

# Hydrogen motional disorder in crystalline iron group chloride dihydrates

Brennan J. Walder,<sup>1</sup> Alex M. Patterson,<sup>1</sup> Jay H. Baltisberger,<sup>2</sup> and Philip J. Grandinetti<sup>1,a)</sup>

<sup>1</sup>*Department of Chemistry, Ohio State University, 100 West 18th Avenue, Columbus, Ohio 43210, USA*

<sup>2</sup>*Division of Natural Science, Mathematics, and Nursing, Berea College, Berea, Kentucky 40403, USA*

(Received 21 April 2018; accepted 3 August 2018; published online 30 August 2018)

The principal components and the relative orientation of the  $^2\text{H}$  paramagnetic shift and quadrupolar coupling tensors have been measured for the  $\text{MCl}_2 \cdot 2\text{D}_2\text{O}$  family of compounds,  $\text{M} = \text{Mn, Fe, Co, Ni, and Cu}$ , using the two-dimensional shifting- $d$  echo nuclear magnetic resonance experiment in order to determine (1) the degree of unpaired electron delocalization and (2) the number and location of crystallographically distinct hydrogen sites around oxygen and their fractional occupancies. Expressions for the molecular susceptibility of  $3d$  ion systems, where the spin-orbit coupling is a weak perturbation onto the crystal field, are derived using the generalized Van Vleck equation and used to predict molecular susceptibilities. These predicted molecular susceptibilities are combined with various point dipole source configurations modeling unpaired electron delocalization to predict  $^2\text{H}$  paramagnetic shift tensors at potential deuterium sites. The instantaneous deuterium quadrupolar coupling and shift tensors are then combined with parameterized motional models, developed for trigonally ( $\text{M} = \text{Mn, Fe, Co, and Cu}$ ) and pyramidally ( $\text{M} = \text{Ni}$ ) coordinated  $\text{D}_2\text{O}$  ligands, to obtain the best fit of the experimental 2D spectra. Dipole sources placed onto metal nuclei with a small degree of delocalization onto the chlorine ligands yield good agreement with the experiment for  $\text{M} = \text{Mn, Fe, Co, and Ni}$ , while good agreement for  $\text{CuCl}_2 \cdot 2\text{D}_2\text{O}$  is obtained with additional delocalization onto the oxygen. Our analysis of the salts with trigonally coordinated water ligands ( $\text{M} = \text{Mn, Fe, Co, and Cu}$ ) confirms the presence of bisector flipping and the conclusions from neutron scattering measurements that hydrogen bonding to chlorine on two adjacent chains leads to the water molecule in the  $[\text{M}(\text{D}_2\text{O})_2\text{Cl}_4]$  cluster being nearly coplanar with  $\text{O-M-Cl}$  involving the shortest metal-chlorine bonds of the cluster. In the case of  $\text{NiCl}_2 \cdot 2\text{D}_2\text{O}$ , the experimental parameters were found to be consistent with a motional model where the  $\text{D}_2\text{O}$  ligands are pyramidally coordinated to the metal and undergo bisector flipping while the water ligand additionally hops between two orientations related by a  $120^\circ$  rotation about the  $\text{Ni-O}$  bond axis. The position of the three crystallographically distinct hydrogen sites in the unit cell was determined along with fractional occupancies. This restricted water ligand motion is likely due to van der Waals interactions and is concerted with the motion of neighboring ligands. *Published by AIP Publishing.* <https://doi.org/10.1063/1.5037151>

## I. INTRODUCTION

Hyperfine interactions in paramagnetic samples cause large nuclear magnetic resonance frequency shifts and enhance nuclear spin relaxation rates.<sup>1–3</sup> Paramagnetic shifts and relaxation enhancements have long been exploited in solution NMR spectroscopy to study chemical equilibria,<sup>4</sup> analyze unpaired spin densities in transition metal complexes,<sup>5</sup> determine distance constraints,<sup>6</sup> and act as contrast agents in magnetic resonance imaging.<sup>7</sup> The incorporation of biologically compatible paramagnetic ions such as divalent cations of the iron group and trivalent lanthanide cations into biomacromolecular systems is well established as a powerful method for obtaining additional information about protein structures, binding, and activity.<sup>8</sup>

Magnetic resonance studies of paramagnetic samples in the solid state are more challenging. In the decades following the pioneering work of Bloembergen,<sup>9</sup> analyzing paramagnetic shifts in the single crystal proton NMR spectrum of

$\text{CuSO}_4 \cdot 5\text{H}_2\text{O}$ , solid-state NMR of paramagnetic materials was used to explore magnetic effects and chemical bonding.<sup>10–15</sup> Large paramagnetic frequency anisotropies and rapid transverse relaxation rates, although undoubtedly a rich source of electronic and structural information in these systems, have historically led to a preference for single crystals at low temperatures. This situation changed with the application of magic-angle spinning (MAS), which provided sufficient averaging of the inhomogeneous broadening to permit accurate spectral interpretation, first in inorganic materials and simple coordination complexes,<sup>16–18</sup> followed by organic and biological systems as continual increases to the attainable MAS rotation rates further improved spectral resolution.<sup>19–23</sup> The constraints afforded by measuring site-specific paramagnetic shifts and relaxation rates in solid-state NMR have become an invaluable tool in the nascent field of NMR crystallography.<sup>24–26</sup>

Additional information useful for electronic, magnetic, and structural studies of materials can be found in the same paramagnetic shift anisotropy (PSA) that MAS attempts to remove from the spectrum. When the sample rotation rate

<sup>a)</sup>URL: <http://www.grandinetti.org>.

is low enough, residual anisotropy survives as a spinning sideband manifold, which can be analyzed for the PSA tensor and linked back to material properties.<sup>27</sup> The simultaneous existence of other nuclear spin interaction tensors possessing frequency anisotropy, such as nuclear quadrupolar coupling tensors, further enriches the depth with which one can characterize material properties,<sup>12,28</sup> but with one-dimensional nuclear magnetic resonance spectra, resolution can be impaired beyond the point of usefulness. Even when high resolution is not critical, e.g., when only one magnetically distinct NMR nucleus is present, there is usually a high degree of correlated uncertainty among parameters analyzed from such line shapes, particularly for stationary powder samples.

We recently introduced a two-dimensional experiment for separating and correlating the first-order shift and quadrupolar anisotropic line shapes.<sup>29</sup> Two-dimensional approaches are superior to analyses of one-dimensional static and MAS patterns,<sup>30–32</sup> allowing for a more precise determination of relative tensor orientations as first illustrated by Ernst and co-workers.<sup>33</sup> An attractive advantage of the quadrupolar correlation is that the magnitude and orientation of the quadrupolar coupling tensor relative to the molecular or crystal frame is relatively easy to determine and immune to not only magnetic effects originating from the PSA but also those of macroscopic origin such as crystalline demagnetizing fields. For this reason, the correlation to the quadrupolar coupling proves to be a valuable constraint on the orientation of the paramagnetic shift tensor, allowing a determination of its molecular frame orientation even for polycrystalline samples. Using this approach with <sup>2</sup>H NMR of CuCl<sub>2</sub>·2D<sub>2</sub>O, the experimental PSA was determined with such an accuracy that a point dipole model reveals slight displacements of the chlorine dipole sources away from the metal center to regions of high electron density.<sup>27,34</sup>

In this work, we further explore the potential of this approach to model <sup>2</sup>H two-dimensional NMR anisotropic correlation spectra from a series of transition metal ion containing salts, MCl<sub>2</sub>·2D<sub>2</sub>O with M = Mn, Fe, Co, and Ni, each having total electron spins of *S* = 5/2, 2, 3/2, and 1, respectively. These salts, each antiferromagnetic at low temperature, possess a high density of paramagnetic centers, making them challenging from the perspective of a point dipole model. Furthermore, the Mn, Fe, and Co members are isostructural, making them particularly well suited for comparing different models of unpaired electron delocalization. Here we adopt a more detailed crystal field theory analysis for calculating the molecular magnetic susceptibility of the transition metals via the generalized Van Vleck equation. Using these more accurate susceptibilities, we are able to identify motional models for the water ligands, even in the perplexing case of NiCl<sub>2</sub>·2D<sub>2</sub>O, and identify the number and location of crystallographically distinct hydrogen sites around oxygen and their fractional occupancies.

## II. METHODS

### A. Sample preparation

An enrichment apparatus capable of selectively applying high vacuum or a flow of dry N<sub>2</sub> gas at elevated temperatures

was designed to enrich the samples in deuterium while preventing the formation of complexes with the hydration state greater than that of the dihydrate. The apparatus consists of a three-neck 50 mL round bottom flask with a gas inlet adapter branched off a line between the N<sub>2</sub> source and a mineral oil bubbler. The flow of N<sub>2</sub> into the flask could be controlled with this adapter. Under N<sub>2</sub> counterflow, the stoppered neck of the flask could be removed to charge the flask with a desired amount of material, manually stirred, or fitted to a high vacuum line. The flask was kept immersed in a mineral oil bath on a hot plate used for magnetic stirring and holding the solution at a temperature (stable within a range of 5 °C) in which the thermodynamically favored coexisting solid phase was the dihydrate. Adding DCl to the solution also favors the dihydrate. Upon precipitation and drying of crystals under high vacuum, the flask was transferred to a nitrogen filled glove bag where the crystals were crushed and placed in a glass vial for storage in a desiccator, preventing further exposure to moisture. The pure samples could not be stored indefinitely in this way, particularly FeCl<sub>2</sub>·2D<sub>2</sub>O, which oxidized noticeably in a few days. Details specific to each sample are given in the [supplementary material](#).

### B. NMR

All NMR experiments were performed at 9.4 T using a single-channel Bruker static-sample probe on an Avance III HD spectrometer. The spectrometer frequency for <sup>2</sup>H was exactly 61.495 MHz, corresponding to the resonance frequency of heavy water, with additional carrier offsets of 3000 Hz, 10 761.63 Hz, and −8550 Hz for the experiments on CuCl<sub>2</sub>·2D<sub>2</sub>O, FeCl<sub>2</sub>·2D<sub>2</sub>O, and MnCl<sub>2</sub>·2D<sub>2</sub>O, respectively. A variable temperature (VT) controller supplied 1200 L/h gas flow at 300.0 K to the sample to stabilize its temperature.

Each powdered sample was worked into a small capillary tube by tapping the closed end of the capillary against a countertop. Finely ground silica was used as a spacer to ensure roughly a 6 mm stretch of the sample could be centered in the NMR coil. By mass difference measurements, the final packing fraction was estimated to be less than or around 0.2 for each sample. A tightly wound solenoid approximately 10 mm in length with a turn density of approximately 4 turns/mm was made by rolling 34 AWG copper over the same 1.7 mm OD capillary NMR tube (Wilma LabGlass) used as the sample container. This allowed the coil to be slid directly over the sample capillary and secured in a custom mount. The maximum rf strength generated with this coil was  $\nu_1(^2\text{H}) = 660$  kHz, measured on a sample of neat D<sub>2</sub>O. Attempts to refine the pulse lengths directly on each of the samples by minimizing the total echo artifact indicated that pulse lengths calculated using  $\nu_1$  were optimal to within 0.02  $\mu\text{s}$ . For CoCl<sub>2</sub>·2D<sub>2</sub>O, FeCl<sub>2</sub>·2D<sub>2</sub>O, and MnCl<sub>2</sub>·2D<sub>2</sub>O, it was recognized that the magnitude of the total echo artifact could be reduced somewhat by dematching the probe to increase the excitation bandwidth. Hence, pulse lengths were selected using a calibration table giving pulse lengths as a function of probe attenuation and transmitter power. The final pulse lengths and corresponding power settings used in the experiments are reported in the [supplementary material](#).

To separate and correlate the first-order quadrupolar coupling and shift interactions, we use the three-pulse shifting-*d* echo pulse sequence, shown in Fig. 1. We describe this sequence in the context of the symmetry pathway notation<sup>35</sup> where the spin transition functions are defined between spin states  $|m_i\rangle$  and  $|m_j\rangle$  by

$$\begin{aligned}\mathbb{P}_I(m_i, m_j) &= m_j - m_i, \\ \mathbb{D}_I(m_i, m_j) &= \sqrt{\frac{3}{2}}(m_j^2 - m_i^2).\end{aligned}\quad (1)$$

The spatial functions for the  $\xi$ th interaction are defined using the upper-case symbols according to

$$\mathbb{D}^{(\xi)}(\Theta) \propto R_{2,0}^{(\xi)}(\Theta), \quad (2)$$

where  $R_{2,0}^{(\xi)}$  is the irreducible second-rank tensor element in the laboratory frame describing the spatial part of the NMR frequency for the interaction labeled  $\xi$ . The orientation dependence of the spatial part is represented by  $\Theta$ , often given in terms of a full-body rotation using the Euler angles  $(\alpha, \beta, \gamma)$ . We adopt this approach here, using the *z*-*y*-*z* convention of intrinsic Euler angle rotations.<sup>36</sup>

The first-order quadrupolar coupling contribution to the NMR frequency is purely anisotropic and is written in symmetry pathway notation as

$$\Omega_q^{(1)}(\Theta, m_i, m_j) = \omega_q \mathbb{D}^{(q)}(\Theta) \mathbb{D}_I(m_i, m_j), \quad (3)$$

where  $\omega_q$  is the quadrupolar splitting, defined as

$$\omega_q = \frac{6\pi C_q}{2I(2I-1)}, \quad (4)$$

with  $C_q = eQ_{\gamma}I\zeta_q/(4\pi\epsilon_0 h)$  as the quadrupolar coupling constant in Système International (SI) units where  $\zeta_q$  is the electric

field gradient (efg) tensor anisotropy. Here, we have defined the principal axis system (PAS) of a real second-rank symmetric tensor as the coordinate system where its matrix representation is diagonal with principal components,  $\lambda_{ii}$ , ordered according to the Haeberlen convention,<sup>37</sup> where  $|\lambda_{zz}| \geq |\lambda_{xx}| \geq |\lambda_{yy}|$ . The anisotropic line shape is characterized by the anisotropic strength parameter  $\zeta_\xi = \lambda_{zz}$  and asymmetry parameter  $\eta_\xi = (\lambda_{yy} - \lambda_{xx})/\zeta_\xi$ . When two (or more) anisotropic interactions are present, the line shape will depend on not only the principal components describing each interaction but also the relative orientations of their principal axis systems, which can be described by Euler angles  $(\alpha_{\text{rel}}, \beta_{\text{rel}}, \gamma_{\text{rel}})$ . An important feature of the first-order quadrupolar coupling is that it is immune to the effects of magnetic susceptibility, making the efg tensor a useful reference frame for determining the orientation of the paramagnetic shift tensor in a molecular frame.

The paramagnetic shift contribution<sup>27,38,39</sup> to the NMR frequency can be written using symmetry pathway notation as the sum of two components

$$\begin{aligned}\Omega_p^{(1)}(\Theta, m_i, m_j) &= \omega_0 P_{\text{iso}} \mathbb{P}_I(m_i, m_j) \\ &+ \omega_0 \zeta_P \mathbb{D}^{(P)}(\Theta) \mathbb{P}_I(m_i, m_j),\end{aligned}\quad (5)$$

where  $P_{\text{iso}}$  is the isotropic paramagnetic shift,  $\zeta_P$  is the paramagnetic shift anisotropy, and  $\omega_0$  is the nuclear Larmor frequency. As all field shift interactions possess the same symmetry representation, no experiment manipulating solely the spin and spatial degrees of freedom of the sample can segregate the paramagnetic shift from the closed-shell nuclear shielding interaction, which dominates the field shifts of diamagnetic compounds. Since shifts due to nuclear shielding for  $^2\text{H}$  are two to three orders of magnitude smaller than the paramagnetic shifts we report in this study, its contribution to the shift parameters will be ignored.

The transition pathways for the shifting-*d* echo experiment, beginning from the Zeeman order,  $[z_I]$ , of a spin  $I = 1$  nucleus like  $^2\text{H}$  are

$$\{I = 1\} : \begin{cases} [z_I] \rightarrow |-1\rangle\langle 0|_{t_1/2} \rightarrow |1\rangle\langle 0|_{t_1/2} \rightarrow |0\rangle\langle 1|_{t_2} \\ [z_I] \rightarrow |0\rangle\langle 1|_{t_1/2} \rightarrow |0\rangle\langle -1|_{t_1/2} \rightarrow |-1\rangle\langle 0|_{t_2} \end{cases} \quad (6)$$

These are illustrated in Fig. 1(b). The  $\mathbb{P}_I$  pathway, corresponding to pure paramagnetic shift evolution, refocuses at  $t_2 = 0$ , while the  $\mathbb{D}_I$  pathway, corresponding to pure quadrupole evolution, refocuses when  $t_2 = t_1$ . A  $\kappa^{(t_1)} = -1$  shearing transformation applied to the 2D shifting-*d* echo signal correlates the two interactions along orthogonal dimensions and a 2D Fourier transform yields the correlation spectrum.<sup>29</sup> At the two-dimensional time origin,  $t_1 = t_2 = 0$ , the evolution due to both the ( $\mathbb{P}_I$ ) paramagnetic shift and ( $\mathbb{D}_I$ ) first-order quadrupolar frequency contributions refocuses into a simultaneous echo which, in the absence of frequency contributions with transition symmetries other than  $\mathbb{P}_I$  or  $\mathbb{D}_I$ , is a total echo.

The sheared experimental spectra for the deuterated iron group chloride dihydrates at 300.0 K are shown in Fig. 2. All spectral processing, including affine transformations, was

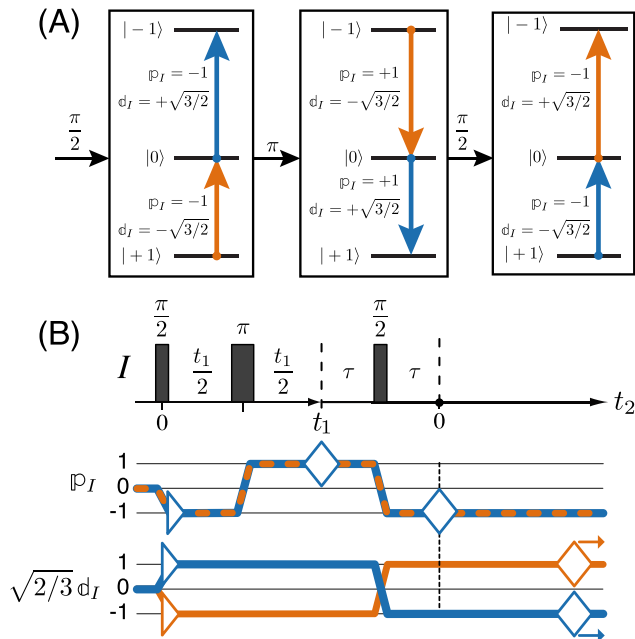


FIG. 1. Relevant spin transition pathways for the shifting-*d* echo experiment, displaying the first observable transition pathway given in Eq. (6). (b) Pulse sequence and spin transition pathways for the experiment. Signal acquisition begins immediately after the final pulse where  $t_2 = -\tau$ .

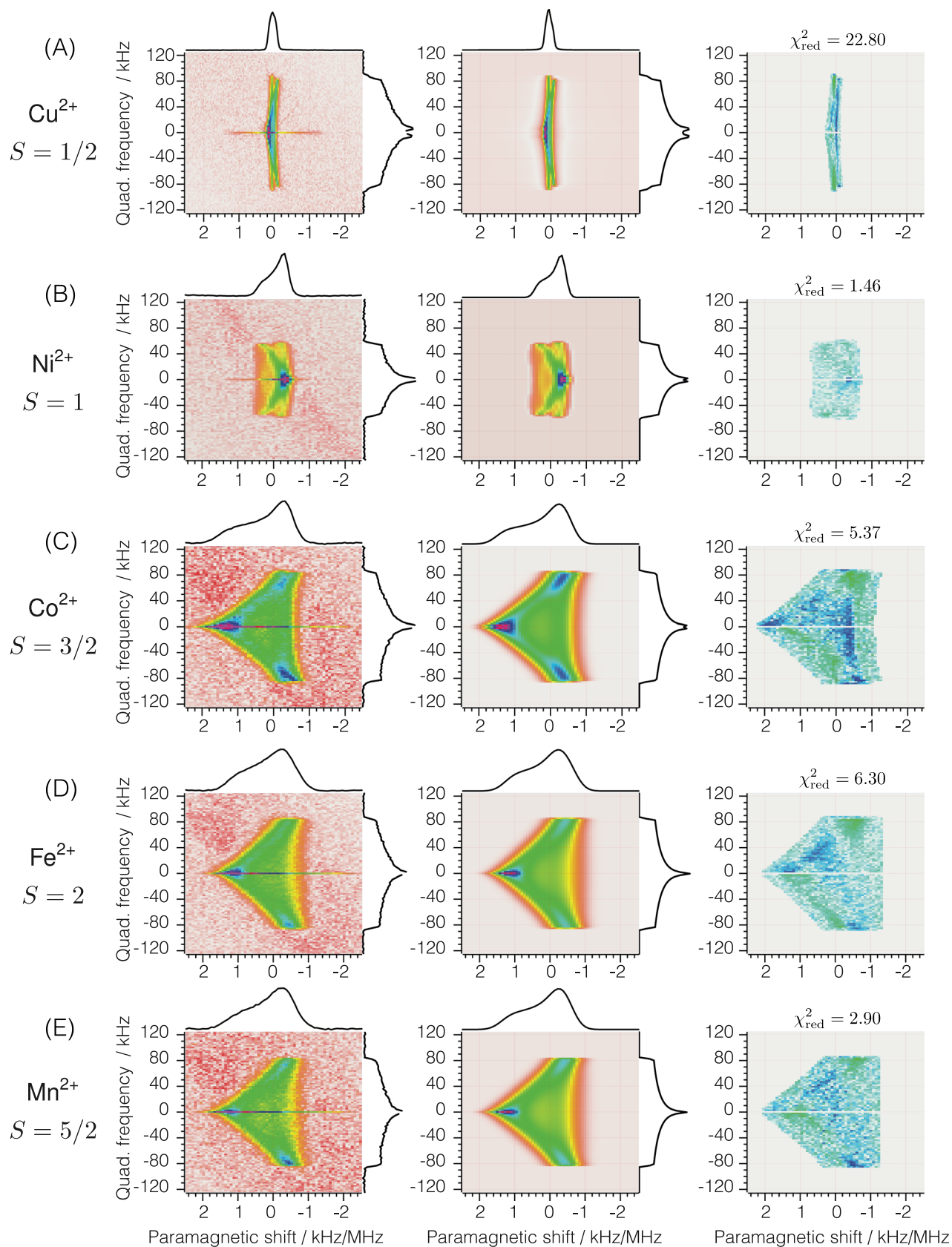


FIG. 2. Comparison of shifting-*d* echo  $^2\text{H}$  NMR experimental, best fit, and residual spectra for each of the  $\text{MCl}_2 \cdot 2\text{D}_2\text{O}$  salts measured in this study. On the horizontal axis, 1 kHz/MHz corresponds to 1000 ppm. Blank regions in the residuals correspond to points masked from the best fit analysis.

performed using the MacOS application RMN (version 1.8.4).<sup>40</sup> In all experimental and simulated 2D spectra, the color hue is linearly proportional to the NMR signal intensity

and the color saturation goes to zero as the NMR signal intensity magnitude approaches zero. These 2D spectra contain information related to the eigenvalues of both interaction



tensors as well as their relative orientation. The distinctive symmetry about the zero quadrupolar frequency axis is evident, along with a small spectral artifact which is a consequence of pulse imperfections contributing to breakthrough pathways<sup>29</sup> which generate simultaneous *p* and *d* echoes (total echo) for nonzero values of  $t_1$ . Also shown are the projections onto the horizontal and vertical axes, giving pure paramagnetic shift and quadrupolar frequency spectra, respectively. If desired, the principal components of the quadrupolar coupling and paramagnetic shift tensors can be determined from these 1D patterns. The principal components can also be determined from the 2D correlation spectrum itself if the relative orientation of the tensor is simultaneously analyzed. We adopt the latter approach and analyze the line shape directly from the 2D correlation spectrum—which forms the basis for validating our modeling results—and report that the best fit parameters estimated 95% confidence intervals (CIs) in Table I.

The residuals shown in Fig. 2 indicate that all salts examined here fit well to a single deuteron site. In crystalline hydrates at room temperature, the deuterons undergo motion on a faster time scale than the NMR experiment. This renders all deuterons NMR equivalent and leads to a spectrum that is characterized by motional averaged quadrupolar coupling and paramagnetic shift tensors.<sup>29,41</sup> In the absence of motion, the instantaneous  $^2\text{H}$  efg tensor is expected to be axially symmetric with the  $e q_{zz}$  axis lying along the O–D bond. Typical values<sup>42</sup> of the  $^2\text{H}$   $C_q$  in crystalline hydrates are approximately  $C_q = 230$  kHz with  $\eta_q \approx 0$ , which we verify with a shifting-*d* echo measurement of  $\text{NiCl}_2 \cdot 2\text{D}_2\text{O}$  at 173 K as reported in the [supplementary material](#).

As discussed later, two of the angles describing the relative orientation of the tensors are predicted to be integer multiples of  $\pi/2$ , except for  $\text{NiCl}_2 \cdot 2\text{D}_2\text{O}$ . We restricted the domain of  $\alpha_{\text{rel}}$  for these fits, constraining  $\beta_{\text{rel}}$  and  $\gamma_{\text{rel}}$  to integer multiples of  $\pi/2$  in order to give a one-to-one correspondence between the orientation parameters and a unique 2D line shape.

### C. Spectral modeling

The two-dimensional line shapes were subjected to maximum likelihood estimation according to the  $\chi^2$  parameter, where  $\chi^2$  is the spectral noise-weighted sum of the squared residuals. This was carried out with a C program using Markov Chain Monte Carlo (MCMC) sampling according to a Metropolis-Hastings algorithm<sup>43</sup> to generate statistics from goodness-of-fit comparisons to numerically generated two-dimensional correlation spectra as functions of spectral intensity,  $\zeta_P$ ,  $\eta_P$ ,  $C_q$ ,  $\eta_q$ , the Euler angles ( $\alpha_{\text{rel}}$ ,  $\beta_{\text{rel}}$ ,  $\gamma_{\text{rel}}$ ) describing the relative orientation of the paramagnetic shift and quadrupole coupling tensors, and the Gaussian and Lorentzian line broadening parameters for the paramagnetic shift dimension,  $\sigma_{\text{GB}}$  and  $\gamma_{\text{LB}}$ . The quadrupolar dimension was modeled without any additional line broadening parameters. In our previous study<sup>29</sup> of  $\text{CuCl}_2 \cdot 2\text{D}_2\text{O}$ , we describe the development of an improved 2D tenting algorithm, which we also utilize here. Such 2D frequency domain tenting algorithms<sup>44,45</sup> are critical for achieving a sufficiently thorough Monte Carlo sampling of the multidimensional  $\chi^2$  surface in a timely manner.

For the  $\text{CoCl}_2 \cdot 2\text{D}_2\text{O}$ ,  $\text{FeCl}_2 \cdot 2\text{D}_2\text{O}$ , and  $\text{MnCl}_2 \cdot 2\text{D}_2\text{O}$  spectra, suppression of the total echo artifact was significantly poorer than for the  $\text{CuCl}_2 \cdot 2\text{D}_2\text{O}$  and  $\text{NiCl}_2 \cdot 2\text{D}_2\text{O}$  spectra and was readily identified as a source of bias in the line broadening parameters. This bias was partially removed by masking the data at zero quadrupolar frequency before fitting. A mask was also used to remove points with no significant signal intensity. Despite these efforts, residuals above the level of noise were observed for the best fit spectra, which choked the  $\chi^2$  hypersurface in the vicinity of the minimum and led to unreasonably narrow confidence intervals, an effect which has been discussed previously in the analysis of EPR line shapes.<sup>46</sup> Rather than laboriously determine a way to model the bias—which amounts to a rather small component particularly given that residuals were still approximately normally distributed

TABLE I. Best fit tensor parameters determined from the 2D shifting-*d* echo line shapes for  $\text{MCl}_2 \cdot 2\text{D}_2\text{O}$  samples at 300.0 K. Symbols inside angle brackets represent motional averaged values. Since  $N_{\text{pts}} \geq 1000$ , the degree of freedom correction is neglected in calculating the reduced chi-squared parameter, defined here as  $\chi_{\text{red}}^2 = \chi_{\text{best}}^2 / N_{\text{pts}}$ . Values are given as approximate 95% confidence intervals (CIs) determined from the chi-scaled MCMC routine. Values in between the CI limits represent the best fit corresponding to the given  $\chi_{\text{red}}^2$ .

M	$P_{\text{iso}}$ (ppm)	$\langle \zeta_P \rangle$ (ppm)	$\langle \eta_P \rangle$	$\langle C_q \rangle$ (kHz)	$\langle \eta_q \rangle$	$\langle \alpha_{\text{rel}} \rangle$ (deg)	$\langle \beta_{\text{rel}} \rangle^{\text{a}}$ (deg)	$\langle \gamma_{\text{rel}} \rangle^{\text{a}}$ (deg)	$\chi_{\text{red}}^2$
Cu	$51^{+2}_{-3}$	$-147 \pm 4$	$0.84^{+0.11}_{-0.04}$	$118.0^{+1.7}_{-1.2}$	$0.86 \pm 0.01$	$[95^{+7}_{-5}]^{\text{b,c}}$	$[90]^{\text{c}}$	0	22.8
Ni	$-97^{+7}_{-6}$	$551^{+14}_{-12}$	$0.12^{+0.24}_{-0.10}$	$77.2^{\text{d}}$	$0.91^{+0.04}_{-0.01}$	$[62]$	$[114]^{\text{e}}$	$[171]^{\text{d,e}}$	1.46
Co	$215^{+13}_{-11}$	$1310^{+23}_{-19}$	$0.23^{+0.04}_{-0.07}$	$114.6^{+1.5}_{-0.7}$	$0.95 \pm 0.02$	$180^{+0}_{-10}$	90	90	5.37
Fe	$101^{+8}_{-12}$	$1187^{+17}_{-24}$	$0.40^{+0.06}_{-0.09}$	$114.2^{+1.8}_{-0.6}$	$0.98^{\text{d,e}}$	$122^{+23}_{-5}$	90	90	6.30
Mn	$145^{+13}_{-9}$	$1236^{+17}_{-22}$	$0.23^{+0.09}_{-0.23}$	$111.4 \pm 0.4$	$1.00^{\text{a}}$	$[136^{+33}_{-1}]^{\text{f}}$	90	90	2.90

<sup>a</sup>Constrained, as justified above.

<sup>b</sup>CI for one-tailed distribution, with the domain boundary denoted by square brackets.

<sup>c</sup>Best fit solution of an analysis with constrained  $\langle \alpha_{\text{rel}} \rangle$  and free  $\langle \beta_{\text{rel}} \rangle$  has a slightly higher  $\chi_{\text{red}}^2$  minimum.

<sup>d</sup>Significant secondary probability maximum.

<sup>e</sup>Constraint released; refer to the [supplementary material](#) for probability histograms.

<sup>f</sup>A value of  $\langle \eta_q \rangle = 1$  with other angle constraints implies that unique  $\alpha_{\text{rel}}$  can be restricted to the domain  $\left[\frac{3\pi}{4}, \pi\right]$ ; CI is for the upper one-tailed distribution on this domain, and no angle is prohibited with >99% confidence.

overall—we estimated the correct but unknown maximum likelihood estimator by scaling the ordinary least squares maximum likelihood estimator. This was implemented by taking the probability of accepting the  $i$ th step extending the Markov chain according to

$$\ln P_{\text{accept},i} = \begin{cases} 0 & \text{if } \chi_{i-1}^2 > \chi_i^2 \\ \frac{1}{2S_\chi} (\chi_{i-1}^2 - \chi_i^2) & \text{if } \chi_{i-1}^2 < \chi_i^2, \end{cases} \quad (7)$$

which is the Metropolis criterion for the ordinary least squares maximum likelihood estimator, scaled by  $S_\chi$ . To assess approximate 95% confidence intervals, we set this correction according to  $S_\chi = 10\chi_{\text{best}}^2/N_{\text{pts}}$ , where  $\chi_{\text{best}}^2$  is the chi-squared parameter of the best fit and  $N_{\text{pts}}$  are the number of points used in the fit, which were not apodized. In this way, greater deviations from the current chi-square value would be deemed as acceptable draws by the MCMC routine, allowing greater exploration of parameter space. This compromise permits us to form approximate probability distributions reflecting our uncertainty in the best fit parameters and explore correlations between parameter uncertainties. We do this by plotting histograms of distributions marginalized over one and two parameters, which are shown in the [supplementary material](#).

### III. THEORETICAL BACKGROUND AND CALCULATIONS

#### A. Paramagnetic shift in the point dipole approximation

The paramagnetic shift originates from the modulation of the applied magnetic field by unpaired electrons.<sup>39</sup> The microscopic magnetic field at the nucleus is dominated by magnetic fields resulting from the microscopic electric currents set up by the orbital motion of the electrons and the spin of the electrons, respectively.<sup>47</sup> These microscopic currents are distributed throughout space. It is often valid to approximate the continuous distributions by one or more point dipole sources, usually placed on neighboring atomic nuclei. At a quantum mechanical level, the strength of the magnetic moments of these dipoles (and hence the resultant microscopic magnetic field) is determined by evaluating magnetic dipole moment operators in the given quantum state of each paramagnetic complex. If the  $LS$ -coupling scheme holds for each paramagnetic center, we can write for this operator

$$\hat{\mu} = -\mu_B(\hat{\mathbf{L}} + g_e\hat{\mathbf{S}})/\hbar, \quad (8)$$

where  $\mu_B$  is the Bohr magneton,  $\hat{\mathbf{L}}$  and  $\hat{\mathbf{S}}$  are the electronic orbital and spin angular momentum operators, and  $g_e = 2.0023$ . Rapid electron relaxation in the paramagnetic state means that, on the NMR time scale, the nucleus couples to a microscopic magnetic field  $\mathbf{B}_P$  arising from an average of  $\hat{\mu}$  over thermally accessible states. This thermal average, denoted here by  $\mathbf{m}$ , behaves like a classical magnetic moment. As such,  $\mathbf{B}_P$  behaves classically, and in the point dipole approximation over a fixed atomic lattice, we can write

$$\mathbf{B}_P(\mathbf{r}) = \frac{\mu_0}{4\pi} \sum_k \frac{1}{r_k^3} \left[ 3(\mathbf{m} \cdot \hat{\mathbf{r}}_k) \hat{\mathbf{r}}_k - \mathbf{m} \right] + \frac{2}{3} \mu_0 \mathbf{m}_S \left( \frac{1}{2S} \rho(\mathbf{r}) \right) \quad (9)$$

for an ensemble of identical noninteracting paramagnetic complexes. We also write  $\mathbf{r}_k = \mathbf{r}_k - \mathbf{r}$  for the separation vector directed from the  $k$ th point dipole source to the NMR nucleus at  $\mathbf{r}$ ,  $\mathbf{r}_k$  for the position of the point dipole source, and  $\hat{\mathbf{r}}_k = \mathbf{r}_k/r_k$  for the unit vector along  $\mathbf{r}_k$ . The second term of Eq. (9) is the so-called “contact” term which arises from a delta-function term in the classical expression for the magnetic field of a dipole and concerns the case when a true point magnetic dipole, i.e., an electron spin, is placed inside the NMR nucleus.<sup>48</sup> It is relevant when a nonzero spin density  $\rho(\mathbf{r})$  resides at the site of the NMR nucleus, as is often the case in paramagnetic compounds due to the effects of spin delocalization and core polarization.<sup>47,49</sup> It is also related to the thermally averaged electronic magnetic moment of the paramagnetic complex due to spin,  $\mathbf{m}_S$ . As detailed in [Appendix B](#),  $\mathbf{m}_S$  differs from  $\mathbf{m}$  in that the orbital contribution to the magnetism is excluded, corresponding to the omission of  $\hat{\mathbf{L}}$  in Eq. (8) when evaluating the thermal average of  $\hat{\mu}$ . Using the total spin magnetic moment  $\mathbf{m}_S$  of the complex, rather than summing the thermally averaged magnetic moments of the  $2S$  individual unpaired electron spin moments, requires dividing the contact term by  $2S$  so that the average spin density per unpaired electron appears in Eq. (9). In the contact term, we assume that the unpaired spin density is not dependent on the spin state of the complex so that it factors out of the thermal average.

The thermally averaged electronic magnetic moment,  $\mathbf{m}$ , is related to the molecular susceptibility tensor,  $\chi$ , according to

$$\mathbf{m} = \frac{1}{\mu_0} \chi \cdot \mathbf{B}_0. \quad (10)$$

The quantity  $\chi$ , unlike  $\mathbf{m}$ , is independent of the applied magnetic field  $\mathbf{B}_0$ . We therefore define the field-independent paramagnetic shift tensor,  $\mathbf{P}$ , of the NMR nucleus in terms of the microscopic magnetic field from which it originates,

$$\mathbf{B}_P(\mathbf{r}) = \mathbf{P} \cdot \mathbf{B}_0. \quad (11)$$

Upon substituting Eq. (10) into Eq. (9) and comparing to Eq. (11), we obtain for the through-space dipolar term

$$\mathbf{P}^D = \frac{1}{4\pi} \chi \cdot \sum_k \frac{1}{r_k^3} \left[ 3\hat{\mathbf{r}}_k \otimes \hat{\mathbf{r}}_k - \mathbf{1} \right], \quad (12)$$

where the summand is the familiar through-space dipolar coupling tensor to the  $k$ th paramagnetic center. Here  $\mathbf{1}$  refers to the unit dyadic. Similarly, the contact term is given by

$$\mathbf{P}^C = \frac{1}{3S} \chi^{(S)} \rho(\mathbf{r}). \quad (13)$$

The total paramagnetic shift tensor of the NMR nucleus in the point-dipole approximation is  $\mathbf{P} = \mathbf{P}^D + \mathbf{P}^C$ . A slightly modified form of the susceptibility,  $\chi^{(S)}$ , appears in Eq. (13)

TABLE II. Principal components of the molecular susceptibility tensor used in the calculation of  $\mathbf{P}^D$ . A constant diamagnetic correction  $\chi_{\text{dia}} \approx -0.0019 \text{ \AA}^3$  has not been included.<sup>57</sup>

Compound	$\chi_{xx} (\text{\AA}^3)$	$\chi_{yy} (\text{\AA}^3)$	$\chi_{zz} (\text{\AA}^3)$
MnCl <sub>2</sub> ·2D <sub>2</sub> O	0.2904	0.2904	0.2904
FeCl <sub>2</sub> ·2D <sub>2</sub> O	0.2287	0.2287	0.3336
CoCl <sub>2</sub> ·2D <sub>2</sub> O	0.0925	0.2170	0.3197
NiCl <sub>2</sub> ·2D <sub>2</sub> O	0.0937	0.0937	0.0937
CuCl <sub>2</sub> ·2D <sub>2</sub> O	0.0276	0.0295	0.0376

due to exclusion of the orbital moment from the thermally averaged  $\mathbf{m}_S$ .

In the analysis that follows, the instantaneous paramagnetic shift tensor parameters are calculated using the molecular susceptibilities in Table II (*vide infra*) with a point dipole source configuration inside of a spherical Lorentz cavity, summed according to Eq. (12) with *Mathematica*.<sup>50</sup> In previous work<sup>29</sup> on CuCl<sub>2</sub>·2D<sub>2</sub>O, we found that a Lorentz cavity with a radius of 60 Å was sufficient for less than 1% error in the calculated parameters. All calculations reported here utilize Lorentz cavities of 100 Å radius. It can be assumed that the contributions of the paramagnetic contact shift,  $\mathbf{P}^C$ , and a relatively tiny closed-shell nuclear shielding contribution to the overall shift anisotropy are negligible.

## B. Molecular susceptibility

Far from magnetic saturation ( $\mu_B B_0 \ll k_B T$ , where  $T$  is the temperature), the molecular susceptibility is analyzed as a thermal average over the zero field energy levels according to Van Vleck's generalized susceptibility equation,<sup>51,52</sup>

$$\chi_{ij} = \frac{\mu_0 \sum_m [W_{m,ij}^I - k_B T W_{m,ij}^{II}] e^{-E_m/(k_B T)}}{k_B T \sum_m e^{-E_m/(k_B T)}}. \quad (14)$$

The energy eigenstates,  $|m\rangle$ , of energy  $E_m$  are specified in a basis at zero applied magnetic field. Matrix elements of  $\hat{\mu}$  are contained in the  $W$  factors,

$$\chi = \mu_0 \mu_B^2 \left[ -2\Lambda + \frac{S(S+1)}{3k_B T} \mathbf{g} \cdot \mathbf{g} - \frac{S(S+1)(2S+3)(2S-1)}{30(k_B T)^2} \mathbf{g} \cdot \mathbf{g} \cdot \mathbf{D} \right], \quad (18)$$

whose derivation from the Van Vleck equation using perturbation theory is outlined in Appendix A. Each term involves the symmetric negative semi-definite orbital angular momentum dequenching tensor  $\Lambda$ , with components<sup>47,53,54</sup>

$$\Lambda_{ij} = \frac{1}{\hbar^2} \sum_{\alpha > 0} \frac{\langle 0 | \hat{L}_i | \alpha \rangle \langle \alpha | \hat{L}_j | 0 \rangle}{E_0 - E_\alpha}, \quad (19)$$

and which has units of inverse energy. Here,  $\alpha$  refers to the ordering of electronic states. The dependence on  $\Lambda$  is explicitly

$$W_{m,ij}^I = \sum_{n'} \langle m | \hat{\mu}_i | n' \rangle \langle n' | \hat{\mu}_j | m \rangle, \quad (15)$$

$$W_{m,ij}^{II} = \sum_{n''} \frac{\langle m | \hat{\mu}_i | n'' \rangle \langle n'' | \hat{\mu}_j | m \rangle + \langle m | \hat{\mu}_j | n'' \rangle \langle n'' | \hat{\mu}_i | m \rangle}{E_m - E_{n''}}. \quad (16)$$

In Eq. (15), the single prime summation carries with it an instruction to sum only over states degenerate with  $|m\rangle$ ; the double prime summation in Eq. (16) carries the opposite instruction.

To apply the Van Vleck equation, the energy level structure of the magnetically active manifold must be known; i.e., the eigenvalue problem must be solved for the zero-field Hamiltonian. This can be done using the framework of crystal field theory.<sup>51</sup> As is well known, the best strategy to solve this problem within this framework depends on both the number of unpaired electrons and the relative size of the following terms:

- $\hat{V}_{ee}$ :  $\mathcal{O}(1 - 100 \text{ eV})$ , the interelectron Coulomb repulsion;
- $\hat{V}_{cf}$ :  $\mathcal{O}(0.01 - 10 \text{ eV})$ , the crystal field potential;
- $\hat{H}_{so}$ :  $\mathcal{O}(< 0.1 \text{ eV})$ , the spin-orbit coupling.

In general,  $\hat{V}_{ee} \gtrsim \hat{V}_{cf} \gtrsim \hat{H}_{so}$  for the 3d shell of iron group cations, suggesting a weak crystal field approach in which the spin-orbit coupling is considered as a perturbation onto the electronic configuration established by  $\hat{H}_0 = \hat{V}_{ee} + \hat{V}_{cf}$  so that the *LS*-coupling scheme applies. There is no orbital contribution to the magnetism whatsoever when the ground state of this electronic configuration is orbitally nondegenerate (i.e., nondegenerate in the neglect of the spin degrees of freedom) and  $\hat{H}_{so} = 0$ . In this case, the molecular susceptibility is isotropic and obeys the Curie law,

$$\chi = \frac{\mu_0 \mu_B^2 g_e^2 S(S+1)}{3k_B T} \mathbf{1}. \quad (17)$$

Weak spin-orbit coupling reintroduces an orbital contribution to the magnetism, leading to susceptibility anisotropy and violation of the Curie law's characteristic  $T^{-1}$  dependence. The molecular susceptibility for such spin-orbit dequenched systems is given by

shown for the temperature independent term and encoded into the symmetric EPR  $\mathbf{g}$  tensor, introduced in the  $T^{-1}$  dependent term, and the traceless symmetric part of the zero field splitting tensor  $\mathbf{D}$ , introduced in the  $T^{-2}$  dependent term,<sup>55</sup> according to

$$g_{ij} = g_e \delta_{ij} + 2\lambda_{so} \Lambda_{ij}, \quad (20)$$

$$D_{ij} = \lambda_{so}^2 \left( \Lambda_{ij} - \frac{1}{3} \text{Tr}\{\Lambda\} \delta_{ij} \right). \quad (21)$$

Equation (18) is valid provided that the spin-orbit coupling constant  $\lambda_{\text{so}}$  obeys  $|\lambda_{\text{so}}| \ll E_1$ , where  $E_1$  is the energy of the first excited electronic state relative to the ground state, and provided that the splittings of the ground manifold are small enough to be treated in the high temperature approximation. When these conditions do not hold, one must generally resort to a numerical evaluation of the Van Vleck equation. A concise expression for the “spin molecular susceptibility”  $\chi^{(S)}$  in spin-orbit dequenched systems can also be written and is given in Appendix B.

Finally, the Van Vleck equation gives the susceptibility of a single isolated paramagnetic center. In the iron group chloride dihydrates, the paramagnetic centers interact with each other. In the paramagnetic phase, this effect can be approximately handled by using an effective temperature,  $T_{\text{eff}} = T - T_c$ , in the susceptibility expressions, where  $T_c$  is the Weiss constant. For example, in Eq. (17), we have

$$\chi = \frac{\mu_0 \mu_B^2 g_e^2 S(S+1)}{3k_B(T - T_c)} \mathbf{1}, \quad (22)$$

the so-called Curie-Weiss law common to the literature on magnetic susceptibilities.<sup>51</sup>

### C. Molecular susceptibility calculations

Here we describe how  $\chi$  is evaluated for each of the divalent metal cations in the dihydrate salts measured in this work. The crystal field for each metal is predominantly cubic, with a potential represented by  $\hat{V}_{\text{cb}}$ . Further tetragonal ( $\hat{V}_{\text{ax}}$ ) and rhombic ( $\hat{V}_{\text{rh}}$ ) distortions of the crystal field lead to a pseudo- $D_{2h}$  metal complex. Symmetry descent from the free ion is used to consider the effects of the different crystal field terms. To aid in the following discussions, the crystal field energy level diagrams are given in the [supplementary material](#). We generally consider effects that influence the result to a 5% level. A similar approach, using the angular overlap method, has been previously described.<sup>56</sup> The principal components of the molecular susceptibility tensors calculated in this section are given in Table II.

#### 1. $\text{MnCl}_2 \cdot 2\text{D}_2\text{O}$ : $\text{Mn}^{2+}$ , $^6S$

The  $\text{Mn}^{2+}$  free ion term,  $^6S$ , signifies an orbital singlet state ( $L = 0$ ) whose character is not appreciably altered by the distorted cubic crystal field. The excited terms are over 3700 meV removed from the ground state.<sup>58,59</sup> Deviation of the  $g$ -tensor components from the free-electron  $g$ -value has not been detected, and very weak zero field splittings around 0.01 meV are primarily from effects beyond those captured by our description of spin-orbit dequenched magnetism.<sup>60</sup> With a high level of confidence, we have  $\Lambda = 0$ , and therefore, take the isotropic Curie-Weiss law, Eq. (22), with  $S = 5/2$  and a Weiss constant<sup>61</sup> of  $T_c = -14.5$  K to calculate the molecular susceptibility for  $\text{MnCl}_2 \cdot 2\text{D}_2\text{O}$ . The Weiss correction leads to a small decrease of the isotropic susceptibility from the isolated spin-only prediction of Eq. (17), as shown in Fig. 3.

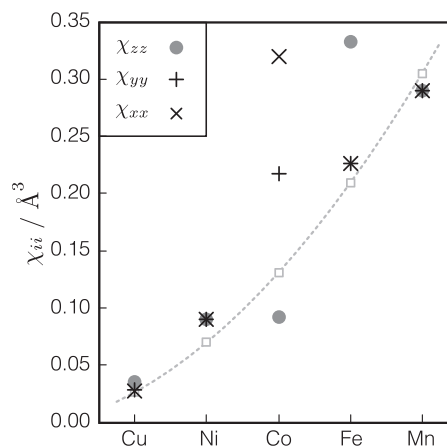


FIG. 3. Plot of the principal components given in Table II. Square boxes, connected by a dashed line to guide the eye, are the isolated spin-only prediction at  $T = 300$  K according to the Curie law, Eq. (17).

#### 2. $\text{FeCl}_2 \cdot 2\text{D}_2\text{O}$ : $\text{Fe}^{2+}$ , $^5D$

The free ion ground state of  $\text{Fe}^{2+}$  is  $^5D$ , whose five-fold orbital degeneracy is partially lifted in a cubic crystal field to produce a  $T_{2g}$  orbital triplet ground state. Any  $T$  state subspace has proper first-order orbital angular momentum with a fictitious  $\tilde{L} = 1$ , with this particular  $T$  state possessing a fictitious orbital  $g$  factor<sup>47,53</sup> of  $\tilde{g}_L = -1$ . As illustrated in Fig. S3 of the [supplementary material](#), further descent from the  $O_h$  point group must lift the orbital degeneracy as only nondegenerate electronic states are permissible electronic eigenfunctions of the symmetry operations of  $D_{2h}$ , and such states cannot possess first-order orbital angular momentum.<sup>51</sup> Room temperature susceptibility measurements have never been published; fortunately, the electronic states of  $\text{FeCl}_2 \cdot 2\text{H}_2\text{O}$ , as well as  $\text{FeCl}_2 \cdot 2\text{D}_2\text{O}$ , are well known by Raman spectroscopy.<sup>62</sup> A detailed analysis of these data by Graf,<sup>63</sup> aided by low temperature magnetic susceptibility measurements showing an (accidentally) axial  $g$ -tensor,<sup>64</sup> showed a ground  $B_{1g}$  state separated from the first excited  $B_{2g}$  state by over  $E_1 = 60$  meV. The second excited  $B_{3g}$  state lies about  $E_2 = 210$  meV above the ground state. Each of these states is a quintet with respect to the spin degrees of freedom, which is split upon introduction of the spin-orbit coupling giving rise to significant zero-field splittings<sup>65,66</sup> approaching  $1.2 \text{ meV} \ll k_B T = 26 \text{ meV}$  at 300 K. Since  $E_1$  is rather large compared to  $\lambda_{\text{so}}(\text{Fe}^{2+}) = -12 \text{ meV}$ <sup>67</sup> and high enough to avoid significant thermal population at room temperature, we consider  $\text{FeCl}_2 \cdot 2\text{D}_2\text{O}$  to fulfill the criteria for second-order spin-orbit dequenched magnetism, permitting the use of Eq. (18) to calculate the molecular susceptibility. Following Graf, we determine the principal components of the orbital angular momentum dequenching tensor to be

$$\Lambda_{zz} = -0.0160 \text{ meV}^{-1},$$

$$\Lambda_{xx} = \Lambda_{yy} = -0.0047 \text{ meV}^{-1},$$

where the principal  $z$ -axis, directed along the short Fe–Cl bond of the complex, is common to both the dequenching and susceptibility tensors. We used an orbital reduction parameter<sup>68</sup>



of 0.9 to approximate the reduction of the spin-orbit coupling strength through the effects of covalency, although other values can be justified to improve consistency with other analyses.<sup>65,66</sup> The Weiss constant is  $|T_C| \lesssim 10$  K and we neglect its contribution here.<sup>64</sup>

We can compare the molecular susceptibility of the  $\text{Fe}^{2+}$  case calculated using Eq. (18) to that of the  $\text{Mn}^{2+}$  case calculated using Eq. (22) in Fig. 3. The anisotropic orbital dequenching tensor of the former case leads to significant molecular susceptibility anisotropy, with a nearly 60% deviation of  $\chi_{zz}$  from the isolated spin-only prediction of Eq. (17) but only about a 10% deviation for the other two principal components. The deviation from the spin-only prediction is always positive owing to the negative sign of the spin-orbit coupling constant, leading to positive deviations from  $g_e$  in Eq. (20). The relative contribution of the **g**, temperature independent, and **D** terms to the susceptibility is given in Table S-V of the [supplementary material](#), where it is seen that the latter two terms make comparable and significant contributions at 300 K to the molecular susceptibility.

### 3. $\text{CoCl}_2 \cdot 2\text{D}_2\text{O}$ : $\text{Co}^{2+}$ , $^4\text{F}$

The free ion ground state of  $\text{Co}^{2+}$  is  $^4\text{F}$ . As with  $\text{FeCl}_2 \cdot 2\text{D}_2\text{O}$  and illustrated in Fig. S4 of the [supplementary material](#), an orbital triplet results as the ground state when the cubic field is imposed onto the  $\text{Co}^{2+}$  free ion, which contains some excited  $^4\text{P}$  character due to a configuration interaction.<sup>47</sup> Another orbital triplet and an orbital singlet result as first and second excited states. The most significant complication is due to the fact that the crystal fields  $\hat{V}_{\text{ax}}$  and  $\hat{V}_{\text{rh}}$  in distorted octahedral cobaltous complexes are of comparable strength<sup>69</sup> to  $\lambda_{\text{so}}(\text{Co}^{2+}) = -22$  meV<sup>67</sup> and often produce insufficient separation between the ground and excited electronic states to permit application of the expressions pertinent to the spin-orbit dequenched magnetism. In other words, the electronic ground state of octahedrally coordinated cobaltous complexes often remains quasi-degenerate and orbital angular momentum is not effectively quenched to even first order. Thus, we cannot utilize the dequenching tensor expression of Eq. (18) and revert back to the more general Van Vleck expression of Eq. (14).

While sufficient data characterizing the electronic states of  $\text{CoCl}_2 \cdot 2\text{D}_2\text{O}$  is lacking, a valuable set of low temperature ( $<120$  K) bulk magnetic susceptibility measurements and analysis by Narath<sup>28</sup> is available. He numerically evaluated the Van Vleck equation using zero field eigenfunctions determined via the diagonalization of

$$\hat{\mathcal{H}} = \Delta_{\text{ax}} \left[ \frac{1}{\hbar^2} \hat{L}_z^2 - \frac{2}{3} \hat{1} \right] + \frac{1}{2} \frac{\Delta_{\text{rh}}}{\hbar^2} [\hat{L}_+^2 + \hat{L}_-^2] + \frac{\tilde{g}_L \kappa \lambda_{\text{so}}}{\hbar^2} \hat{\mathbf{L}} \cdot \hat{\mathbf{S}} \quad (23)$$

carried out in a fictitious  $\tilde{L} = 1$  representation of the cubic field  $T$  state. The parameter  $\kappa = 0.9$ , incorporating the covalency reduction and the effect of the  $^4\text{F}$ – $^4\text{P}$  configuration interaction, is fixed, along with a  $T$  state orbital  $g$ -factor<sup>47,54</sup> of  $\tilde{g}_L = -\frac{3}{2}$ . The values of  $\Delta_{\text{ax}}$  and  $\Delta_{\text{rh}}$ , corresponding to the strengths of the axial and rhombic crystal field distortions, are determined by fitting the principal components of the predicted bulk magnetic susceptibility tensor to the measured values as a function of

temperature. We have reanalyzed Narath's data<sup>70</sup> with nearly the same method,<sup>71</sup> assuming that the bulk magnetic susceptibility tensor  $\chi_m$  is proportional to the molecular susceptibility tensor according to

$$\chi_m = \frac{N_A}{V_M} \chi, \quad (24)$$

where  $N_A$  is Avogadro's number and  $V_M$  is the molar volume. Our best fit to his data<sup>72</sup> gives

$$\Delta_{\text{ax}} = -125 \text{ meV}, \quad \Delta_{\text{rh}} = -43 \text{ meV},$$

which nominally gives  $E_1 = 87$  meV. This is shown in Fig. S7 of the [supplementary material](#). In addition, there is a large zero field splitting which splits the spin quartet into two Kramers doublets separated by 15.7 meV, which is on the order of  $k_B T$  at 300 K. This structure is illustrated in Fig. S4. With the crystal field assumed to be temperature independent, we extrapolate  $\chi$  to  $T = 300$  K with our first-order numerical treatment using the full Van Vleck equation, Eq. (14). At 300 K, the  $x$ -axis of the PAS is oriented along the Co–O bond and the  $z$ -axis is oriented along the short Co–Cl bond. The overall effects of cooperative magnetism are not significant in the paramagnetic phase of this compound, with  $|T_C| \approx 0$  K.

Figure 3 shows the exceptionally large molecular susceptibility anisotropy resulting from the quasi-first order contribution of the orbital moment to the magnetic properties of the  $\text{Co}^{2+}$  ion in this compound. The value of  $\chi_{xx}$  is nearly 250% above the spin-only prediction with  $S = 3/2$  and nearly 350% larger than  $\chi_{zz}$ , which falls nearly 30% below the spin-only value. Interestingly, our extrapolation to room temperature predicts interchange of the Haeberlen-convention labeled  $z$ - and  $x$ -axes near 163 K as a result of the PAS component of lowest magnitude exhibiting only a weak temperature dependence, which can be seen in Fig. S7 of the [supplementary material](#). The large negative deviations of  $\chi_{zz}$  component would be difficult to realize at high temperatures in the second-order spin-orbit dequenched approximation of Eq. (18) as they must result from the **D** term when  $\lambda_{\text{so}} < 0$ . Such an approximation of the magnetism of  $\text{CoCl}_2 \cdot 2\text{D}_2\text{O}$  would not have been adequate for predicting NMR shift tensors.

### 4. $\text{NiCl}_2 \cdot 2\text{D}_2\text{O}$ : $\text{Ni}^{2+}$ , $^3\text{F}$

The free ion ground state of  $\text{Ni}^{2+}$  is  $^3\text{F}$ . The splitting of the  $\text{F}$  term in the cubic field gives the same states as for  $\text{Co}^{2+}$ , but the order of energy is inverted. As shown in Fig. S5 of the [supplementary material](#), the  $A_{2g}$  orbital singlet now comprises the ground manifold, with the next  $T_{2g}$  orbital triplet lying some 1000 meV higher, which is split further by the axial and rhombic crystal field distortions. The spin degeneracy of the ground and excited states is, as usual, lifted by the spin-orbit coupling ( $\lambda_{\text{so}}(\text{Ni}^{2+}) = -40$  meV).<sup>67</sup> The conditions allowing use of Eq. (18) are well met. The dequenching tensor is approximately isotropic, as confirmed by the measurements of an isotropic  $g$ -tensor with  $g_{xx} = g_{yy} = g_{zz} = 2.23$  and a relatively small zero field splitting of around 0.07 meV near room temperature.<sup>73</sup> On the basis of

the  $g$ -tensor measurement, we find an isotropic dequenching tensor,

$$\Lambda_{xx} = \Lambda_{yy} = \Lambda_{zz} = -0.0029 \text{ meV}^{-1}.$$

We also take a Weiss constant<sup>74</sup> of  $T_c = +11$  K for the effective temperature used in Eq. (18). As for the  $\text{Mn}^{2+}$  compound, the isotropic orbital dequenching tensor leads to an isotropic molecular susceptibility tensor, as shown in Fig. 3. Both the  $g$  term and Weiss correction contribute to positive deviations from the spin-only prediction of the susceptibility, giving a net deviation of about 30% for each component.

### 5. $\text{CuCl}_2 \cdot 2\text{D}_2\text{O}$ : $\text{Cu}^{2+}$ , $^2\text{D}$

The free ion ground state of  $\text{Cu}^{2+}$  is  $^2\text{D}$ . After imposition of the crystal field, the ground state term has  $A_g$  symmetry, as shown in Fig. S6 of the [supplementary material](#). In spite of a significant spin-orbit coupling constant,  $\lambda_{\text{so}}(\text{Cu}^{2+}) = -103 \text{ meV}$ ,<sup>67</sup> matrix elements of  $\hat{\mathbf{L}}$  connecting the first excited  $A_g$  electronic state are zero, and the next set of electronic excited states which can contribute to orbital dequenching originate from an orbital triplet that is approximately 1550 meV removed from the ground state.<sup>75</sup> Since  $S = 1/2$ , there is no zero field splitting and Eq. (18) is valid. The  $g$ -tensor of the dihydrate complex has been measured precisely,<sup>76</sup> and from it, we determine

$$\Lambda_{zz} = -0.00160 \text{ meV}^{-1},$$

$$\Lambda_{yy} = -0.00048 \text{ meV}^{-1},$$

$$\Lambda_{xx} = -0.00022 \text{ meV}^{-1}.$$

As with  $g$ , the  $z$ -axis of the PAS coincides with the long Cu–Cl bond and the  $x$ -axis is aligned with the Cu–O bonds. There are two types of chains in this compound which differ in their orientation of  $g$  with respect to the crystal frame, requiring that the dipolar summation in Eq. (12) is carried out over two sublattices, one for each orientation of  $\chi$ . The effects of cooperative magnetism are not significant in the paramagnetic phase of this compound. As expected, the molecular susceptibility tensor is anisotropic—to a lesser extent than the Co and Fe cases—with small positive deviations from the spin-only prediction visible in Fig. 3.

### D. Water coordination and motional models

The  $^2\text{H}$  NMR spectral analysis is complicated by rapid molecular motion of the water molecule which occurs on a faster time scale than the NMR experiment. Since the shifting  $d$ -echo spectrum of all dihydrate salts are exceptionally well-modeled using a single deuteron site, we infer that there is only motional disorder *over well-defined positions* which is fast on the NMR time scale. In the presence of such motional averaging, even if a detailed motional model is known, there will be loss of information about the “instantaneous” tensor, i.e., the tensor in the absence of motion. Thus, the impact of such dynamics must be carefully considered when interpreting measured tensor parameters.

The water ligands in crystalline hydrates possess internal, rotatory, and translatory vibrational modes<sup>77</sup> which result in slight averaging of the instantaneous NMR parameters.<sup>78,79</sup>

Our motional model begins with the assumption that the averaging effects of the vibrations can be ignored. The ligands generally undergo internal deuteron exchange due to the activation of a two-fold hopping motion about the  $C_2$  site-symmetry axis, as illustrated in Fig. 4(a). This motion is a hallmark of water ligands and is always present at room temperature regardless of coordination. The complete details of the water ligand motion, however, depend on the geometry of its coordination to the metal center as well as steric and electrostatic interactions with neighboring atoms, both of which strongly influence each other. Water ligand coordination is generally classified in terms of lone pair model of coordination into trigonal, pyramidal, and tetrahedral in solid hydrates.<sup>77</sup> In trigonal coordination, the bisector of the two lone pairs on oxygen is directed toward the metal; in pyramidal coordination, only one lone pair on oxygen is directed towards the metal; and in tetrahedral coordination, lone pairs are directed toward different metals.

The crystal structure<sup>80–83</sup> and magnetic properties<sup>28,64,84,85</sup> of the iron-group halide dihydrates were investigated extensively in the 1960s. In the isostructural salts,  $\text{CoCl}_2 \cdot 2\text{D}_2\text{O}$ ,  $\text{FeCl}_2 \cdot 2\text{D}_2\text{O}$ , and  $\text{MnCl}_2 \cdot 2\text{D}_2\text{O}$ , planar  $\text{MCl}_2$  chains propagate along the  $c$ -axis of the monoclinic ( $C2/m$ ) crystal frame forming a polymeric linear chain. Water molecules are coordinated to the metal at the two remaining octahedral sites and adopt a trigonal configuration. Adjacent  $\text{MCl}_2$  chains along the  $b$ -axis are held together by hydrogen bonds as illustrated in Fig. 5. This hydrogen bonding to chlorine on two adjacent chains leads to the water molecule in the  $[\text{M}(\text{D}_2\text{O})_2\text{Cl}_4]$  cluster being nearly coplanar with O–M–Cl involving the shortest metal-chlorine bonds of the cluster. A later neutron diffraction study by Schneider and Weitzel<sup>86</sup> at 4.2 K in  $\text{FeCl}_2 \cdot 2\text{H}_2\text{O}$  confirmed that the hydrogen bonding leads to the Cl atoms of neighboring chains being coplanar with the hydrogen of the ligand.

Similarly, the structure of  $\text{CuCl}_2 \cdot 2\text{D}_2\text{O}$  determined by X-ray<sup>88</sup> and neutron diffraction<sup>83,89</sup> consists of columns of planar  $\text{CuCl}_2 \cdot 2\text{D}_2\text{O}$  molecules stacked along the  $b$ -axis of the orthorhombic ( $Pmna$ ) crystal frame. The columns are held

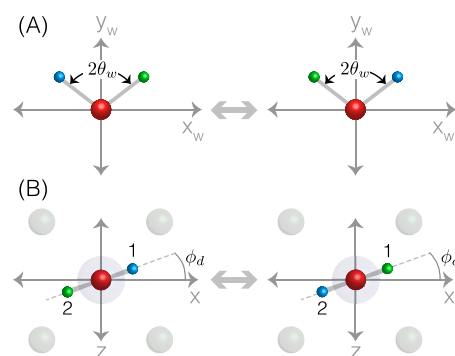


FIG. 4. (a) Bisector flipping of a water ligand in a *ligand-fixed* frame where the water molecule lies in the  $x$ - $y$  plane with the oxygen atom at the origin and the  $y$ -axis lies along the D–O–D angle bisector. (b) Bisector flipping of a trigonally coordinated water ligand in a *lattice-fixed* frame where oxygen defines the origin, the  $y$ -axis lies along the metal–oxygen bond, and the  $x$  axis is in the plane of the metal–oxygen bonds of the chain. Relative atomic radii and distances are not to scale.

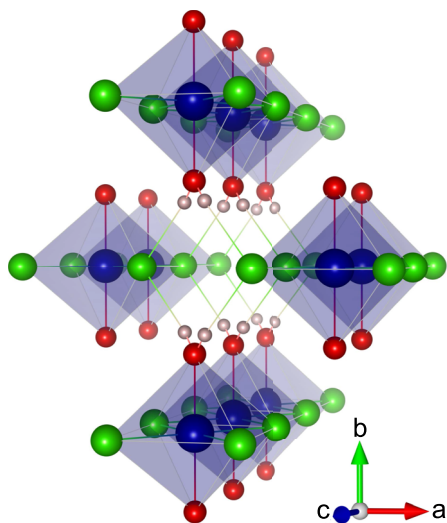


FIG. 5. Illustration<sup>87</sup> of the polymeric linear  $\text{MCl}_2$  chains and the trigonally coordinated water ligands with their hydrogen bonding in a fragment of the  $\text{CoCl}_2 \cdot 2\text{D}_2\text{O}$  structure.

together by hydrogen bonds  $\text{O}-\text{H} \cdots \text{Cl}$  with each Cl accepting two hydrogen bonds at nearly right angles to each other. The water ligand is trigonally coordinated to the metal and the hydrogen bonding with chlorine also leads to the water molecule being nearly coplanar with  $\text{Cl}-\text{Cu}-\text{O}$  involving the shortest metal-chlorine bonds of the  $[\text{Cu}(\text{D}_2\text{O})_2\text{Cl}_4]$  cluster. In a previous work<sup>29</sup> on  $\text{CuCl}_2 \cdot 2\text{D}_2\text{O}$ , we found that a motional model of trigonally coordinated water with simple bisector flipping and the water molecule coplanar with the Cl atoms of neighboring chains gave good agreement for the experimental quadrupolar tensor and paramagnetic shift tensor calculated with the point-dipole approximation of Sec. III A.

The structure of  $\text{NiCl}_2 \cdot 2\text{H}_2\text{O}$  is somewhat different. Morosin<sup>82</sup> found that  $\text{NiCl}_2$  chains propagate along the two-fold axis of the monoclinic lattice forming a corrugated polymeric chain as illustrated in Fig. 6. The  $\text{NiCl}_4$  planes of

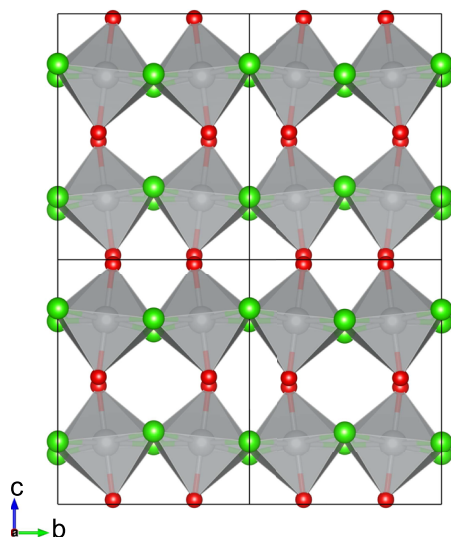


FIG. 6. View down the  $a$  axis of the  $\text{NiCl}_2 \cdot 2\text{D}_2\text{O}$  crystal structure. Hydrogen atoms are not shown.

adjacent Ni atoms in the chains are tipped with respect to each other, forming an angle of  $167.94^\circ$  between the two  $\text{NiCl}_4$  planes. Hydrogen atoms could not be located and to date are unpublished. Morosin speculated that hydrogen bonding to chlorine on neighboring chains may be weakly bi- and tri-furcated and are located along the bisector of the  $\text{Cl}-\text{O}-\text{Cl}$  angle while the other causes the oxygen-hydrogen vector to point toward the center of a triangle defined by an oxygen and a chlorine on an adjacent chain and the nearer oxygen on the same chain. This suggests a pyramidal water ligand to the metal.

In light of these structural data, we examined a number of motional models involving trigonal and pyramidal water coordinations. The two specific models most consistent with the experimental results are presented here. In these models, we start with a general expression for the observed quadrupolar coupling (efg) or shift tensor of a deuteron undergoing exchange between  $N$  distinct sites and given by the average

$$\langle \mathbf{R}^{(\xi)} \rangle = \sum_{j=1}^N p_j \mathbf{R}_j^{(\xi)}, \quad (25)$$

where  $\mathbf{R}_j^{(\xi)}$  is the NMR interaction tensor of the  $j$ th deuteron site and  $p_j$  is the relative site occupancy such that  $\sum_j p_j = 1$ . The orientation of the principal axis system of the motional averaged efg and shift tensors are determined in a *lattice-fixed frame*, here chosen such that oxygen defines the origin, the  $y$ -axis lies along the metal-oxygen bond, and the  $x$ -axis is in the plane of the metal-oxygen bonds of the  $\text{MCl}_2$  chain.

The  $N$ -site exchange leads to a 2D correlation spectrum characterized by a single site, as seen in Fig. 2. Note that there is one crystallographically distinct oxygen site in the crystal structures of all salts considered here. Whether neutron data are available or not, our goal is to use the 2D correlation spectrum and the heavy atom lattice symmetry to determine the number and location of crystallographically distinct hydrogen sites around oxygen and their fractional occupancies.

The efg at each deuteron arises predominantly from its  $\text{O}-\text{D}$  bond in the water ligand. While the motional averaged efg tensor is sensitive to the ligand-metal coordination geometry and ligand motion, it is not sensitive to the absolute ligand orientations relative to the crystal frame since the  $\text{O}-\text{D}$  bond, that is, the dominant source of the efg, moves with the water ligand. On the other hand, the dominant source of the shift tensor at each deuteron site, i.e., the paramagnetic transition metal atoms, is fixed in the lattice and independent of ligand motion. Thus, the shift tensor at each deuteron site, as well as the motional average, is sensitive to the absolute ligand orientations. In this context, the single site nature of the 2D spectrum then becomes a critical constraint as the motional averaging among the crystallographically distinct hydrogen sites on each oxygen must lead to isometric tensors in the crystal frame. Under these constraints, it can be shown (Appendix C) that *each set of crystallographically distinct hydrogen sites and their fractional occupancies can be propagated to all other sites in accordance with the overall heavy atom lattice symmetry.*

## 1. Trigonal motional model

In the case of trigonal water coordination, we only consider deuteron exchange by way of 180° flips about the bisector axis illustrated in Fig. 4(b). To model this motion, we take  $N = 2$  and  $p_1 = p_2 = 0.5$  in Eq. (25) obtaining the average tensor

$$\langle \mathbf{R}^{\{\xi\}} \rangle = \frac{1}{2} [\mathbf{R}_1^{\{\xi\}} + \mathbf{R}_2^{\{\xi\}}]. \quad (26)$$

To calculate the average efg tensor, it is convenient to begin in the *ligand-fixed frame*, illustrated in Fig. 4(a), where we first define a unit vector along the O–D bond for the first deuteron as

$$\hat{\mathbf{r}}_1 = \sin \theta_w \hat{\mathbf{x}}_w + \cos \theta_w \hat{\mathbf{y}}_w, \quad (27)$$

where  $\theta_w$  is half the D–O–D bond angle. The position of the second deuteron site is related by an active rotation about the  $y$ -axis of the ligand-fixed frame by  $\pi$ , with  $\hat{\mathbf{r}}_2 = \mathcal{D}_{y_w}(\pi) \hat{\mathbf{r}}_1$ . The axially symmetric efg tensor of each deuteron site,  $\mathbf{A}_i^{\{q\}}$ , can be expressed as

$$\mathbf{A}_i^{\{q\}} = \frac{\zeta_q}{2} [3\hat{\mathbf{r}}_i \otimes \hat{\mathbf{r}}_i - \mathbf{1}], \quad (28)$$

where  $\zeta_q$  is the instantaneous efg tensor anisotropy. The motional averaged efg tensor  $\langle \mathbf{A}^{\{q\}} \rangle$  is given by

$$\langle \mathbf{A}^{\{q\}} \rangle = \frac{1}{2} [\mathbf{A}_1^{\{q\}} + \mathbf{A}_2^{\{q\}}]. \quad (29)$$

This leads to the nonzero Cartesian components,

$$\langle A_{xx}^{\{q\}} \rangle = \frac{\zeta_q}{2} [3 \sin^2 \theta_w - 1], \quad (30)$$

$$\langle A_{yy}^{\{q\}} \rangle = \frac{\zeta_q}{2} [3 \cos^2 \theta_w - 1], \quad (31)$$

$$\langle A_{zz}^{\{q\}} \rangle = -\frac{\zeta_q}{2}, \quad (32)$$

in the ligand-fixed frame. Through the passive transformation

$$\langle \mathbf{R}^{\{q\}} \rangle = \mathcal{D}_{y_w}^{-1}(-\phi_d) \langle \mathbf{A}^{\{q\}} \rangle \mathcal{D}_{y_w}(-\phi_d), \quad (33)$$

the motional averaged efg tensor is expressed in the lattice-fixed frame.

When the bond angle of the water ligand is in the range  $90^\circ < 2\theta_w \lesssim 109.47^\circ$ , we find  $|\langle A_{zz}^{\{q\}} \rangle| \geq |\langle A_{xx}^{\{q\}} \rangle| \geq |\langle A_{yy}^{\{q\}} \rangle|$ , indicating that the PAS of the motional averaged efg coincides with the ligand-fixed frame. We denote the motional averaged efg tensor expressed in its PAS by  $\langle \rho^{\{q\}} \rangle$ . For the present case, we have  $\langle \rho^{\{q\}} \rangle = \langle \mathbf{A}^{\{q\}} \rangle$ ,

$$\langle \zeta_q \rangle = -\zeta_q/2, \quad \text{and} \quad \langle \eta_q \rangle = -3 \cos 2\theta_w. \quad (34)$$

On the other hand, when  $2\theta_w \gtrsim 109.47^\circ$ , we find  $|\langle A_{xx}^{\{q\}} \rangle| \geq |\langle A_{zz}^{\{q\}} \rangle| \geq |\langle A_{yy}^{\{q\}} \rangle|$  and the PAS of the motional averaged efg is defined by interchange of the  $x$ - and  $z$ -axes of the ligand-fixed frame,

$$\langle \rho^{\{q\}} \rangle = \mathcal{D}_{y_w}^{-1}(\pi/2) \langle \mathbf{A}^{\{q\}} \rangle \mathcal{D}_{y_w}(\pi/2). \quad (35)$$

Here we find

$$\begin{aligned} \langle \zeta_q \rangle &= -\frac{\zeta_q}{2} (3 \sin^2 \theta_w - 1), \\ \langle \eta_q \rangle &= \frac{3 \cos^2 \theta_w}{2 - 3 \cos^2 \theta_w}. \end{aligned} \quad (36)$$

When  $2\theta_w$  is the tetrahedral angle,  $\sim 109.47^\circ$ , we obtain  $\langle \zeta_q \rangle = \zeta_q/2$  and  $\langle \eta_q \rangle = 1$ . On the basis of the experimentally measured motional averaged  $\langle C_q \rangle$  and  $\langle \eta_q \rangle$  values in Table I and the assumption that the instantaneous  $C_q$  value of 230 kHz for the  $^2\text{H}$  in the O–D bond of water and a D–O–D angle near  $109.47^\circ$ , we find that the trigonal motional model is consistent for the Mn, Fe, Co, and Cu salts with  $\langle \zeta_q \rangle \approx \zeta_q/2$  and  $\langle \eta_q \rangle \approx 1$ .

The paramagnetic shift tensor from Eq. (12) is calculated in the lattice-fixed frame. In this frame, the separation vectors for the two deuteron sites are given by

$$\begin{aligned} \mathbf{r}_{1,k} &= \mathbf{r}_k - \mathcal{D}_y(\phi_d) \mathbf{r}_1, \\ \mathbf{r}_{2,k} &= \mathbf{r}_k - \mathcal{D}_y(\phi_d + \pi) \mathbf{r}_1, \end{aligned} \quad (37)$$

where  $\mathbf{r}_1 = r_{\text{OD}} \hat{\mathbf{r}}_1$ , with  $r_{\text{OD}}$  equal to the O–D bond length, and  $\mathbf{r}_k$  represents the coordinates of the  $k$ th dipole source. The active rotation of  $\mathbf{r}_1$  by  $\mathcal{D}_y(\phi_d)$ , where  $\phi_d$  is the dihedral angle, sets the orientation of the trigonally coordinated ligand in the lattice-fixed frame.

The motional averaged paramagnetic shift tensor in the lattice-fixed frame,  $\langle \mathbf{R}^{\{P\}} \rangle$ , can be found by calculating the instantaneous paramagnetic shift tensors  $\mathbf{R}_1^{\{P\}}$  and  $\mathbf{R}_2^{\{P\}}$  and averaging according to Eq. (26). A  $C_2$  point symmetry of the lattice with respect to the  $y$ -axis of the lattice-fixed frame, i.e., the water bisector, is present for all salts with trigonally coordinated waters, i.e.,  $\text{CuCl}_2 \cdot 2\text{D}_2\text{O}$ ,  $\text{CoCl}_2 \cdot 2\text{D}_2\text{O}$ ,  $\text{FeCl}_2 \cdot 2\text{D}_2\text{O}$ , and  $\text{MnCl}_2 \cdot 2\text{D}_2\text{O}$ . With this  $C_2$  point symmetry, we have  $\mathbf{r}_{2,k} = \mathcal{D}_y(\pi) \mathbf{r}_{1,k}$  and obtain

$$\langle \mathbf{R}^{\{P\}} \rangle = \frac{1}{2} [\mathbf{R}_1^{\{P\}} + \mathcal{D}_y(\pi) \mathbf{R}_1^{\{P\}} \mathcal{D}_y^{-1}(\pi)]. \quad (38)$$

With this relation, we only need to calculate the point dipole sum of Eq. (12) for one deuteron site.

Through the passive transformation

$$\langle \mathbf{A}^{\{P\}} \rangle = \mathcal{D}_y^{-1}(\phi_d) \langle \mathbf{R}^{\{P\}} \rangle \mathcal{D}_y(\phi_d), \quad (39)$$

the motional averaged paramagnetic shift tensor in the lattice-fixed frame is expressed in the ligand-fixed frame. If  $2\theta_w \lesssim 109.47^\circ$ , then the ligand-fixed frame coincides with the PAS of the motional averaged efg tensor. When  $2\theta_w \gtrsim 109.47^\circ$ , an additional  $\pi/2$  rotation about  $y_w$  is needed to bring the shift tensor into the PAS of the motional averaged efg tensor, which is the case for  $\text{CuCl}_2 \cdot 2\text{D}_2\text{O}$ . The relative orientation of the efg and shift tensors is then determined by a numerical diagonalization of the shift tensor, and the Euler angles ( $\langle \alpha_{\text{rel}} \rangle$ ,  $\langle \beta_{\text{rel}} \rangle$ ,  $\langle \gamma_{\text{rel}} \rangle$ ) define the passive rotation which takes the PAS of the paramagnetic shift tensor into that of the efg.

## 2. Pyramidal motional model

In the case of  $\text{NiCl}_2 \cdot 2\text{D}_2\text{O}$ , we adopt a model where the water ligands are in pyramidal coordination and undergoing



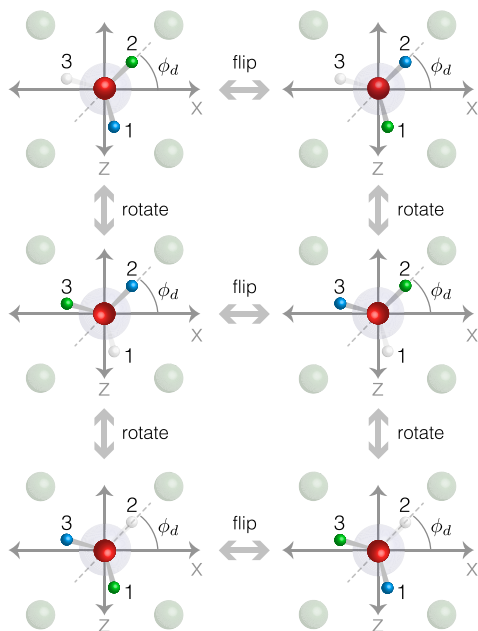


FIG. 7. Combined bisector flipping and three-fold rotation of a pyramidally coordinated water ligand in a *lattice-fixed frame* where oxygen defines the origin, the  $y$ -axis lies along the metal-oxygen bond, and the  $x$  axis is in the plane of the metal-oxygen bonds of the chain. Bisector flipping exchanges the two deuterons but maintains the overall ligand configuration, whereas the three-fold jumping motion changes the ligand configuration and carries the deuterons to unoccupied (white) sites. Deuteron sites are labeled according to Eq. (41). Relative atomic radii and distances are not to scale.

an exchange among three deuteron sites. The overall ligand motion can be seen as a combination of two types of motion: an exchange of deuterons through flipping about the bisector of the D–O–D angle and an exchange of deuterons through a three-fold rotation about the metal-oxygen bond, both illustrated in Fig. 7 in a lattice-fixed frame. Both types of motion are fast on the NMR time scale and lead to single motional averaged tensors.

To calculate the average efg tensor from this motion, we start in the lattice-fixed frame. A unit vector along the O–D

bond for the first deuteron can be written as

$$\hat{\mathbf{r}} = \frac{2}{\sqrt{3}} \sin \theta_w \hat{\mathbf{x}} + \left[ 1 - \frac{4}{3} \sin^2 \theta_w \right]^{1/2} \hat{\mathbf{y}}. \quad (40)$$

Note that  $2\theta_w < 120^\circ$  due to restrictions of pyramidal geometry. With this definition, the unit vectors defining the three deuteron sites in the lattice-fixed frame are

$$\begin{aligned} \hat{\mathbf{r}}_1 &= \mathcal{D}_y \left( \phi_d - \frac{2\pi}{3} \right) \hat{\mathbf{r}}, \\ \hat{\mathbf{r}}_2 &= \mathcal{D}_y(\phi_d) \hat{\mathbf{r}}, \\ \hat{\mathbf{r}}_3 &= \mathcal{D}_y \left( \phi_d + \frac{2\pi}{3} \right) \hat{\mathbf{r}}. \end{aligned} \quad (41)$$

Similar to Eq. (28), we calculate the efg tensor for each site in the lattice-fixed frame from these vectors,

$$\mathbf{R}_i^{(q)} = \frac{\zeta_q}{2} [3\hat{\mathbf{r}}_i \otimes \hat{\mathbf{r}}_i - \mathbf{1}]. \quad (42)$$

For the motionally averaged tensors in the lattice-fixed frame, we have

$$\langle \mathbf{R}^{(\xi)} \rangle = p_1 \mathbf{R}_1^{(\xi)} + p_2 \mathbf{R}_2^{(\xi)} + p_3 \mathbf{R}_3^{(\xi)}. \quad (43)$$

A motional average over all three sites with equal occupancies leads to an axially symmetric ( $\langle \eta_q \rangle = 0$ ) efg tensor, contrary to the experimentally observed  $\langle \eta_q \rangle \approx 1$ ; thus, equal occupancies must be eliminated as a possibility. To keep the assumption of pyramidal coordination, we must consider unequal occupancies of the three sites—a likely consequence of van der Waals interactions as well as hydrogen bonding between the water ligand and neighboring lattice sites. The closest of such interactions arise as neighboring water molecules are pushed together by the corrugation of the linear chains, which results in unequal gaps between oxygen atoms along the  $b$ -axis, as seen in Fig. 6.

With this in mind, Fig. 8 shows possible configurations of ligand  $O_1$  from Fig. 7, with a fixed value of  $\phi_d$ , interacting with neighboring ligand  $O'_1$ . These twenty possible pairwise ligand configurations avoid significant van der Waals overlaps of deuterons on adjacent water ligands. In each column are the

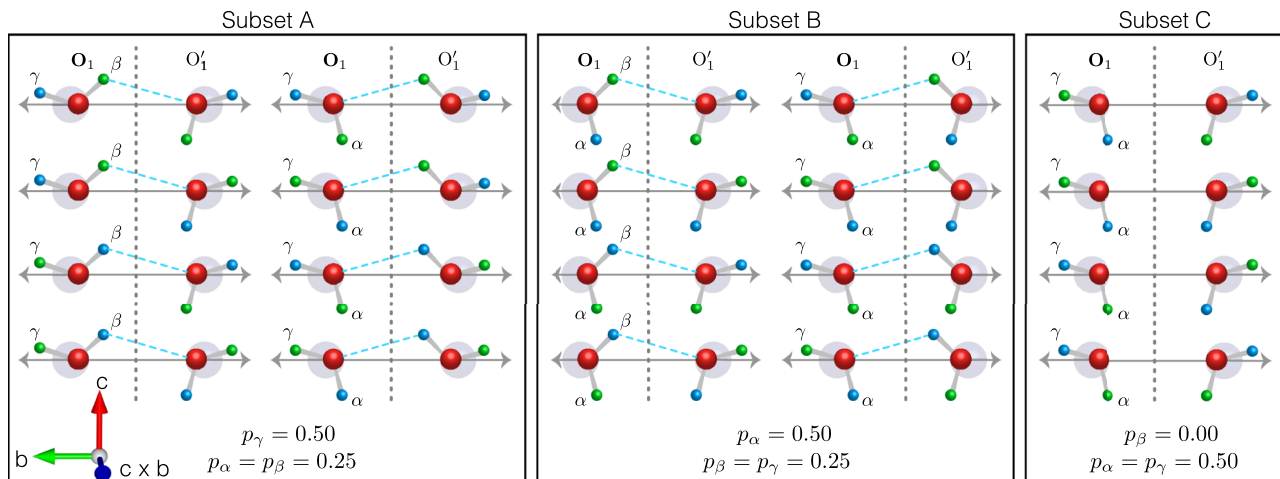


FIG. 8. Possible correlated ligand geometries of adjacent water molecules in pyramidal coordination in the  $\text{NiCl}_2 \cdot 2\text{D}_2\text{O}$  structure. The blue dashed lines represent hydrogen-bond interactions. The possibilities are divided into three subsets with different site occupancies. The black dotted line represents the edge of the unit cell. The ligands  $O_1$  and  $O'_1$  are related by a translation of one unit cell, followed by a reflection operation.

four bisector flipping exchange-equivalent configurations. The observation that only one site is needed to model the NMR spectrum suggests that we focus on combinations of columns that lead to the same motional average tensors for both  $O_1$  and  $O'_1$ . Careful inspection of Fig. 8 reveals that only equally weighted exchange between the configurations of the first and second columns or between the configurations of the third and fourth columns leads to the same motional average tensors for both  $O_1$  and  $O'_1$ . Thus, we further divide the configurations into three subsets, which are corralled in Fig. 8 along with the corresponding site occupancies for each subset. The single column of subset C, on its own, can be dismissed outright as it leads to a motional averaged value of  $|\langle\zeta_q\rangle/\zeta_q| \approx 0.5$  which is inconsistent with the experiment. All the remaining ways in which the three subsets can be combined with equal weights are given in Table III. Taking the water bond angle as equal to the tetrahedral angle, we can screen the feasibility of each subset combination by comparing their predicted values of  $|\langle\zeta_q\rangle/\zeta_q|$  and  $\langle\eta_q\rangle$  with experiment. We see that the equal contribution subset A+B, while reasonable in its prediction of  $|\langle\zeta_q\rangle/\zeta_q|$ , predicts a  $\langle\eta_q\rangle$  far below the experiment and can be eliminated. Similarly, equal contribution subsets A+C and B+C predict reasonable values of  $\langle\eta_q\rangle$  but are too large in their prediction of  $|\langle\zeta_q\rangle/\zeta_q|$  and can also be eliminated. Finally, equal contribution subset A+B+C is closer in its prediction of  $|\langle\zeta_q\rangle/\zeta_q|$  but too small in its prediction of  $\langle\eta_q\rangle$  and is thus eliminated. Hence, we find that subsets A or B are consistent with the experimental values of  $|\langle\zeta_q\rangle/\zeta_q|$  and  $\langle\eta_q\rangle$ . A more thorough screening of models, which considers weighted admixtures of subsets and leverages predictions of full correlation spectra for each case, is given in the [supplementary material](#). This analysis validates the conclusions drawn from Table III, and henceforth, we focus exclusively on the motional model of subsets A or B.

A common characteristic of subsets A and B is that one deuteron site is always occupied. In Fig. 8, the permanently occupied site is labeled  $\gamma$  in subset A and  $\alpha$  in subset B. To model this motion, we refer to Fig. 7 and only consider the top four configurations; that is, we ignore the bottom row. In doing this, we establish the convention that site “2” always represents the permanently occupied site ( $p_2 = 0.5$ ), and  $\phi_d$  becomes the fit parameter for determining the orientation of the permanently occupied site in the lattice-fixed frame. To

calculate the average efg tensor for this model, it is convenient to begin in a frame tilted away from the lattice-fixed frame by a rotation of  $\phi_d$  about the  $y$  axis of the lattice-fixed frame. In this tilted frame, the nonzero Cartesian components of the efg tensor are given by

$$\langle A_{xx}^{(q)} \rangle = \frac{\zeta_q}{8} (1 - 5 \cos 2\theta_w), \quad (44)$$

$$\langle A_{yy}^{(q)} \rangle = \zeta_q \cos 2\theta_w, \quad (45)$$

$$\langle A_{zz}^{(q)} \rangle = -\frac{\zeta_q}{8} (3 \cos 2\theta_w + 1), \quad (46)$$

$$\langle A_{xy}^{(q)} \rangle = \langle A_{yx}^{(q)} \rangle = \frac{3\zeta_q}{4} \sin \theta_w \left[ 1 - \frac{4}{3} \sin^2 \theta_w \right]^{1/2}. \quad (47)$$

This block diagonal  $\langle A^{(q)} \rangle$  tensor can be diagonalized and brought into its PAS by the passive rotation,

$$\langle \rho^{(q)} \rangle = \mathcal{W}^{-1} \langle A^{(q)} \rangle \mathcal{W}, \quad (48)$$

where  $\mathcal{W}$  consists of two successive coordinate system rotations according to

$$\mathcal{W} = \mathcal{D}_{z'}(\psi) \mathcal{D}_{x''}\left(\frac{\pi}{2}\right). \quad (49)$$

Here a rotation about the  $z'$ -axis of the tilted lattice frame diagonalizes  $\langle A^{(q)} \rangle$  and is followed by a rotation about the intermediate diagonal frame  $x''$ -axis, which brings the tensor into its PAS. The angle  $\psi$  is given by

$$\psi = \pi - \frac{1}{2} \cos^{-1} \left( \frac{26 \cos 2\theta_w - 2}{3u(\theta_w)} \right), \quad (50)$$

where

$$u(\theta_w) = \sqrt{2[19 - 4 \cos 2\theta_w + 17 \cos 4\theta_w]}^{1/2} \quad (51)$$

so that  $100^\circ \lesssim \psi \lesssim 125^\circ$  for  $90^\circ \leq 2\theta_w \lesssim 109.47^\circ$ . In this range,

$$\langle \zeta_q \rangle = \frac{2 + 6 \cos 2\theta_w + 3u(\theta_w)}{32}, \quad (52)$$

$$\langle \eta_q \rangle = \frac{3u(\theta_w) - 18 \cos 2\theta_w - 6}{3u(\theta_w) + 6 \cos 2\theta_w + 2}. \quad (53)$$

When  $2\theta_w$  is the tetrahedral angle,  $\sim 109.47^\circ$ , we obtain  $\langle \zeta_q \rangle = \zeta_q/\sqrt{8}$  and  $\langle \eta_q \rangle = 1$ .

We calculate the paramagnetic shift tensor in the lattice-fixed frame,  $\langle \mathbf{R}^{(P)} \rangle$ , where the separation vectors for the three deuteron sites as defined above are given by

$$\begin{aligned} \mathbf{r}_{1,k} &= \mathbf{r}_k - \mathcal{D}_y \left( \phi_d - \frac{2\pi}{3} \right) \mathbf{r}, \\ \mathbf{r}_{2,k} &= \mathbf{r}_k - \mathcal{D}_y(\phi_d) \mathbf{r}, \\ \mathbf{r}_{3,k} &= \mathbf{r}_k - \mathcal{D}_y \left( \phi_d + \frac{2\pi}{3} \right) \mathbf{r}, \end{aligned} \quad (54)$$

where  $\mathbf{r} = r_{OD}\hat{\mathbf{r}}$  and  $\mathbf{r}_k$  represents the coordinates of the  $k$ th dipole source. Through the passive transformation

$$\langle \mathbf{Q}^{(P)} \rangle = \mathcal{W}^{-1} \mathcal{D}_y^{-1}(\phi_d) \langle \mathbf{R}^{(P)} \rangle \mathcal{D}_y(\phi_d) \mathcal{W}, \quad (55)$$

we obtain  $\langle \mathbf{Q}^{(P)} \rangle$ , giving the components of the motional averaged paramagnetic shift tensor in the PAS of the motional averaged efg tensor. As before, the relative orientation of the

TABLE III. Ordered lists of occupancy parameters for equally weighted combinations of the configuration subsets shown in Fig. 8. Predicted values of  $|\langle\zeta_q\rangle/\zeta_q|$  and  $\langle\eta_q\rangle$  are given assuming that  $2\theta_w$  is the tetrahedral angle,  $109.47^\circ$ . The uncertainty in  $|\langle\zeta_q\rangle/\zeta_q|$  arises from an assumed  $\pm 6$  kHz normal uncertainty in the instantaneous  $C_q$  value of 230 kHz.

Subsets	$(p_\alpha, p_\beta, p_\gamma)$	$ \langle\zeta_q\rangle/\zeta_q $	$\langle\eta_q\rangle$
A	(0.25, 0.25, 0.5)	0.354	1
B	(0.5, 0.25, 0.25)	0.354	1
A+B	(0.375, 0.25, 0.375)	0.341	0.464
A+C	(0.333, 0.167, 0.5)	0.373	1
B+C	(0.5, 0.167, 0.333)	0.373	1
A+B+C	(0.4, 0.2, 0.4)	0.356	0.685
Experimental		$0.33 \pm 0.03$	$0.91^{+0.04}_{-0.01}$

efg and shift tensors is determined by a numerical diagonalization of the shift tensor and is defined as the passive transformation which takes the PAS of the paramagnetic shift tensor into that of the efg.

## IV. RESULTS AND DISCUSSION

### A. Comprehensive analysis of 2D spectra

We are now in a position to combine the results of Sec. III into a single comprehensive model for the 2D shifting- $d$  NMR spectrum. This comprehensive model requires (1) the heavy atom crystal structure, (2) the molecular magnetic susceptibility of the paramagnetic metal centers, (3) the extent of magnetic point dipole delocalization away from metal centers onto coordinating ligands, (4) the coordination type and corresponding motional model for the water ligand, and (5) the geometric details on the water ligand:  $r_{OD}$ ,  $\theta_w$ , and  $\phi_d$ . Of course, the adjustable parameters associated with all requirements taken together is an inordinate number of degrees of freedom for any experimental line shape analysis. Additional constraints need to be imposed. Therefore, our analysis assumes the use of known heavy atom crystal structures and the molecular magnetic susceptibilities predicted using bulk magnetic susceptibility or other spectroscopic measurements. Additionally, we chose to fix the values of  $r_{OD}$  and  $\theta_w$  based on the more reliable neutron diffraction<sup>90</sup> results from  $\text{CoCl}_2 \cdot 2\text{D}_2\text{O}$  at 77 K. As suggested by these data, we also hold  $\phi_d \approx 55^\circ$  fixed to enforce  $\text{D}_2\text{O}/\text{Cl}$  planarity for the trigonal systems ( $M = \text{Mn}, \text{Fe}, \text{Co}, \text{and Cu}$ ), as illustrated in Fig. 5. A comparison of ligand geometries obtained from diffraction on  $\text{FeCl}_2 \cdot 2\text{D}_2\text{O}$ ,  $\text{CoCl}_2 \cdot 2\text{D}_2\text{O}$ , and  $\text{CuCl}_2 \cdot 2\text{D}_2\text{O}$  is given in Table S-IX of the [supplementary material](#). Note that this is in spite of the motional model predictions from experimental  $|\langle \zeta_q \rangle / \zeta_q|$  and  $\langle \eta_q \rangle$  giving  $2\theta_w$  values that are  $4^\circ$ – $6^\circ$  larger for all salts—with the exception of  $\text{CuCl}_2 \cdot 2\text{D}_2\text{O}$ —as shown in Table S-X of the [supplementary material](#). Thus, the values of  $r_{OD} = 0.98 \text{ \AA}$  and  $2\theta_w = 103.0^\circ$  are used for all salts analyzed here except  $\text{CuCl}_2 \cdot 2\text{D}_2\text{O}$ , where Engberg's x-ray and neutron data refinement values of  $r_{OD} = 0.948 \text{ \AA}$  and  $2\theta_w = 111.4^\circ$  are used.<sup>83,89</sup>

#### 1. $\text{CuCl}_2 \cdot 2\text{D}_2\text{O}$

Here we examine the performance of our comprehensive model using various point dipole configurations with increasing delocalization to predict the shifting- $d$  spectrum for  $\text{CuCl}_2 \cdot 2\text{D}_2\text{O}$ . In Fig. 2(a) is the fit of the experimental spectrum allowing the tensor parameters to vary freely, that is, without constraints of the comprehensive model, along with the resulting residuals spectrum associated with the best-fit  $\chi^2_{\text{red}}$  value of 22.80. In the first column of Fig. 9 is the best fit of the experimental spectrum using a comprehensive model with trigonal coordination/motion and a point dipole configuration where sources are placed only at Cu centers. The disagreement with the experiment, as highlighted by the residuals below and a  $\chi^2_{\text{red}}$  value rising to 144.2, is striking. In previous work,<sup>29</sup> it was shown that a comprehensive model for the  $\text{CuCl}_2 \cdot 2\text{D}_2\text{O}$  spectrum can be systematically improved by placing dipoles in regions where the spin density is expected to delocalize.

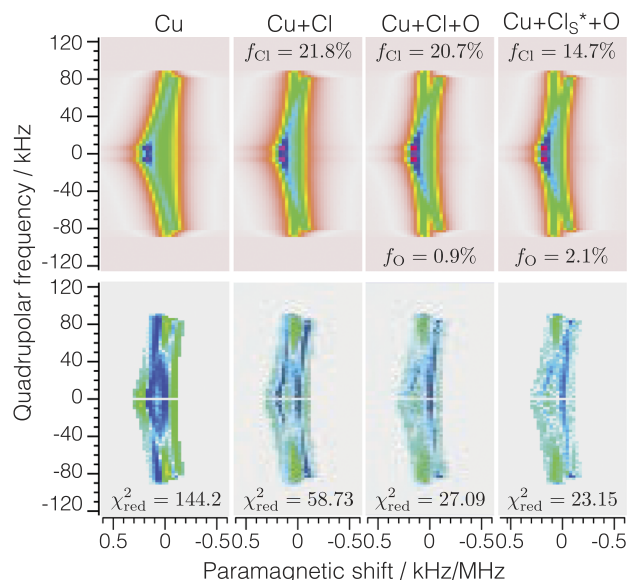


FIG. 9. On the top row is a comparison of the best fit shifting- $d$  spectrum predicted with various point dipole configurations for  $\text{CuCl}_2 \cdot 2\text{D}_2\text{O}$ . On the bottom row are the residual plots calculated with the experimental spectra. The quadrupolar parameters  $\langle C_q \rangle$  and  $\langle \eta_q \rangle$  were taken from the best fit of the experimental data. The line shape was refit to optimize the intensity, isotropic shift, and degree of line broadening for the paramagnetic shift dimension for each fixed set of calculated paramagnetic shift tensor parameters.

The optimum delocalization was determined by a least squares fit that minimizes error in the nontrivial molecular frame spherical components  $\langle R_{2,0}^{(P)} \rangle$  and  $\langle R_{2,-2}^{(P)} \rangle$  relative to the experimentally derived components. Delocalization of point dipoles onto the two chlorines associated with the shortest Cu–Cl bond,<sup>27</sup> as shown in the second column, gives a marked improvement with  $\chi^2_{\text{red}}$  dropping by a factor of two, down to 58.73. Still better improvement is obtained with added delocalization onto the oxygen of the water ligands, as seen in the third column, with  $\chi^2_{\text{red}}$  dropping to 27.1. The best agreement, however, is obtained with oxygen delocalization and the chlorine sources pushed  $0.9 \text{ \AA}$  away from the metal along the direction of the shortest Cu–Cl bond, in imitation of the antibonding character of the singly occupied molecular orbital ( $\text{Cu}+\text{Cl}_S^*+\text{O}$  model). This is seen in the final column where  $\chi^2_{\text{red}}$  approaches a value nearly identical to the fit in Fig. 2(a) where the shift tensor parameters were allowed to vary freely. Any further attempts to improve the point dipole configuration, such as the previously described SOMO-10 model,<sup>29</sup> would only lead to changes within the error and noise of the line shape model and were not pursued.

#### 2. Isostructural salts: $\text{CoCl}_2 \cdot 2\text{D}_2\text{O}$ , $\text{FeCl}_2 \cdot 2\text{D}_2\text{O}$ , and $\text{MnCl}_2 \cdot 2\text{D}_2\text{O}$

In the case of the isostructural salts with  $M = \text{Co}, \text{Fe}, \text{and Mn}$ , the use of a comprehensive model with point dipoles positioned only on metal centers, corresponding to the source configuration of Fig. 10(a), gives considerably better agreement with the experimental line shapes, as shown in the first columns of Figs. 11(a)–11(c), when compared to the first column of Fig. 9 in the  $\text{CuCl}_2 \cdot 2\text{D}_2\text{O}$  case. Physically, this is consistent with the periodic trend predicting that the bonding between the ligands and metal cation takes on increasingly ionic

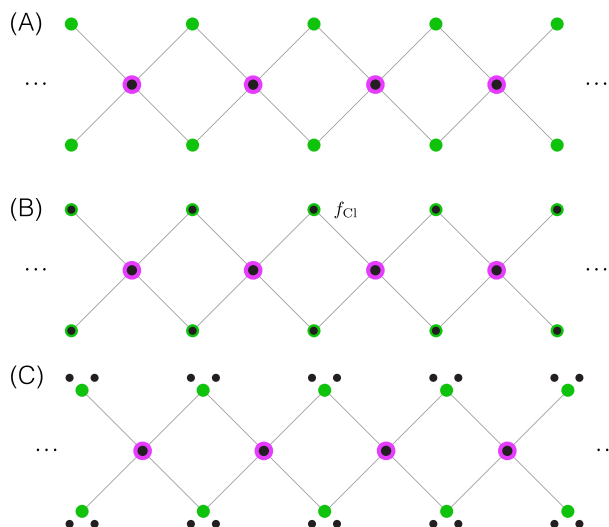


FIG. 10. Configuration of point dipole sources located at (a) metal nuclei, (b) metal and chlorine nuclei, and (c) metal centers and chlorine  $\sigma^*$ -type antibonding orbital configuration with respect to the primary  $\text{MCl}_2$  polymeric chain. From this vantage point, the crystal frame  $b$ -axis is perpendicular to the page. The amplitude of the metal sources becomes  $f_M = 1 - 2f_{\text{Cl}}$  for cases (b) and (c). When delocalization to oxygen atoms is included,  $f_M = 1 - 2f_{\text{Cl}} - 2f_{\text{O}}$ .

character along the iron group<sup>82</sup> moving from  $\text{Cu}^{2+}$  to  $\text{Mn}^{2+}$ . Nevertheless, some degree of covalency is present, leading to detectable effects in EPR and  $^{57}\text{Fe}$  Mössbauer spectra.<sup>91</sup>

The good agreement of the comprehensive model with point dipoles placed only at metal sites validates our use of molecular susceptibility tensors calculated with the crystal field approach. Not only the magnitude but also the susceptibility tensor orientation plays a critical role in determining the shift tensor. For example, in the case of  $\text{CoCl}_2 \cdot 2\text{D}_2\text{O}$ , rotating the susceptibility tensor by  $\pi/2$  about its principal  $y$ -axis leads to the predicted values of  $\langle \zeta_P \rangle = -802$  ppm and  $\langle \eta_P \rangle = 0.958$ , in stark contrast with the experiment.

We explore other dipole source delocalization configurations illustrated in Fig. 10 where delocalization parameters are optimized as described in the Cu case. In all three cases, we find only modest but consistent improvement from delocalization onto chlorine nuclei, corresponding to the source configuration of Fig. 10(b), and visualized in the second columns of Figs. 11(a)–11(c). The extent of delocalization required is significantly smaller in comparison to the values  $f_{\text{Cl}} > 10\%$  required to obtain good agreement in the Cu case. This is consistent with our interpretation of greater ionic character to the bonding interactions in the earlier members of the iron group.

Further refinements of the source configurations do not lead to consistent improvement. The anti-bonding chlorine configuration of Fig. 10(c) does lead to improvement for  $\text{FeCl}_2 \cdot 2\text{D}_2\text{O}$  [ $f_{\text{Cl}^*} = 6.5\%$ ,  $\chi_{\text{red}}^2 = 10.28$ , not shown in Fig. 11(b)] and  $\text{MnCl}_2 \cdot 2\text{D}_2\text{O}$  [Fig. 11(c)] when compared to the metal-only source model, although the gain is meager for the latter case. For  $\text{CoCl}_2 \cdot 2\text{D}_2\text{O}$ ,  $\chi_{\text{red}}^2$  is raised for any  $f_{\text{Cl}^*} > 0$ . Whereas delocalization onto oxygen was crucial for obtaining the experimental negative value of  $\langle \zeta_P \rangle$  for  $\text{CuCl}_2 \cdot 2\text{D}_2\text{O}$ , supplementing the configurations of Figs. 10(a) and 10(b) with sources at oxygen exacerbates agreement for  $\text{CoCl}_2 \cdot 2\text{D}_2\text{O}$  and  $\text{MnCl}_2 \cdot 2\text{D}_2\text{O}$ . Starting from the best performing configurations corresponding to those illustrated in Fig. 11(a), introducing a mere  $f_{\text{O}} = 0.2\%$  raises  $\chi_{\text{red}}^2$  by 0.59 and 0.66 for the first and second columns, respectively. Likewise,  $\chi_{\text{red}}^2$  goes up by 0.06, 0.60, and 0.23 when starting from the configurations illustrated by the first, second, and third columns of Fig. 11(c), respectively. For  $\text{FeCl}_2 \cdot 2\text{D}_2\text{O}$ , the effect of delocalization onto oxygen is mixed. Starting from the configuration illustrated in the second column of Fig. 11(b), introducing  $f_{\text{O}} = 0.2\%$  raises  $\chi_{\text{red}}^2$  by 0.19. The value of  $\chi_{\text{red}}^2$  drops by 0.04 for the configuration corresponding to the first column, but when raised above  $f_{\text{O}} = 0.4\%$ , this meager improvement is already lost. The anti-bonding chlorine configuration,

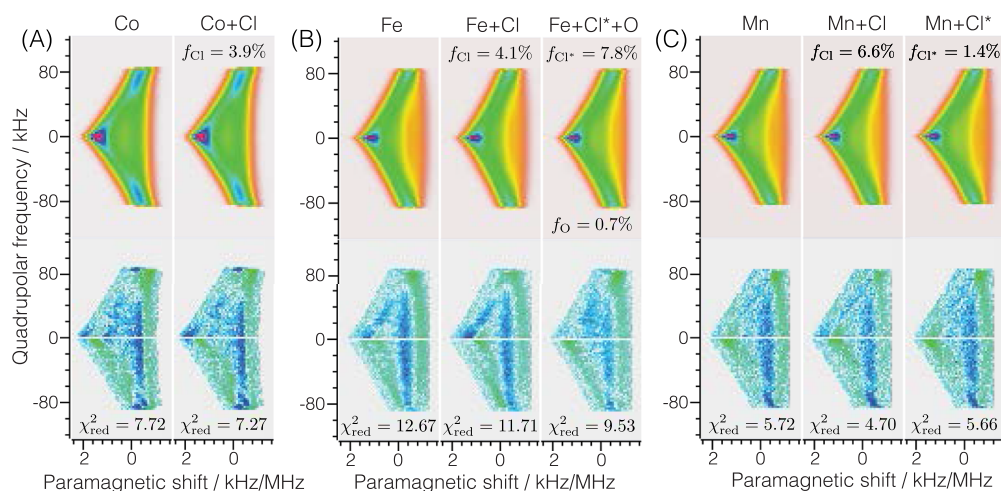


FIG. 11. Simulated correlation spectra and residual plots of (a)  $\text{CoCl}_2 \cdot 2\text{D}_2\text{O}$ , (b)  $\text{FeCl}_2 \cdot 2\text{D}_2\text{O}$ , and (c)  $\text{MnCl}_2 \cdot 2\text{D}_2\text{O}$  comparing different point dipole configurations. In (b), the last column is the  $\sigma^*$ -type antibonding chlorine model of Fig. 10(c) supplemented by oxygen sources; without the oxygen sources, the configuration of Fig. 10(c) gives  $\chi_{\text{red}}^2 = 10.28$  at  $f_{\text{Cl}^*} = 6.5\%$ . The quadrupolar parameters  $\langle C_q \rangle$  and  $\langle \eta_q \rangle$  were taken from the best fit of the experimental data. The line shape was refit to optimize the intensity, isotropic shift, and degree of line broadening for the paramagnetic shift dimension for each fixed set of calculated paramagnetic shift tensor parameters.



TABLE IV. Predicted instantaneous paramagnetic shift tensor parameters, corresponding to  $\mathbf{P}^D$  calculated using Eq. (12), for the comprehensive models deemed most reasonable in the main text. Euler angles correspond to rotation of the PAS into the lattice-fixed frame. The dihedral angle  $\phi_d$  was set to  $152.7^\circ$  for the Ni calculation.

Compound	Dipole locations	$f_{\text{Cl}}$ (%)	$f_{\text{O}}$ (%)	Site	Instantaneous $^2\text{H}$ shift tensor				
					$\zeta_P$ (ppm)	$\eta_P$	$\alpha_P$ (deg)	$\beta_P$ (deg)	$\gamma_P$ (deg)
$\text{CuCl}_2 \cdot 2\text{D}_2\text{O}$	$\text{Cu} + \text{Cl}_5^* + \text{O}$	14.7	2.1	1	259	0.145	43.9	61.3	111.8
				2	259	0.145	-43.9	61.3	-111.8
$\text{NiCl}_2 \cdot 2\text{D}_2\text{O}$	$\text{Ni} + \text{Cl}$	15.0	0	1	639	0.268	172.0	73.6	91.0
				2	683	0.040	138.5	108.1	78.1
				3	605	0.079	143.8	58.9	88.3
$\text{CoCl}_2 \cdot 2\text{D}_2\text{O}$	$\text{Co} + \text{Cl}$	3.9	0	1	1780	0.134	38.5	65.6	93.2
				2	1780	0.134	-38.5	65.6	-93.2
$\text{FeCl}_2 \cdot 2\text{D}_2\text{O}$	$\text{Fe} + \text{Cl}$	4.1	0	1	1762	0.313	121.4	61.6	95.5
				2	1762	0.313	-121.4	61.6	-95.5
$\text{MnCl}_2 \cdot 2\text{D}_2\text{O}$	$\text{Mn} + \text{Cl}$	6.6	0	1	1828	0.134	109.1	62.3	95.1
				2	1828	0.134	-109.1	62.3	-95.1

on the other hand, benefits significantly from delocalization onto oxygen, with  $\chi_{\text{red}}^2$  dropping from 10.28 to 9.53; the latter value and delocalization parameters are reported in the third column of Fig. 11(b). Despite these minor improvements occasionally found with further delocalization, we opt for consistency and conclude that the simpler point dipole configuration featuring nuclei-centered chlorine delocalization, shown in Fig. 10(b), provides the simplest and most reasonable approximation across the isostructural salts.

In Table IV, we list the paramagnetic shift tensor parameters calculated according to the source configuration of Fig. 10(b) at the optimal value of  $f_{\text{Cl}}$  for each case. The strength of the anisotropy for  $\text{CoCl}_2 \cdot 2\text{D}_2\text{O}$ ,  $\text{FeCl}_2 \cdot 2\text{D}_2\text{O}$ , and  $\text{MnCl}_2 \cdot 2\text{D}_2\text{O}$  in the absence of bisector flipping is predicted to be relatively constant, with the instantaneous  $\zeta_P$  varying no more than 40 ppm from 1800 ppm. This is remarkable in light of the Curie law, which might lead one to expect  $\zeta_P(\text{Co}) < \zeta_P(\text{Fe}) < \zeta_P(\text{Mn})$  roughly in proportion to  $S(S+1)$ , as visualized in Fig. 3. In Table V, we list the paramagnetic shift tensor parameters after the motional average. The predicted anisotropy remains roughly constant when accounting for bisector flipping, falling within the range  $1250 \pm 100$  ppm consistent with the experimental values. As a result of the motion, we predict that  $\text{CoCl}_2 \cdot 2\text{D}_2\text{O}$  overtakes  $\text{MnCl}_2 \cdot 2\text{D}_2\text{O}$

as the compound with the largest tensor anisotropy, with  $\langle \zeta_P \rangle(\text{Fe}) < \langle \zeta_P \rangle(\text{Mn}) < \langle \zeta_P \rangle(\text{Co})$ . This is the trend exhibited by our experimental results. These calculations also correctly predict that the asymmetry parameter  $\langle \eta_P \rangle$  is largest for  $\text{FeCl}_2 \cdot 2\text{D}_2\text{O}$  and capture the  $\langle \beta_{\text{rel}} \rangle = \langle \gamma_{\text{rel}} \rangle = \frac{\pi}{2}$  constraints implemented in the experimental tensor analysis.

The differences in  $\chi_{\text{red}}^2$  between the experimental best fit and the comprehensive model of the line shape remain large enough to warrant consideration of other factors which influence the calculation, especially for  $\text{FeCl}_2 \cdot 2\text{D}_2\text{O}$  and  $\text{MnCl}_2 \cdot 2\text{D}_2\text{O}$ . This disagreement is primarily driven by a persistent overestimation of  $\langle \eta_P \rangle$  by  $\sim 0.2$ – $0.4$  and an insubstantial reduction of this parameter by the delocalized point dipole models. One factor may be an overly constrained water ligand geometry and orientation, which also plays an important role in the shift tensor calculation. Shrinking the O–D bond length and opening the water angle does lower  $\langle \eta_P \rangle$  but requires rather extreme distortions of the water ligand to obtain good agreement with the experimental  $\langle \eta_P \rangle$ . In the “Mn+Cl” source model at  $f_{\text{Cl}} = 5\%$ , for example, reducing  $r_{\text{OD}}$  to  $0.8 \text{ \AA}$  and opening  $2\theta_w$  to  $120^\circ$  decrease  $\langle \eta_P \rangle$  to 0.29 but also leads to an unreasonable increase of  $\langle \zeta_P \rangle$  to 1768 ppm. Another factor could be the constraint on the dihedral angle. For  $\text{MnCl}_2 \cdot 2\text{D}_2\text{O}$ ,  $\langle \eta_P \rangle$  can be reduced by decreasing  $\phi_d$  alone. By simply subtracting

TABLE V. Predicted motional averaged paramagnetic shift tensor parameters, corresponding to the observable  $\langle \mathbf{P}^D \rangle$ , for the comprehensive models deemed most reasonable in the main text. The pseudo-contact shift is given by  $P_{\text{iso}}^D$ . Euler angles correspond to rotation of the PAS into the PAS of the efg tensor. The dihedral angle  $\phi_d$  was set to  $152.7^\circ$  for the Ni calculation.

Compound	$P_{\text{iso}}^D$ (ppm)	$\langle \zeta_P \rangle$ (ppm)	$\langle \eta_P \rangle$	$\langle \alpha_{\text{rel}} \rangle$ (deg)	$\langle \beta_{\text{rel}} \rangle$ (deg)	$\langle \gamma_{\text{rel}} \rangle$ (deg)
$\text{CuCl}_2 \cdot 2\text{D}_2\text{O}$	-12	-148	0.816	90	88.8	0
$\text{NiCl}_2 \cdot 2\text{D}_2\text{O}$	0	531	0.108	32.7	111.6	174.5
$\text{CoCl}_2 \cdot 2\text{D}_2\text{O}$	274	1320	0.392	164.4	90	90
$\text{FeCl}_2 \cdot 2\text{D}_2\text{O}$	-82	1150	0.705	136.9	90	90
$\text{MnCl}_2 \cdot 2\text{D}_2\text{O}$	0	1233	0.601	147.1	90	90



approximately  $\phi_d = 60^\circ$  to  $\phi_d = 150^\circ$ , becoming best when a moderate degree of delocalization to chlorine atoms, with  $f_{\text{Cl}} = 15\%$ , is made. Not all values of  $\phi_d$  within this range, however, are equally reasonable from a crystallographic standpoint. Selecting  $\phi_d = 60^\circ$ , for instance, leads to a crystal structure where the permanently occupied sites of water ligands on neighboring chains are separated by just 1.29 Å, creating instances of severe van der Waals overlap. This nearest neighbor separation does increase with increasing  $\phi_d$ , but only when  $\phi_d$  reaches the upper extreme of the agreement basin does the minimum separation of permanently occupied deuterium sites reach a physically tenable value of 2 Å near  $\phi_d = 150^\circ$ . For the water ligand geometry used in our calculation ( $r_{\text{OD}} = 0.98$  Å,  $2\theta_w = 103^\circ$ ), the value  $\phi_d = 152.7^\circ$  distinguishes itself as the orientation for which the O–D bond of the permanently occupied deuterium site is directed toward a chloride anion 2.60 Å away. In this configuration, the nearest neighbor separation of the permanently occupied deuterium sites is 2.02 Å. A similar situation occurs in  $\text{SnCl}_2 \cdot 2\text{H}_2\text{O}$ ,<sup>94</sup> where a hydrogen position of permanent occupancy is oriented toward a chloride anion.

Based on X-ray diffraction data, Morosin<sup>82</sup> speculated that the water ligand engages in weak bifurcated and trifurcated hydrogen bonds with its neighbors. It is interesting that he proposed hydrogen positions that nearly coincide with the two sites with 50% occupancy in the concerted motion of our pyramidal coordination model. Although Morosin did not mention ligand dynamics nor fractional occupancies, the simultaneous occupancy of these two positions would not be feasible due to van der Waals overlap of hydrogen atoms on neighboring ligands.

Of all the comprehensive model fits of iron group chloride dihydrates shifting- $d$  spectra, this particular model gives the lowest  $\chi_{\text{red}}^2$  values and are remarkably close to the fit in Fig. 2(b). The low uncertainty determined by our analysis of the experimental spectrum—refer to histograms of the marginal parameter distributions in the [supplementary material](#)—is a reflection of how sensitively the distinctiveness of the correlation pattern responds to changes of  $\langle\beta_P\rangle$ . Even more so than the other cases, this particular analysis nicely illustrates the power of the 2D NMR experiment and the comprehensive 2D line shape model as a method for determining the number, location, and occupancies of crystallographically distinct hydrogen sites.

## B. Other considerations

### 1. Contact anisotropy

Until this point in the discussion, we have completely neglected the contact contribution to the paramagnetic shift tensor,  $\mathbf{P}^C$ , under the assumption that the spin density at the deuteron is approximately zero. This is certainly a simplification in light of the fact that predicted pseudo-contact shifts  $P_{\text{iso}}^D$  disagree markedly with the observed isotropic shifts given in Table I. The anisotropic component of  $\mathbf{P}$  is, however, influenced by  $\mathbf{P}^C$  to a much lesser degree than the isotropic component, as  $\mathbf{P}^C$  is simply proportional to  $\chi^{(S)}$ , which itself is approximately proportional to  $\mathbf{g}$  (Appendix B). On this basis, we can estimate the anisotropy of  $\mathbf{P}^C$  to be

$$\zeta_{PC} \approx P_{\text{iso}}^C \frac{g_{zz} - g_{\text{iso}}}{g_{\text{iso}}},$$

where  $g_{\text{iso}} = \text{Tr}\{\mathbf{g}\}/3$ . This value can be taken as an estimate of the maximum extent to which the anisotropy of  $\mathbf{P}$  can be affected by the contact contribution. For  $\text{MnCl}_2 \cdot 2\text{D}_2\text{O}$  and  $\text{NiCl}_2 \cdot 2\text{D}_2\text{O}$ , where  $\chi^{(S)} = \chi$  is wholly isotropic, there is no contact contribution whatsoever to the anisotropy. To estimate this contribution for the other compounds, we first strip away an initial contribution to the measured isotropic shift using the predicted  $P_{\text{iso}}^D$ , leaving us with

$$\begin{aligned} P_{\text{iso}}^C(\text{Co}) &= -60 \text{ ppm}, \\ P_{\text{iso}}^C(\text{Fe}) &= 183 \text{ ppm}. \end{aligned}$$

For  $\text{FeCl}_2 \cdot 2\text{D}_2\text{O}$ , this leads to  $|\zeta_{PC}| = 14$  ppm. While we have not expressed a well-defined  $\mathbf{g}$  for  $\text{CoCl}_2 \cdot 2\text{D}_2\text{O}$ , crudely taking  $g_{zz} = 3$ ,  $g_{\text{iso}} = 2.5$  leads to the same magnitude of contact anisotropy. Since  $|\zeta_{PD}| > 1400$  ppm, we conclude that contact anisotropy affects our results below the 1% level of accuracy. This represents a range of error that is even smaller than the 95% confidence intervals given in Table I, justifying our neglect of contact anisotropy.

### 2. Bulk susceptibility effects

Macroscopic fields could also cause parameter bias. In a spherical Lorentz cavity large enough to render the distinction between continuous and discrete dipole densities negligible, the magnetic field at the nucleus can be written as

$$\mathbf{B} = \mathbf{B}_0 + \mathbf{B}_{\text{shape}} + \mathbf{B}_{\text{container}} + \mathbf{B}_{\text{dipolar}} + \mathbf{B}_{\text{micro}}. \quad (56)$$

Here, the molecular information of interest is encoded in the microscopic field represented by the final term,  $\mathbf{B}_{\text{micro}}$ , which corresponds to  $\mathbf{B}_P$  in Eqs. (9) and (11). The field  $\mathbf{B}_{\text{dipolar}}$  resulting from the dipolar fields due to the macroscopic magnetic moment of each crystallite primarily manifests as a broadening along the paramagnetic shift dimension as long as the crystallites are randomly oriented.<sup>95,96</sup> The value of  $\mathbf{B}_{\text{container}}$  arises from a discontinuity of the magnetization at the sample boundary and we take it to be negligible on account of the loose packing of crystallites in our sample. Demagnetizing fields resulting from nonspherical crystallites, as encoded by the field  $\mathbf{B}_{\text{shape}}$ , could in fact lead us to measure a systematic deviation from the predicted tensor anisotropy, as these fields are modulated by the orientation of the crystallite with respect to the external magnetic field. Therefore, they are also correlated with the paramagnetic shift anisotropy. The tendency of the compounds studied here is to crystallize in the form of long, thin needles, which could lead to substantial corrections. To counteract this effect, care was taken to grind the samples finely in an attempt to create approximately spherical crystallites, rendering the demagnetizing fields negligible.<sup>97</sup> Although the particle shape distribution is admittedly difficult to control, we do not believe that this explains the residual discrepancy in  $\langle\eta_P\rangle$  for the isostructural cases.

### 3. Electronic structure considerations

We might also concern ourselves with the accuracy of our molecular susceptibility calculations, which are reliant on simplistic (and arguably archaic) crystal field methods. We recall that, in spite of the multifarious crystal field developments implemented in calculating  $\chi$  for each ion—involving even *extrapolation*, in the case of  $\text{CoCl}_2 \cdot 2\text{D}_2\text{O}$ —the predictions which these susceptibilities underlie deviate in a *systematic* fashion from the values analyzed experimentally, to wit, the overestimation of  $\langle\eta_P\rangle$ . This suggests a structural origin to the discrepancy. There is little doubt that crystal field methods, calibrated and supported by information from other analytic methods, provide a sound way to determine accurate molecular susceptibility tensors. This robustness can prove useful when *g*- and *A*-tensor data from EPR, which usually provides the most straightforward means for calculating of paramagnetic shifts,<sup>9,38,98</sup> are difficult to obtain. Indeed, point dipole calculations in Lorentz cavities, calibrated solely by magnetization measurements, have been used since the 1960s to analyze the magnetic properties of materials—most noteworthy is the work by Albert Narath, also on the iron group chloride dihydrates.<sup>28,64</sup>

All factors considered, the slight discrepancy in  $\langle\eta_P\rangle$  for the isostructural series defies satisfactory explanation, and we leave this as a challenge for modern computational methods for paramagnetic shift tensor prediction. A general formalism, first introduced by Moon and Patchkovskii<sup>98</sup> expressing the NMR paramagnetic shift tensor in terms of the EPR *g*- and *A*-tensors, has recently been expanded in scope by Vaara, Soncini, and others<sup>99–101</sup> to encompass spin-orbit dequenched systems experiencing zero field splittings such as those we have studied here. Accurate prediction of the shifting-*d* spectra of the iron group chloride dihydrates, particularly  $\text{NiCl}_2 \cdot 2\text{D}_2\text{O}$ , might serve as a suitable challenge for modern computational methods in NMR crystallography.<sup>24,25,102–104</sup>

## V. SUMMARY

Two-dimensional NMR measurements have been performed on the  $\text{MCl}_2 \cdot 2\text{D}_2\text{O}$  family of compounds, with *M* = Cu, Ni, Co, Fe, and Mn, using the shifting-*d* echo experiment to correlate the  $^2\text{H}$  quadrupolar and paramagnetic shift interactions. The specific focus of this work is the design of a comprehensive NMR approach to determine the degree of positional and motional disorder of the hydrogen sites around oxygen in the water ligands of these hydrate salts, and, when possible, determine the number and location of crystallographically distinct hydrogen sites and their fractional occupancies.

The experimental 2D NMR spectra were analyzed for the principal components of the first-order quadrupole coupling and paramagnetic shift tensors along with their relative orientation. A chi-scaled Markov chain Monte Carlo method, aided by an efficient 2D frequency tenting algorithm, was used to explore the NMR parameter space and deliver estimations of the 95% confidence regions for the tensor parameters.

Starting from Van Vleck's generalized susceptibility equation, expressions for obtaining the molecular susceptibility tensor  $\chi$  for the iron group cations were determined

utilizing the concept of the orbital angular momentum dequenching tensor  $\Lambda$  in the context of crystal field theory. Aside from  $\text{Mn}^{2+}$ , the octahedrally coordinated cations of the divalent iron group in these complexes exhibit marked deviations from Curie law behavior.

On the basis of the experimental quadrupolar coupling parameters, a motional model with trigonal water ligand coordination and bisector flipping is proposed for the *M* = Cu, Co, Fe, and Mn salts. In the case of the Ni salt, we propose a model with pyramidal water ligand coordination and ligand hopping by 120° rotations about the Ni–O bond axis between two equally probable orientations in conjunction with bisector flipping.

Using the heavy atom crystal structure, appropriate motional models, and predicted susceptibility tensors, the performance of various point dipole source configurations for predicting the experimental 2D shifting-*d* echo NMR spectrum is evaluated. Given the approximations involved, the metal-only point dipole configuration for *M* = Ni, Co, Fe, and Mn salts performs well in its prediction of the experimental 2D spectra. This underscores the importance of an accurate determination of  $\chi$ . In all cases, further delocalization of point dipoles on the chlorine ligands gives moderate improvement. By contrast, the metal-only point dipole configuration performs poorly in predicting the  $\text{CuCl}_2 \cdot 2\text{D}_2\text{O}$  spectrum. Following previous work,<sup>27</sup> delocalization onto oxygen leads to an improved prediction.

Overall, we have shown that the shifting *d*-echo experiment and the analysis of its 2D spectrum can be a useful probe of structure and dynamics. This is particularly well illustrated in our determination of pyramidal water ligand coordination in  $\text{NiCl}_2 \cdot 2\text{D}_2\text{O}$ , as well as describing its restricted motion, and the absolute orientation of the permanently occupied deuterium site. An overestimation of  $\langle\eta_P\rangle$ , however, persists across our predictions for the *M* = Co, Fe, and Mn isostructural family. Given the precision of our measurements, such discrepancies lead us to challenge modern computational methods to accurately predict the instantaneous and motional averaged paramagnetic shift tensors, including principal component values and orientation, for these substances.

## SUPPLEMENTARY MATERIAL

See [supplementary material](#) for additional details on sample preparation, NMR acquisition parameters, the low temperature shifting-*d* echo spectrum of  $\text{NiCl}_2 \cdot 2\text{D}_2\text{O}$ , the crystal field energy level diagrams, a breakdown of the molecular susceptibility into its constituent parts according to the three terms of Eq. (18), survey of motional models for pyramidal coordination in  $\text{NiCl}_2 \cdot 2\text{D}_2\text{O}$ , an estimation of the effects of torsional motion, the marginal parameter distributions obtained in the analysis of all experimental shifting-*d* echo spectra, and an overview of structural parameters relevant to this study. Raw and processed NMR data are provided for each of the shifting-*d* echo experiments. We also provide the *Mathematica* .nb files used for the point dipole calculations and a .cif file including hydrogen coordinates and fractional occupancies according to our NMR refined structure of  $\text{NiCl}_2 \cdot 2\text{D}_2\text{O}$ .



## ACKNOWLEDGMENTS

This material is based upon work supported in part by the National Science Foundation under Grant No. CHE-1506870.

## APPENDIX A: DERIVATION OF THE DEQUENCHED MOLECULAR SUSCEPTIBILITY

Orbitally quenched magnetism occurs when the electrostatic Hamiltonian  $\hat{\mathcal{H}}_0$  contains no terms which couple the electron orbital and spin degrees of freedom. In this limit, we have  $[\hat{\mathcal{H}}_0, \hat{\mathbf{S}}^2] = [\hat{\mathcal{H}}_0, \hat{S}_z] = 0$  and label eigenstates of  $\hat{\mathcal{H}}_0$  as  $|\alpha m\rangle = |\alpha\rangle \otimes |m\rangle$ , where  $|\alpha\rangle$  and  $|m\rangle$  are the electronic state and magnetic quantum number of the total spin, respectively. We also assume that the ground electronic states  $|0m\rangle$  possess no orbital degeneracy<sup>51</sup> so that the first order contribution to the orbital moment vanishes,  $\langle 0|\hat{\mathbf{L}}|0\rangle = 0$ . Here, it is understood that  $\hat{\mathbf{L}}$  operates solely on the  $\alpha$  component of the eigenstates and so the  $|m\rangle$  component is omitted.

As described,  $\hat{\mathcal{H}}_0$  is a good zeroth-order description for the electronic configuration of the iron group elements, and so we adopt the complete unperturbed eigenstates  $|\alpha m\rangle$  as the working basis. Dequenching occurs when a spin-orbit coupling is introduced as a perturbation to  $\hat{\mathcal{H}}_0$ . When the  $LS$ -coupling scheme holds, we take

$$\hat{\mathcal{H}}_1 = \frac{\lambda_{\text{so}}}{\hbar^2} \hat{\mathbf{L}} \cdot \hat{\mathbf{S}}, \quad (\text{A1})$$

and, following Griffith,<sup>53</sup> the first order correction  $|\psi^{(1)}m\rangle$  to the relevant set of ground state wave functions  $|\psi m\rangle = |0m\rangle + |\psi^{(1)}m\rangle$  can be written in the following way:

$$|\psi^{(1)}m\rangle = \frac{\lambda_{\text{so}}}{\hbar^2} \sum_{\alpha>0} \frac{\langle \alpha|\hat{\mathbf{L}}|0\rangle}{E_0 - E_\alpha} \cdot \hat{\mathbf{S}}|\alpha m\rangle. \quad (\text{A2})$$

Equation (A2) expresses the perturbed wave functions in terms of matrix elements of  $\hat{\mathbf{L}}$  connecting electronic states, which

are just numbers, but overtly retains the action of  $\hat{\mathbf{S}}$  on the spin space kets. In this way, it serves as the foundation for defining equivalent operators for  $\hat{\mathcal{H}}_1$  and  $\hat{\boldsymbol{\mu}}$  which act only on the truncated subspace of ground electronic state spin kets. For instance, the second order correction to the energy,  $E_m^{(2)} = \langle 0m|\hat{\mathcal{H}}_1|\psi^{(1)}m\rangle$ , is given by

$$E_m^{(2)} = \frac{\lambda_{\text{so}}^2}{\hbar^4} \sum_i \sum_j \sum_{\alpha>0} \langle m|\hat{S}_i \frac{\langle 0|\hat{L}_i|\alpha\rangle \langle \alpha|\hat{L}_j|0\rangle}{E_0 - E_\alpha} \hat{S}_j|m\rangle. \quad (\text{A3})$$

By introducing the symmetric negative semi-definite orbital angular momentum dequenching tensor  $\boldsymbol{\Lambda}$ , with components<sup>47,53,54</sup>

$$\Lambda_{ij} = \frac{1}{\hbar^2} \sum_{\alpha>0} \frac{\langle 0|\hat{L}_i|\alpha\rangle \langle \alpha|\hat{L}_j|0\rangle}{E_0 - E_\alpha}, \quad (\text{A4})$$

Eq. (A3) becomes equivalent to

$$E_m^{(2)} = \langle m|\hat{\mathbf{S}} \cdot (\lambda_{\text{so}}^2 \boldsymbol{\Lambda} / \hbar^2) \cdot \hat{\mathbf{S}}|m\rangle \quad (\text{A5})$$

from which we derive the form of the “zero-field splitting” Hamiltonian in the truncated subspace,

$$\mathcal{H}_{\text{ZFS}} = \frac{1}{\hbar^2} \hat{\mathbf{S}} \cdot \mathbf{D}_\lambda \cdot \hat{\mathbf{S}}, \quad (\text{A6})$$

where the zero-field splitting tensor  $\mathbf{D}_\lambda = \lambda_{\text{so}}^2 \boldsymbol{\Lambda}$  has units of energy.

We develop expressions related to magnetism using the ground state wave functions, corrected by perturbation theory. The matrix elements of the electronic magnetic moment operator  $\hat{\boldsymbol{\mu}} = -\mu_B (\hat{\mathbf{L}} + g_e \hat{\mathbf{S}}) / \hbar$ , within degenerate zeroth-order spin states of the ground electronic manifold, are given by  $\langle \psi m|\hat{\boldsymbol{\mu}}|\psi m'\rangle$ , which can be decomposed into

$$\begin{aligned} \langle \psi m|\hat{\boldsymbol{\mu}}_i|\psi m'\rangle &= -\frac{\mu_B}{\hbar} \left( \langle 0|\hat{L}_i|0\rangle \langle m|m'\rangle + g_e \langle 0|0\rangle \langle m|\hat{S}_i|m'\rangle \right) \\ &\quad - \frac{\mu_B \lambda_{\text{so}}}{\hbar^3} \left( \sum_{\alpha>0} \sum_k \frac{\langle 0|\hat{L}_i|\alpha\rangle \langle \alpha|\hat{L}_k|0\rangle}{E_0 - E_\alpha} \langle m|\hat{S}_k|m'\rangle + g_e \sum_{\alpha>0} \langle 0|\alpha\rangle \sum_k \frac{\langle \alpha|\hat{L}_k|0\rangle}{E_0 - E_\alpha} \langle m|\hat{S}_k|m'\rangle \right) \\ &\quad - \frac{\mu_B \lambda_{\text{so}}}{\hbar^3} \left( \sum_{\alpha>0} \sum_k \frac{\langle 0|\hat{L}_k|\alpha\rangle \langle \alpha|\hat{L}_i|0\rangle}{E_0 - E_\alpha} \langle m|\hat{S}_k|m'\rangle + g_e \sum_{\alpha>0} \langle \alpha|0\rangle \sum_k \frac{\langle 0|\hat{L}_k|\alpha\rangle}{E_0 - E_\alpha} \langle m|\hat{S}_k|m'\rangle \right) \\ &\quad - \frac{\mu_B}{\hbar} \langle \psi^{(1)}m|\hat{L}_i + g_e \hat{S}_i|\psi^{(1)}m\rangle. \end{aligned}$$

The final term, between the correction states  $|\psi^{(1)}m\rangle$ , is of order  $(E_0 - E_\alpha)^{-2}$  and can be neglected under the assumption that  $|\lambda_{\text{so}}| \ll E_\alpha - E_0$ ; that is, the spin-orbit coupling is a weak perturbation onto the electrostatic Hamiltonian. Among the terms of order  $(E_0 - E_\alpha)^{-1}$ , those which involve  $g_e$  are zero by the orthonormality of the electronic eigenstates. Finally, with our assumed condition that the first order contribution to the orbital angular momentum is quenched,  $\langle 0|\hat{\mathbf{L}}|0\rangle = 0$ , we are

left with

$$\langle \psi m|\hat{\boldsymbol{\mu}}_i|\psi m'\rangle = \langle m| -\frac{\mu_B}{\hbar} \sum_k g_{ik} \hat{S}_k |m'\rangle, \quad (\text{A7})$$

where the symmetric  $g$ -tensor components,  $g_{ik}$ , are given by Eq. (20). This has the form of an effective magnetic moment operator

$$\hat{\boldsymbol{\mu}}_{\text{eff}} = -\frac{\mu_B}{\hbar} \mathbf{g} \cdot \hat{\mathbf{S}}, \quad (\text{A8})$$

which, unlike the formal electron magnetic moment operator, is defined to act only on the spin degrees of freedom within the ground electronic manifold.

We also consider matrix elements of  $\hat{\mu}$  connecting the ground and excited electronic states, corrected by perturbation theory. Including the perturbation correction only for the ground state, we find

$$\langle \psi m | \hat{\mu}_i | \alpha'' m'' \rangle = -\frac{\mu_B}{\hbar} \left( \langle 0 | \hat{L}_i | \alpha'' \rangle \langle m | m'' \rangle + g_e \sum_{\alpha > 0} \langle \alpha | \alpha'' \rangle \sum_k \frac{\langle 0 | \hat{L}_k | \alpha \rangle}{E_0 - E_\alpha} \langle m | \hat{S}_k | m'' \rangle \right).$$

As we will see below, the second term would introduce terms of order  $(E_0 - E_\alpha)^{-2}$  into our expressions for the molecular susceptibility. Similarly, a perturbative correction to the excited state  $|\alpha'' m''\rangle$  would introduce terms of order  $(E_0 - E_\alpha)^{-2}$  and  $(E_0 - E_\alpha)^{-3}$ . They are therefore neglected, and for our purposes, we take

$$\langle \psi m | \hat{\mu}_i | \alpha'' m'' \rangle = \langle m | -\frac{\mu_B}{\hbar} \langle 0 | \hat{L}_i | \alpha'' \rangle | m'' \rangle. \quad (\text{A9})$$

The generalized Van Vleck susceptibility equation, Eq. (14), can be simplified by using Eqs. (A7) and (A9) to express the magnetic moment matrix elements with respect to the *unperturbed* basis states. This is done through their substitution into the magnetic dipole moment matrix elements contained in the  $W$  factors of Eqs. (15) and (16). The  $W_{m,ij}^I$  term is thus formed as the summation over the  $(2S + 1)$ -dimensional spin subspace of the ground electronic state, referred to as the magnetically active manifold. Upon inclusion of the perturbative corrections,

$$W_{m,ij}^I = \sum_{m'} \langle \psi m | \hat{\mu}_i | \psi m' \rangle \langle \psi m' | \hat{\mu}_j | \psi m \rangle = \frac{\mu_B^2}{\hbar^2} \sum_k \sum_l g_{ik} g_{jl} \langle m | \hat{S}_k \hat{S}_l | m \rangle, \quad (\text{A10})$$

with the completeness relation  $\sum_{m'} |m'\rangle \langle m'| = \hat{1}$  in the truncated spin manifold. For the  $W_{m,ij}^{II}$  term, which is to be summed across the manifolds of the electronic excited states,

$$\begin{aligned} W_{m,ij}^{II} &= \sum_{\alpha''} \sum_{m''} \frac{\langle \psi m | \hat{\mu}_i | \alpha'' m'' \rangle \langle \alpha'' m'' | \hat{\mu}_j | \psi m \rangle + \langle \psi m | \hat{\mu}_j | \alpha'' m'' \rangle \langle \alpha'' m'' | \hat{\mu}_i | \psi m \rangle}{E_0 - E_{\alpha''}} \\ &= \frac{\mu_B^2}{\hbar^2} \langle m | m \rangle \sum_{\alpha''} \frac{\langle 0 | \hat{L}_i | \alpha'' \rangle \langle \alpha'' | \hat{L}_j | 0 \rangle + \langle 0 | \hat{L}_j | \alpha'' \rangle \langle \alpha'' | \hat{L}_i | 0 \rangle}{E_0 - E_{\alpha''}} \\ &= 2\mu_B^2 \Lambda_{ij}, \end{aligned} \quad (\text{A11})$$

which is in fact independent of  $m$ . The factor of  $(E_0 - E_{\alpha''})^{-1}$  already present explains the validity of discarding terms of order higher than  $(E_0 - E_\alpha)^0$  in Eq. (A9).

The generalized Van Vleck equation is formed as the sum over thermally accessible states, which in using Eqs. (A10) and (A11) to calculate the  $W$  factors, we are implicitly assuming is restricted to magnetically active manifold. Then, with the zero-field energies given by Eq. (A5), we can express the components of the molecular susceptibility as a sum over the  $(2S + 1)$  unperturbed spin states,

$$\begin{aligned} \chi_{ij} &= \frac{\mu_0 \mu_B^2}{\hbar^2} \frac{\sum_{m=-S}^S \sum_k \sum_l g_{ik} g_{jl} \langle m | \hat{S}_k \hat{S}_l | m \rangle e^{-E_m^{(2)}/(k_B T)}}{k_B T \sum_{m=-S}^S e^{-E_m^{(2)}/(k_B T)}} \\ &\quad - 2\mu_0 \mu_B^2 \Lambda_{ij}. \end{aligned} \quad (\text{A12})$$

This second term, arising from the  $W_{m,ij}^{II}$  factors, reveals the temperature independent paramagnetism. The first term contains the thermal (Boltzmann) average of  $\hat{S}_k \hat{S}_l$ . This quantity yields a convenient expression in the high temperature approximation  $E_m^{(2)} \ll k_B T$  provided that the zero of energy is shifted to the center of gravity of the ground state manifold. The latter condition implies that the trace is stripped from the zero field splitting tensor,  $\mathbf{D} = \mathbf{D}_\lambda - \frac{1}{3} \text{Tr}(\mathbf{D}_\lambda) \mathbf{1}$ , so that the condition  $\sum_m E_m^{(2)} = 0$  is fulfilled. Then the thermal average of  $\hat{S}_k \hat{S}_l$  is

$$\begin{aligned} &\frac{\sum_{m=-S}^S \langle m | \hat{S}_k \hat{S}_l | m \rangle e^{-E_m^{(2)}/(k_B T)}}{\sum_{m=-S}^S e^{-E_m^{(2)}/(k_B T)}} \\ &= \frac{1}{2S + 1} \sum_{m=-S}^S \langle m | \hat{S}_k \hat{S}_l | m \rangle \left( 1 - \frac{1}{k_B T} \langle m | \hat{\mathbf{S}} \cdot \mathbf{D} \cdot \hat{\mathbf{S}} | m \rangle \right) \\ &= \frac{1}{2S + 1} \left[ \text{Tr}\{\hat{S}_k \hat{S}_l\} - \frac{1}{k_B T} \sum_o \sum_p D_{op} \text{Tr}\{\hat{S}_k \hat{S}_l \hat{S}_o \hat{S}_p\} \right]. \end{aligned} \quad (\text{A13})$$

Inserting this into Eq. (A12) yields the formula of Eq. (18) as the molecular susceptibility for spin-orbit perturbed  $LS$ -ion systems, after using established formulas to evaluate the traces.<sup>36</sup> Note that for these systems,  $\mathbf{\Lambda}$  represents the fundamental quantity:  $\mathbf{g}$  and  $\mathbf{D}$  are calculated from  $\mathbf{\Lambda}$  by Eqs. (20) and (21) and will be diagonal in the principal axis system of  $\mathbf{\Lambda}$ . Given their spectroscopic interpretation, however, they are convenient to retain in Eq. (18).

Therefore, spin-orbit dequenched magnetism requires that, on top of an orbitally nondegenerate ground state, we have  $|\lambda_{so}| \ll E_1 - E_0$  (unless  $\langle 1 | \hat{\mathbf{L}} | 0 \rangle = 0$ , which then requires  $|\lambda_{so}| \ll E_2 - E_0$ , as in the case of  $\text{CuCl}_2 \cdot 2\text{H}_2\text{O}$ ), and that the populated states are restricted to the ground spin multiplet which can be treated in the high temperature approximation,  $E_m^{(2)} \ll k_B T$ . The  $T^{-2}$  term of Eq. (18) was first expressed in

terms of the  $D$ -tensor by Bleaney in the context of the crystal field induced zero field splitting of lanthanide ions,<sup>55</sup> and when Eq. (18) is applied to the calculation of paramagnetic shifts, it is subsumed by the theory of Kurland and McGarvey.<sup>105</sup> Finally, we note that a recent monograph by Pell *et al.*<sup>106</sup> also gives an expression for the molecular susceptibility that is nearly identical to Eq. (18), except that the temperature independent paramagnetism term is missing. Its absence appears to be the result of neglecting the second-order orbital Zeeman Hamiltonian. In this work, however, we find that the temperature independent paramagnetism term should not be neglected, as Table S-V shows that its contribution to  $\chi_{zz}$  in  $\text{FeCl}_2 \cdot 2\text{D}_2\text{O}$  at 300 K exceeds 6%, and is comparable to the  $T^{-2}$  term for all components at this temperature. As already noted, this term arises from a contribution which is independent of the electronic spin state  $m$ , as seen in Eq. (A11). As such, each level of the magnetically active manifold is raised uniformly and the temperature independent contribution is not observable in EPR. This may explain why temperature independent paramagnetism has largely been overlooked in the magnetic resonance literature.

## APPENDIX B: SPIN MOLECULAR SUSCEPTIBILITY

The contact term in Eq. (9) requires evaluating the thermal average of the electronic magnetic moment due to spin, represented by the operator  $\hat{\mu}_S$ ,

$$\hat{\mu}_S = -\frac{\mu_B g_e}{\hbar} \hat{S}, \quad (\text{B1})$$

in order to determine  $\mathbf{m}_S$ . This is not as simple as transcribing components according to  $\hat{\mu} \rightarrow \hat{\mu}_S$  in the  $W$  factors of Eqs. (15) and (16), for the orbital component of  $\mu$  still influences the Zeeman level structure of the magnetically active manifold. Nonetheless, the derivation of the generalized Van Vleck equation lends itself to straightforward modification, allowing us to determine a *spin molecular susceptibility*  $\chi^{(S)}$ , for which  $\mu_0 \mathbf{m}_S = \chi^{(S)} \cdot \mathbf{B}_0$ .

The modification involves the power series expansion giving the energy of the paramagnetic complex in the presence of the applied field,

$$E_m = E_m^{(0)} + \sum_i \langle m | \hat{\mu}_i | m \rangle B_i + \sum_i \sum_j \sum_n \frac{\langle m | \hat{\mu}_i | n \rangle \langle n | \hat{\mu}_j | m \rangle B_i B_j}{E_m - E_n}. \quad (\text{B2})$$

The indices  $i, j$  refer to Cartesian field axes. This is the expression for the energy given by the full electronic Hamiltonian (including spin-orbit coupling) with the addition of the electronic Zeeman energy

$$\hat{H} = \hat{H}_e - \frac{\mu_B}{\hbar} (\hat{\mathbf{L}} + g_e \hat{\mathbf{S}}) \cdot \mathbf{B}. \quad (\text{B3})$$

The expected value of the induced electronic magnetic moment of the (zero field) eigenstate  $m$  directed along the Cartesian field direction  $i$  is given by

$$\langle \mu_i \rangle_m = -\frac{\partial E_m}{\partial B_i}, \quad (\text{B4})$$

analogous to its definition in thermodynamics. Determination of the thermal average of this expected value according

to Boltzmann statistics for the other Cartesian field directions followed by generalization for arbitrary field directions leads to the full form of Eq. (14), the generalized Van Vleck equation.<sup>52</sup>

Equation (B4) also follows from Eqs. (B2) and (B3) by the Feynman-Hellmann theorem.<sup>107</sup> From Eqs. (B2) and (B3), this theorem also gives the expectation value of the electronic magnetic moment due to spin in the state  $m$ ,

$$\langle \mu_{S,i} \rangle_m = -\frac{g_e}{B_i} \frac{\partial E_m}{\partial g_e}. \quad (\text{B5})$$

The derivation of the Van Vleck equation analog for  $\chi^{(S)}$  proceeds with the calculation of the Boltzmann average of  $\langle \mu_{S,i} \rangle_m$  as defined in Eq. (B5), followed by generalization for the arbitrary field direction as for the ordinary generalized Van Vleck equation.<sup>52</sup> This leads to an equation identical in form to Eq. (14) but which involves the hybrid  $W$  factors,

$$W_{m,ij}^{(S),I} = \sum_{n'} \langle m | \hat{\mu}_{S,i} | n' \rangle \langle n' | \hat{\mu}_j | m \rangle, \quad (\text{B6})$$

$$W_{m,ij}^{(S),II} = \sum_{n''} \frac{\langle m | \hat{\mu}_{S,i} | n'' \rangle \langle n'' | \hat{\mu}_j | m \rangle + \langle m | \hat{\mu}_{S,j} | n'' \rangle \langle n'' | \hat{\mu}_i | m \rangle}{E_m - E_{n''}}. \quad (\text{B7})$$

For the spin-orbit dequenched system defined by the applicability of Eq. (18), it is straightforward to mirror the derivation in Appendix A using the hybrid  $W$  factors to arrive at a similarly concise expression for the spin molecular susceptibility,

$$\chi^{(S)} = \frac{\mu_0 \mu_B^2 g_e S(S+1)}{3k_B T} \left[ \mathbf{g} - \frac{(2S+3)(2S-1)}{10k_B T} \mathbf{g} \cdot \mathbf{D} \right]. \quad (\text{B8})$$

As with Eq. (18), this expression can be worked out from the Kurland and McGarvey theory of paramagnetic shifts,<sup>105</sup> although our approach using the Feynman-Hellmann theorem is closer to that of Narath<sup>28</sup> in his calculation of the (total) molecular susceptibility of  $\text{CoCl}_2 \cdot 2\text{D}_2\text{O}$ . Interestingly,  $W_{m,ij}^{(S),II}$  vanishes for these systems to this order in perturbation theory, implying that the temperature independent component of the contact shift is negligible.

## APPENDIX C: SINGLE SITE AFTER MOTIONAL AVERAGE

Consider two ligand sites  $\text{O}_1$  and  $\text{O}'_1$ , where the heavy atom positions with respect to  $\text{O}'_1$  are known to be related to  $\text{O}_1$  by some symmetry operation of the lattice. Since  $\text{O}_1$  and  $\text{O}'_1$  lead to the same correlation spectrum, it follows that the corresponding tensors,  $\langle \mathbf{R}^{\{\xi\}} \rangle$  and  $\langle \mathbf{R}'^{\{\xi\}} \rangle$ , are isometric; i.e. their eigenvalues are identical such that

$$\langle \mathbf{R}'^{\{\xi\}} \rangle = \mathcal{O} \langle \mathbf{R}^{\{\xi\}} \rangle \mathcal{O}^{-1}, \quad (\text{C1})$$

where

$$\langle \mathbf{R}'^{\{\xi\}} \rangle = \sum_{j=1}^N p_j' \mathbf{R}_j'^{\{\xi\}} \quad (\text{C2})$$

and  $\mathcal{O}$  is some orthogonal transformation. This strict relationship is ensured if, for each  $j$  corresponding to one of the  $N$  deuteron sites,

$$\mathbf{R}_j'^{\{\xi\}} = \mathcal{O} \mathbf{R}_j^{\{\xi\}} \mathcal{O}^{-1}, \quad (\text{C3})$$

along with the crucial correspondence

$$p_j = p'_j. \quad (\text{C4})$$

To determine the nature of the orthogonal transformation  $\mathcal{O}$ , we turn to the paramagnetic shift tensor. We have for each  $j$ ,

$$\mathbf{R}_j^{(P)} = \mathcal{O} \mathbf{R}_j^{(P)} \mathcal{O}^{-1}, \quad (\text{C5})$$

which by Eq. (12) permits us to establish the correspondence,

$$\mathbf{r}'_{j,k} = \mathcal{O} \mathbf{r}_{j,k}, \quad \forall j, k. \quad (\text{C6})$$

We now exploit the heavy atom lattice symmetry to select the origin of our coordinate system to be the fixed point of the lattice symmetry operation  $\mathcal{P}$  relating  $\mathbf{O}_1$  to  $\mathbf{O}'_1$  such that

$$\mathbf{r}'_k = \mathcal{P} \mathbf{r}_k, \quad \forall k, \quad (\text{C7})$$

where  $\mathbf{r}_k$  gives the  $k$ th lattice coordinate (principally, those of the paramagnetic transition metal atoms) for  $\mathbf{O}_1$  and  $\mathbf{r}'_k$  those for  $\mathbf{O}'_1$ . This choice of origin also ensures that  $\mathcal{P}$  can be represented by an orthogonal transformation. With respect to this same origin, we write  $\mathbf{r}_j$  and  $\mathbf{r}'_j$  for the coordinates of the  $j$ th deuteron site for  $\mathbf{O}_1$  and  $\mathbf{O}'_1$ , respectively. Then Eqs. (C6) and (C7) imply that

$$\begin{aligned} (\mathbf{r}'_k - \mathbf{r}'_j) &= \mathcal{O}(\mathbf{r}_k - \mathbf{r}_j), \\ \mathbf{r}'_j &= \mathcal{O} \mathbf{r}_j + (\mathcal{P} - \mathcal{O}) \mathbf{r}_k, \quad \forall j, k. \end{aligned} \quad (\text{C8})$$

But  $\mathbf{r}'_j$  cannot possibly express such a dependence on  $k$ . The final term in Eq. (C8) must vanish, forcing us to identify  $\mathcal{O} = \mathcal{P}$ . Crucially,

$$\mathbf{r}'_j = \mathcal{P} \mathbf{r}_j, \quad \forall j. \quad (\text{C9})$$

Therefore, barring accidental equivalence, we can assert that when the correlation spectrum appears as though originating from a single site, *deuteron sites can be propagated from  $\mathbf{O}_1$  to all other sites in accordance with the overall heavy atom lattice symmetry*. Furthermore, because we have already established  $p_j = p'_j$ , we can assign  $p$  factors to symmetry related sites for the motional average cases we consider.

<sup>1</sup>C. P. Slichter, *Principles of Magnetic Resonance* (Springer-Verlag, Berlin, 1980).

<sup>2</sup>A. Abragam, *Principles of Nuclear Magnetism* (Oxford University Press, Oxford, 1961).

<sup>3</sup>I. Bertini, C. Luchinat, G. Parigi, and E. Ravera, *NMR of Paramagnetic Molecules*, 2nd ed. (Elsevier, Boston, 2017).

<sup>4</sup>G. N. La Mar, W. D. Horrocks, and R. H. Holm, *NMR of Paramagnetic Molecules: Principles and Applications* (Elsevier, 1973).

<sup>5</sup>D. Eaton, A. Josey, W. Phillips, and R. Benson, *J. Chem. Phys.* **37**, 347–360 (1962).

<sup>6</sup>L. B. Dugad, G. N. La Mar, L. Banci, and I. Bertini, *Biochemistry* **29**, 2263–2271 (1990).

<sup>7</sup>P. Caravan, J. J. Ellison, T. J. McMurry, and R. B. Lauffer, *Chem. Rev.* **99**, 2293–2352 (1999).

<sup>8</sup>G. Otting, “Protein NMR using paramagnetic ions,” in *Annual Review of Biophysics*, edited by D. C. Rees, K. A. Dill, and J. R. Williamson (Annual Reviews, Palo Alto, 2010), Vol. 39, p. 387–405.

<sup>9</sup>N. Bloembergen, *Physica* **16**, 95 (1950).

<sup>10</sup>R. G. Shulman and V. Jaccarino, *Phys. Rev.* **108**, 1219–1231 (1957).

<sup>11</sup>J. M. Mays, *Phys. Rev.* **108**, 1090–1091 (1957).

<sup>12</sup>G. Soda and T. Chiba, *J. Chem. Phys.* **50**, 439–455 (1969).

<sup>13</sup>W. Looyestijn, T. Klaassen, and N. Poulis, *Physica B+C* **97**, 33 (1979).

<sup>14</sup>M. Kozelj, V. Rutar, I. Zupancic, R. Blinc, H. Arend, R. Kind, and G. Chapuis, *J. Chem. Phys.* **74**, 4123–4129 (1981).

<sup>15</sup>S. E. Woehler, R. J. Wittebort, S. M. Oh, D. N. Hendrickson, D. Inniss, and C. E. Strouse, *J. Am. Chem. Soc.* **108**, 2938 (1986).

<sup>16</sup>V. P. Chacko, S. Ganapathy, and R. G. Bryant, *J. Am. Chem. Soc.* **105**, 5491–5492 (1983).

<sup>17</sup>J. F. Haw and G. C. Campbell, *J. Magn. Reson.* **66**, 558 (1986).

<sup>18</sup>A. K. Cheetham, C. M. Dobson, C. P. Grey, and R. J. B. Jakeman, *Nature* **328**, 706 (1987).

<sup>19</sup>Y. Ishii, N. P. Wickramasinghe, and S. Chimon, *J. Am. Chem. Soc.* **125**, 3438 (2003).

<sup>20</sup>I. Bertini, C. Luchinat, G. Parigi, and R. Pierattelli, *ChemBioChem* **6**, 1536 (2005).

<sup>21</sup>N. P. Wickramasinghe, M. Shaibat, and Y. Ishii, *J. Am. Chem. Soc.* **127**, 5796 (2005).

<sup>22</sup>S. Parthasarathy, Y. Nishiyama, and Y. Ishii, *Acc. Chem. Res.* **46**, 2127 (2013).

<sup>23</sup>C. P. Jaroniec, *J. Magn. Reson.* **253**, 50–59 (2015).

<sup>24</sup>G. Kervern, A. D’Aléo, L. Toupet, O. Maury, L. Emsley, and G. Pintacuda, *Angew. Chem., Int. Ed.* **48**, 3082 (2009).

<sup>25</sup>C. Luchinat, G. Parigi, E. Ravera, and M. Rinaldelli, *J. Am. Chem. Soc.* **134**, 5006 (2012).

<sup>26</sup>G. Pintacuda and G. Kervern, *Paramagnetic Solid-State Magic-Angle Spinning NMR Spectroscopy*, edited by H. Heise and S. Matthews, Topics in Current Chemistry (Springer Berlin Heidelberg, Berlin, Heidelberg, 2013), Vol. 335, pp. 157–200.

<sup>27</sup>A. Nayeem and J. P. Yesinowski, *J. Chem. Phys.* **89**, 4600 (1988).

<sup>28</sup>A. Narath, *Phys. Rev.* **140**, A552 (1965).

<sup>29</sup>B. J. Walder, K. K. Dey, M. C. Davis, J. H. Baltisberger, and P. J. Grandinetti, *J. Chem. Phys.* **142**, 014201 (2015).

<sup>30</sup>T. A. Early, *J. Magn. Reson.* **74**, 337 (1987).

<sup>31</sup>M. Mizuno, N. Itakura, and K. Endo, *Chem. Phys. Lett.* **416**, 358 (2005).

<sup>32</sup>F. H. Larsen, *Solid State Nucl. Mag.* **31**, 100 (2007).

<sup>33</sup>M. Linder, A. Höhener, and R. R. Ernst, *J. Chem. Phys.* **73**, 4959 (1980).

<sup>34</sup>R. E. Rundle, *J. Am. Chem. Soc.* **79**, 3372 (1957).

<sup>35</sup>P. J. Grandinetti, J. T. Ash, and N. M. Trease, *Prog. Nucl. Magn. Reson. Spectrosc.* **59**, 121 (2011).

<sup>36</sup>D. A. Varshalovich, A. N. Moskalev, and V. K. Khersonskii, *Quantum Theory of Angular Momentum* (World Scientific, Teaneck, NJ, 1988).

<sup>37</sup>R. K. Harris, E. D. Becker, S. M. C. De Menezes, P. Grangerd, R. E. Hoffman, and K. W. Zilm, *Solid State Nucl. Magn. Reson.* **33**(3), 41 (2008).

<sup>38</sup>H. M. McConnell and R. E. Robertson, *J. Chem. Phys.* **29**, 1361 (1958).

<sup>39</sup>I. Bertini, C. Luchinat, and G. Parigi, *Prog. Nucl. Magn. Reson. Spectrosc.* **40**, 249 (2002).

<sup>40</sup>PhySy Ltd, RMN, Version 1.8 ([www.physyapps.com](http://www.physyapps.com), PhySy Ltd., Grandview Heights, OH 43212).

<sup>41</sup>H. S. Gutowsky and G. E. Pake, *J. Chem. Phys.* **18**, 162 (1950).

<sup>42</sup>K. Larsson, J. Tegenfeldt, and K. Hermansson, *J. Chem. Soc., Faraday Trans.* **87**, 1193 (1991).

<sup>43</sup>*Handbook of Markov Chain Monte Carlo*, Chapman & Hall/CRC Handbooks of Modern Statistical Methods, edited by S. Brooks, A. Gelman, G. Jones, and X.-L. Meng (Chapman and Hall/CRC, Boca Raton, FL, USA, 2011), p. 619.

<sup>44</sup>D. W. Alderman, M. S. Solum, and D. M. Grant, *J. Chem. Phys.* **84**, 3717 (1986).

<sup>45</sup>T. Charpentier, C. Fermon, and J. Virlet, *J. Chem. Phys.* **109**, 3116 (1998).

<sup>46</sup>D. E. Budil, S. Lee, S. Saxena, and J. H. Freed, *J. Magn. Reson., Ser. A* **120**, 155–189 (1996).

<sup>47</sup>B. Bleaney and A. Abragam, *Electron Paramagnetic Resonance of Transition Ions* (Oxford University Press, Oxford, 1970).

<sup>48</sup>D. J. Griffiths, *Am. J. Phys.* **50**, 698 (1982).

<sup>49</sup>E. Ruiz, J. Cirera, and S. Alvarez, *Coord. Chem. Rev.* **249**, 2649–2660 (2005).

<sup>50</sup>Wolfram Research, Inc., *Mathematica*, Version 10.0 (Wolfram Research, Inc., Champaign, IL, 2014).

<sup>51</sup>J. H. V. Vleck, *The Theory of Electric and Magnetic Susceptibilities* (Oxford University Press, 1932).

<sup>52</sup>M. Gerloch, *Magnetism and Ligand-Field Analysis* (Cambridge University Press, 1983).

<sup>53</sup>J. Griffith, *The Theory of Transition-Metal Ions* (Cambridge University Press, 1971).

<sup>54</sup>D. Mingos and R. Boca, *Magnetic Functions beyond the Spin-Hamiltonian* (Springer, 2006), Vol. 117.

<sup>55</sup>B. Bleaney, *J. Magn. Reson.* **8**, 91–100 (1972).

<sup>56</sup>B. R. McGarvey, *Inorg. Chem.* **34**, 6000–6007 (1995).



- <sup>57</sup>G. A. Bain and J. F. Berry, *J. Chem. Educ.* **85**, 532 (2008).
- <sup>58</sup>A. Abragam and M. H. L. Pryce, *Proc. R. Soc. London, Ser. A* **205**, 135–153 (1951).
- <sup>59</sup>Y. Tanabe and S. Sugano, *J. Phys. Soc. Jpn.* **9**, 766 (1954).
- <sup>60</sup>M. Motokawa, *J. Phys. Soc. Jpn.* **45**, 1528 (1978).
- <sup>61</sup>G. C. DeFotis, C. D. Wallo, R. L. Smith, D. B. Bodkin, G. L. Mirabilio, T. R. Leftwich, M. G. Kim, and Z. D. Reed, *Phys. Rev. B* **71**, 224415 (2005).
- <sup>62</sup>L. Graf, *Solid State Commun.* **27**, 1361–1365 (1978).
- <sup>63</sup>L. Graf, *Phys. Status Solidi B* **88**, 429–437 (1978).
- <sup>64</sup>A. Narath, *Phys. Rev.* **139**, A1221 (1965).
- <sup>65</sup>K. A. Hay and J. B. Torrance, *Phys. Rev. B* **2**, 746 (1970).
- <sup>66</sup>H. Weitzel and J. Hirte, *Phys. Rev. B* **37**, 5414–5422 (1988).
- <sup>67</sup>M. Blume and R. E. Watson, *Proc. R. Soc. London, Ser. A* **271**, 565–578 (1963).
- <sup>68</sup>K. W. H. Stevens, *Proc. R. Soc. London, Ser. A* **219**, 542–555 (1953).
- <sup>69</sup>A. Abragam and M. H. L. Pryce, *Proc. R. Soc. London, Ser. A* **206**, 173–191 (1951).
- <sup>70</sup>First-order numerical calculation of the molecular susceptibility for  $\text{CoCl}_2 \cdot 2\text{D}_2\text{O}$  and associated fit for the crystal field parameters using the variable temperature bulk magnetic susceptibility data of  $\text{CoCl}_2 \cdot 2\text{H}_2\text{O}$  obtained by Narath<sup>28</sup> was also carried out using *Mathematica*.
- <sup>71</sup>Narath made a few *ad hoc* modifications to several magnetic moment matrix elements, corrections which we have neglected.
- <sup>72</sup>These values are slightly different than those reported by Narath and lead to an insubstantially different zero field energy level structure. Using his reported  $\Delta$  values, we can replicate his zero field energy level structure and some, but not all, of his reported effective  $g$ -values, leading us to suspect a calculation error in the original analysis.
- <sup>73</sup>K. Juraitis, J. Domiciano, and W. Sano, *J. Phys. Chem. Solids* **44**, 531 (1983).
- <sup>74</sup>G. C. DeFotis, J. G. McMahon, J. M. Berlin, J. A. Duling, and R. B. Jeffers, *J. Appl. Phys.* **87**, 6052 (2000).
- <sup>75</sup>E. Buluggiu, G. Dascola, D. C. Giori, and A. Vera, *J. Chem. Phys.* **54**, 2191 (1971).
- <sup>76</sup>Y. Servant, J.-C. Bissey, and M. Maini, *Physica B+C* **106**, 343 (1981).
- <sup>77</sup>H. D. Lutz, “Bonding and structure of water molecules in solid hydrates. Correlation of spectroscopic and structural data,” in *Structure and Bonding*, edited by M. J. Clarke, J. B. Goodenough, J. A. Ibers, C. K. Jørgensen, D. M. P. Mingos, J. B. Neilands, G. A. Palmer, D. Reinen, P. J. Sadler, R. Weiss, and R. J. P. Williams (Springer Berlin Heidelberg, Berlin, Heidelberg, 1988), Vol. 69, pp. 97–125.
- <sup>78</sup>R. Sjöblom and J. Tegenfeldt, *J. Magn. Reson.* **27**, 405 (1977).
- <sup>79</sup>B. Berglund and J. Tegenfeldt, *J. Mol. Struct.* **40**, 139 (1977).
- <sup>80</sup>B. Morosin and E. J. Graeber, *J. Chem. Phys.* **42**, 898 (1965).
- <sup>81</sup>B. Morosin, *J. Chem. Phys.* **44**, 252–257 (1966).
- <sup>82</sup>B. Morosin, *Acta Cryst.* **23**, 630 (1967).
- <sup>83</sup>Å. Engberg, *Acta Chem. Scand.* **24**, 3510 (1970).
- <sup>84</sup>A. Narath, *Phys. Rev.* **136**, A766 (1964).
- <sup>85</sup>D. E. Cox, G. Shirane, B. Frazer, and A. Narath, *J. Appl. Phys.* **37**, 1126 (1966).
- <sup>86</sup>W. Schneider and H. Weitzel, *Acta Crystallogr., Sect. A* **32**, 32 (1976).
- <sup>87</sup>K. Momma and F. Izumi, *J. Appl. Crystallogr.* **44**, 1272 (2011).
- <sup>88</sup>D. Harker, *Z. Kristallogr. - Cryst. Mater.* **93**, 136 (1936).
- <sup>89</sup>S. W. Peterson and H. A. Levy, *J. Chem. Phys.* **26**, 220 (1957).
- <sup>90</sup>D. Cox, B. Frazer, and G. Shirane, *Phys. Lett.* **17**, 103 (1965).
- <sup>91</sup>Y. Hazony, R. Axtmann, and J. Hurley, *Chem. Phys. Lett.* **2**, 440 (1968).
- <sup>92</sup>W. H. Baur, *Acta Crystallogr.* **19**, 909 (1965).
- <sup>93</sup>Z. M. E. Saffar, *J. Chem. Phys.* **52**, 4097–4099 (1970).
- <sup>94</sup>R. Kiriya, H. Kiriya, K. Kitahama, and O. Nakamura, *Chem. Lett.* **2**, 1105 (1973).
- <sup>95</sup>L. E. Drain, *Proc. Phys. Soc., London* **80**, 1380 (1962).
- <sup>96</sup>A. Kubo, T. P. Spaniol, and T. Terao, *J. Magn. Reson.* **133**, 330 (1998).
- <sup>97</sup>J. A. Osborn, *Phys. Rev.* **67**, 351–357 (1945).
- <sup>98</sup>S. Moon and S. Patchkovskii, “First-principles calculations of paramagnetic NMR shifts,” in *Calculation of NMR and EPR Parameters, Theory and Applications*, edited by M. Kaupp, M. Bühl, and V. G. Malkin (Wiley-VCH Verlag GmbH & Co. KGaA, Weinheim, FRG, 2004), Chap. 20, pp. 325–338.
- <sup>99</sup>T. Pennanen and J. Vaara, *Phys. Rev. Lett.* **100**, 133002 (2008).
- <sup>100</sup>A. Soncini and W. Van den Heuvel, *J. Chem. Phys.* **138**, 021103 (2013).
- <sup>101</sup>W. Van den Heuvel and A. Soncini, *J. Chem. Phys.* **138**, 054113 (2013).
- <sup>102</sup>M. Odelius, C. Ribbing, and J. Kowalewski, *J. Chem. Phys.* **104**, 3181–3188 (1996).
- <sup>103</sup>J. Mareš, M. Hanni, P. Lantto, J. Lounila, and J. Vaara, *Phys. Chem. Chem. Phys.* **16**, 6916–6924 (2014).
- <sup>104</sup>A. Bhaumik, C. Luchinat, G. Parigi, E. Ravera, and M. Rinaldelli, *Cryst. Eng. Commun.* **15**, 8639 (2013).
- <sup>105</sup>R. J. Kurland and B. R. McGarvey, *J. Magn. Reson.* **2**, 286–301 (1970).
- <sup>106</sup>A. J. Pell, G. Pintacuda, and C. P. Grey, “Paramagnetic NMR in solution and the solid state,” *Prog. Nucl. Magn. Reson. Spectrosc.* (in press).
- <sup>107</sup>R. P. Feynman, *Phys. Rev.* **56**, 340–343 (1939).

# Supplementary Information–Hydrogen motional disorder in crystalline iron group chloride dihydrates

Brennan J. Walder, Alex M. Patterson, and Philip J. Grandinetti\*

*Department of Chemistry, Ohio State University,  
100 West 18th Avenue, Columbus, OH 43210, USA*

Jay H. Baltisberger

*Division of Natural Science, Mathematics, and Nursing,  
Berea College, Berea, Kentucky 40403, USA*

---

\* <http://www.grandinetti.org>

## CONTENTS

I. Sample Preparation and Purification	2
A. $\text{CuCl}_2 \cdot 2\text{D}_2\text{O}$	2
B. $\text{NiCl}_2 \cdot 2\text{D}_2\text{O}$	3
C. $\text{CoCl}_2 \cdot 2\text{D}_2\text{O}$	3
D. $\text{FeCl}_2 \cdot 2\text{D}_2\text{O}$	3
E. $\text{MnCl}_2 \cdot 2\text{D}_2\text{O}$	4
II. NMR parameters	5
III. Low temperature shifting <i>d</i> -echo spectrum	7
IV. Crystal field energy levels	8
V. Contributions to spin-orbit dequenched molecular susceptibility	12
VI. Motional model survey for pyramidal coordination in $\text{NiCl}_2 \cdot 2\text{D}_2\text{O}$	14
VII. Tensor averaging by torsional motion	18
VIII. Marginal parameter distributions	20
IX. Structural parameters and water ligand geometry	42
References	42

## I. SAMPLE PREPARATION AND PURIFICATION

### A. $\text{CuCl}_2 \cdot 2\text{D}_2\text{O}$

A large quantity of crude  $\text{CuCl}_2 \cdot 2\text{D}_2\text{O}$  was produced by dissolving anhydrous  $\text{CuCl}_2$  (97 %, Sigma Aldrich) into approximately 20 mL of  $\text{D}_2\text{O}$  (99.9 % D, Cambridge Isotopes) and evaporating to dryness in a desiccator. 7 g of the large, deep green stock crystals were later dissolved in 8 mL heavy water acidified by addition of a drop of 20 % DCl in  $\text{D}_2\text{O}$  (Aldrich) and dried under  $\text{N}_2$  flow. Care was taken not to expose the crystals to high rates of  $\text{N}_2$  flow after it was found the crystals would, over the course of several minutes, revert to the anhydrous form under these conditions.

This material was stored for over a year and was purified with the enrichment apparatus described in the main text prior to this study. 5.9 g of the crude sample added to the flask and dissolved into 6.0 mL of 8 % DCl in  $\text{D}_2\text{O}$  at room temperature. Evaporation under  $\text{N}_2$  counterflow and magnetic stirring produced a slurry after three hours. To achieve thorough drying and avoid signal contamination from occluded heavy water, the flask was then pumped down with high vacuum for an hour, with occasional application of weak  $\text{N}_2$  counterflow to allow manual agitation and breakup of solid with a plastic stir rod. With this drying procedure, initially dense clumps of vivid, deep green crystals converted to larger cyan crystals and needles after about 10 min. The final product was a loose, sea green powder as shown in Fig. S1.

### B. $\text{NiCl}_2 \cdot 2\text{D}_2\text{O}$

A mass of 5 g of  $\text{NiCl}_2 \cdot 6\text{H}_2\text{O}$  (Sigma Aldrich) was partially dehydrated in the enrichment apparatus at temperatures exceeding 100 °C for 4 hours. The solution was then cooled to 80 °C. At this temperature the flask was charged twice with 2.5 mL of a diluted 2 % DCl in  $\text{D}_2\text{O}$  solution, with the crystals dried under nitrogen flow between charges to afford a yellow-green batch of crystals. Initial NMR analysis of these crystals indicated probable hexahydrate contamination.

This material was stored for several months and purified prior to NMR analysis. The enrichment apparatus described in the main text was charged with 3.1 g of old  $\text{NiCl}_2 \cdot 2\text{D}_2\text{O}$  which was dissolved into 4 mL of pure  $\text{D}_2\text{O}$  at 95 °C. Over the next two hours two additional charges of  $\text{D}_2\text{O}$  were added as a slurry began to form, culminating with a 2 mL charge of 8 % DCl in  $\text{D}_2\text{O}$ . After another two hours at 95 °C in  $\text{N}_2$  atmosphere the slurry was thoroughly dried by applying high vacuum for 45 min. The final product was a banana yellow powder as shown in Fig. S1.

### C. $\text{CoCl}_2 \cdot 2\text{D}_2\text{O}$

A large quantity of crude  $\text{CoCl}_2 \cdot 6\text{H}_2\text{O}$  was produced by dissolving anhydrous  $\text{CoCl}_2$  (Alfa/Morton Thiokol Inc.) into approximately 10 mL of slightly acidified (< 1 % DCl) heavy water and evaporating to dryness in a desiccator. A mass of 5 g of the crude material transferred into the enrichment apparatus and wetted with 1 mL 20 % DCl/ $\text{D}_2\text{O}$  at 70 °C. Crystals were dried under  $\text{N}_2$  while held at 70 °C with occasional light manual agitation by a plastic stirring rod.

This material was stored for several months and purified prior to NMR analysis. The enrichment apparatus described in the main text was charged with 2.2 g of old  $\text{CoCl}_2 \cdot 2\text{D}_2\text{O}$  which was dissolved into 2.5 mL of 8 % DCl in  $\text{D}_2\text{O}$ . The solution was held at 70 °C under nitrogen for several hours prior to dryness under high vacuum. The final product were light purple crystals as shown in Fig. S1.

### D. $\text{FeCl}_2 \cdot 2\text{D}_2\text{O}$

A mass of 4.4281 g  $\text{FeCl}_2 \cdot 4\text{H}_2\text{O}$  (Sigma Aldrich) was placed directly into the enrichment apparatus and dried overnight at 70°C. It was subsequently charged with 5 mL of a 1.8 % DCl/ $\text{D}_2\text{O}$  solution and a 192 mg piece of pure iron metal. After crystallization another 4.9 mL of 1.8 %  $\text{D}_2\text{O}$ /DCl solution was added. After cooling to 40°C four additional shots of 2.5 mL of 2 % DCl/ $\text{D}_2\text{O}$  were added over four hours, each at the stage when precipitation was well underway but not complete. After raising the temperature of the solution to 70 °C and holding the wet crystals were dried under high vacuum for 20 min resulting in a hard concrete-like mat of solid. The iron chip was removed with the stir bar in the glove bag. The freshly crushed powder was nearly pure white with only a faint tinge of green, as shown in Fig. S1, but darkened noticeably in the days following the synthesis.

After several months the powder had turned a much deeper shade of green and had to be purified prior to NMR analysis. The enrichment apparatus described in the main text was charged with 3.0 g of the crude material which was dissolved into 4.3 mL of 8 % DCl in  $\text{D}_2\text{O}$ . A small chip of pure iron metal was added to reduce  $\text{Fe}^{3+}$ . Over the course of



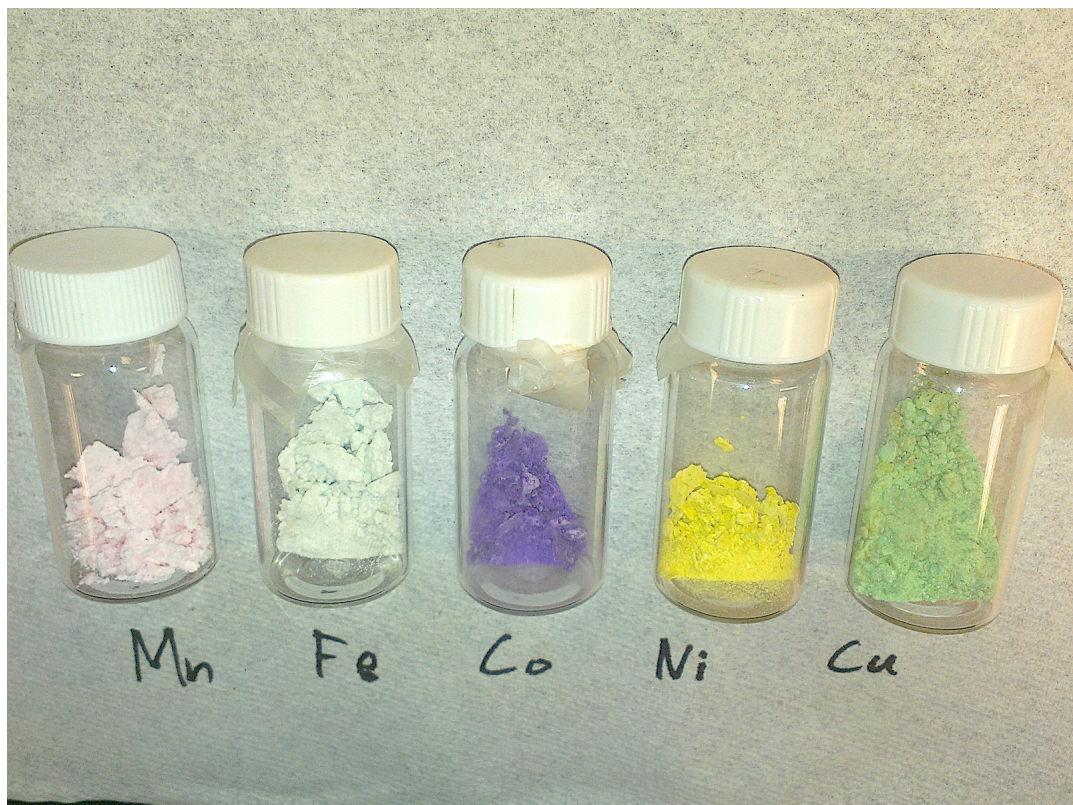


Figure S1: Photograph of the  $\text{MCl}_2 \cdot 2\text{D}_2\text{O}$  samples used in this study.

several hours the oil bath temperature was raised from 45 °C to 85 °C, driving off the excess solution. Dryness was completed by gradual application of high vacuum near 75 °C. The iron chip was removed along with the stir bar in the glove bag. The final product was a white powder consisting of small crystallites after crushing.

#### E. $\text{MnCl}_2 \cdot 2\text{D}_2\text{O}$

An initial batch was prepared by dehydrating 5 g  $\text{MnCl}_2 \cdot 4\text{H}_2\text{O}$  (Merck) above 155 °C for 6 h to produce anhydrous  $\text{MnCl}_2$ . After cooling the flask to 80 °C, 6.5 mL of 2 % DCl in  $\text{D}_2\text{O}$  was added, followed by an additional 3.0 mL to complete dissolution of the powder. Drying under  $\text{N}_2$  flow proceeded at this temperature with occasional manual agitation using a plastic stir rod.

This material was stored for several months and purified prior to NMR analysis. The enrichment apparatus described in the main text was charged with 2.9 g of old  $\text{MnCl}_2 \cdot 2\text{D}_2\text{O}$  which was dissolved into 4.3 mL of 8 % DCl in  $\text{D}_2\text{O}$ . The solution was held at 80 °C under nitrogen for two hours prior to dryness under high vacuum. Pale pink crystals.

## II. NMR PARAMETERS

Table S-I gives rf transmission parameters used for each experiment. The maximum rf amplitude we could generate with this coil was  $\nu_1(^2\text{H}) = 660$  kHz but values closer to  $\nu_1(^2\text{H}) = 350$  kHz were generally obtained after dematching the probe.

$T_1$  measurements on the samples were performed using a shifted  $dp$ -echo version of the Freeman and Hill modified inversion recovery sequence. These  $T_1$  values are shown in Table S-II along with  $\chi_{\text{red}}^2$  for the fit to the exponential decay. The long wait period was 50 ms. The echo delay used was 160  $\mu\text{s}$  for each experiment, except for  $\text{NiCl}_2 \cdot 2\text{D}_2\text{O}$  and  $\text{FeCl}_2 \cdot 2\text{D}_2\text{O}$ , which used echo shifts of 80  $\mu\text{s}$ . This shows that 50 ms is sufficient for full  $^2\text{H}$  relaxation.

Table S-III lists the acquisition parameters for each of the shifting  $d$ -echo experiments. A recycle delay of 50 ms was used. Each experiment was completed in less than 5 h, with the exception of the  $\text{CoCl}_2 \cdot 2\text{D}_2\text{O}$  and  $\text{MnCl}_2 \cdot 2\text{D}_2\text{O}$  experiments, which were allowed to run overnight. A 64-step nested phase cycle was employed, with each pulse phase independently stepped in multiples of  $\pi/2$  and the receiver phase given by  $\phi_R = \phi_1 - 2\phi_2 + 2\phi_3$ .

Sample	Attn	$P_{\text{tx}} / \text{W}$	$\tau_{90} / \mu\text{s}$	$\tau_{180} / \mu\text{s}$
$\text{MnCl}_2 \cdot 2\text{D}_2\text{O}$	11.0 dB	1459	0.74	1.47
$\text{FeCl}_2 \cdot 2\text{D}_2\text{O}$	16 dB	1400	0.71	1.42
$\text{CoCl}_2 \cdot 2\text{D}_2\text{O}$	11.8 dB	1306	0.77	1.54
$\text{NiCl}_2 \cdot 2\text{D}_2\text{O}$	14.9 dB	1153	0.78	1.56
$\text{CuCl}_2 \cdot 2\text{D}_2\text{O}$	17.3 dB	1270	0.75	1.50

Table S-I: Power settings and pulse length settings used for all experiments. ‘Attn’ refers to attenuation of the pulses by the probe when dematched and was measured with an oscilloscope via a directional coupler.

Sample	$T_1 / \text{ms}$	$\chi_{\text{red}}^2$
$\text{CuCl}_2 \cdot 2\text{D}_2\text{O}$	9.8	2.60
$\text{NiCl}_2 \cdot 2\text{D}_2\text{O}$	4.5	18.33
$\text{CoCl}_2 \cdot 2\text{D}_2\text{O}$	9.2	5.27
$\text{FeCl}_2 \cdot 2\text{D}_2\text{O}$	7.6	2.05
$\text{MnCl}_2 \cdot 2\text{D}_2\text{O}$	4.4	6.78

Table S-II: Longitudinal relaxation parameters at  $T = 300.0$  K by fitting the exponential decay function  $M_z(t) = M_0 e^{-t/T_1}$  to Freeman-Hill inversion recovery data.

Sample	$\tau$ / $\mu\text{s}$	$(\Delta t_2, \Delta t_1)/\mu\text{s}$	(TD <sub>2</sub> ,TD <sub>1</sub> )	Scans
MnCl <sub>2</sub> · 2D <sub>2</sub> O	80	(1.6, 3.2)	(192, 80)	8192
FeCl <sub>2</sub> · 2D <sub>2</sub> O	40	(2.0, 4.0)	(256, 40)	7168
CoCl <sub>2</sub> · 2D <sub>2</sub> O	80	(1.6, 3.2)	(192, 80)	8192
NiCl <sub>2</sub> · 2D <sub>2</sub> O	160	(2.0, 4.0)	(256, 48)	7168
CuCl <sub>2</sub> · 2D <sub>2</sub> O	160	(1.6, 3.2)	(384, 83)	2048

Table S-III: Acquisition parameters for the shifting  $d$ -echo experiments.  $\Delta t_2$  and  $\Delta t_1$  are the respective dwell times for the direct and indirect dimensions. TD<sub>2</sub> and TD<sub>1</sub> refer to the number of directly acquired complex points and the number of  $t_1$  increments used, respectively.

### III. LOW TEMPERATURE SHIFTING *d*-ECHO SPECTRUM

A shifting *d*-echo spectrum of  $\text{NiCl}_2 \cdot 2\text{D}_2\text{O}$  taken at 173 K is shown in Fig. S2. This spectrum is processed in the same way those of the main text. The line shape was analyzed for the tensor parameters given in Tab. S-IV. Though the two ligand deuterons are potentially inequivalent when the ligand is frozen, the single site model provides a reasonable coarse description of the line shape. The instantaneous value of  $\zeta_P = 1320$  ppm we find in this analysis would, with scaling according to a Curie law  $T^{-1}$  dependence, correspond to 760 ppm at 300 K. This is slightly larger but, on the whole, comparable to the instantaneous values predicted for the three sites listed in Table IV. of the main text. Also, note that this spectrum was recorded below the crystallographic phase transition around 220 K, [1] which is associated with slight shifts in the relative positions of the chains. This transition, along with the anticipated deuteron inequivalence at 173 K, prevents a comparison with the room temperature data from being anything more than qualitative.

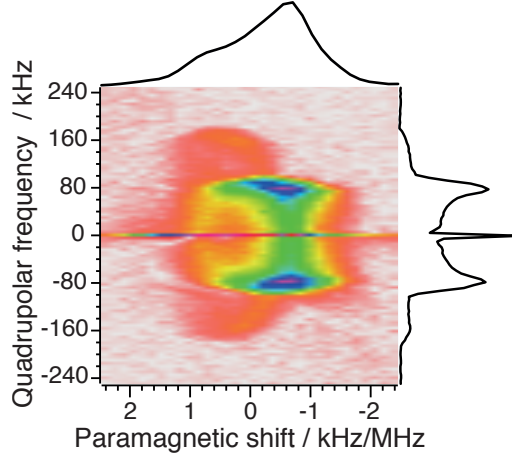


Figure S2: Shifting *d*-echo spectrum of  $\text{NiCl}_2 \cdot 2\text{D}_2\text{O}$  taken at  $T = 173$  K. Temperature stabilization was lost and the temperature began to increase roughly 3 h into the experiment, reaching 188 K after 4 h and 220 K after the 5 h experiment had completed. The effect on the line shape is minimal as the desired signals (save for the total echo artifact) had decayed in  $t_1$  after 3 h.

$P_{\text{iso}}$ / ppm	$\zeta_P$ / ppm	$\eta_P$	$C_q$ / kHz	$\eta_q$	$\alpha_{\text{rel}}$	$\beta_{\text{rel}}$	$\gamma_{\text{rel}}$
-200	1320	0.2	230	0.1	50°	40°	20°

Table S-IV: Single site best fit tensor parameters determined from the sheared 2D shifting-*d* echo line shape for  $\text{NiCl}_2 \cdot 2\text{D}_2\text{O}$  at 173 K.



#### IV. CRYSTAL FIELD ENERGY LEVELS

Figs. S3-S6 illustrate the weak crystal field approach to determining the zero field structure of the magnetically active manifold for the iron group chloride dihydrates, meant to provide qualitative visual accompaniment to the descriptions in the main text. Symmetry labels are provided according to isolated  $[\text{MCl}_4(\text{D}_2\text{O})_2]^{-2}$  complexes of pseudo- $D_{2h}$  point group symmetry. Energy levels are not drawn to scale. The symmetry labels, particularly for excited states, may not always correspond to the correct energy ordering.

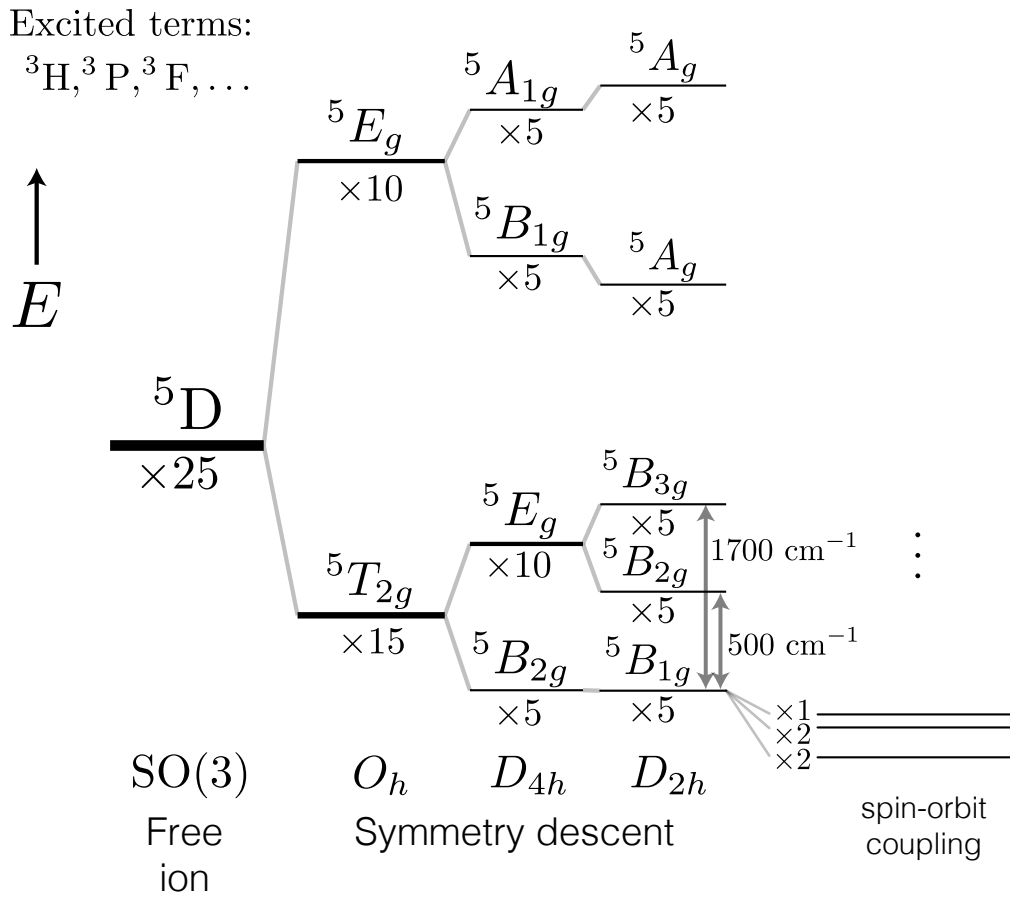


Figure S3: Lifting of  $\text{Fe}^{2+}$  free ion degeneracy in the weak crystal field of  $[\text{FeCl}_4(\text{D}_2\text{O})_2]^{-2}$  through successive imposition of the cubic, axial, and rhombic components of the crystal field. The spin-orbit coupling lifts the fivefold spin degeneracy of the  $D_{2h}$  orbital singlets.

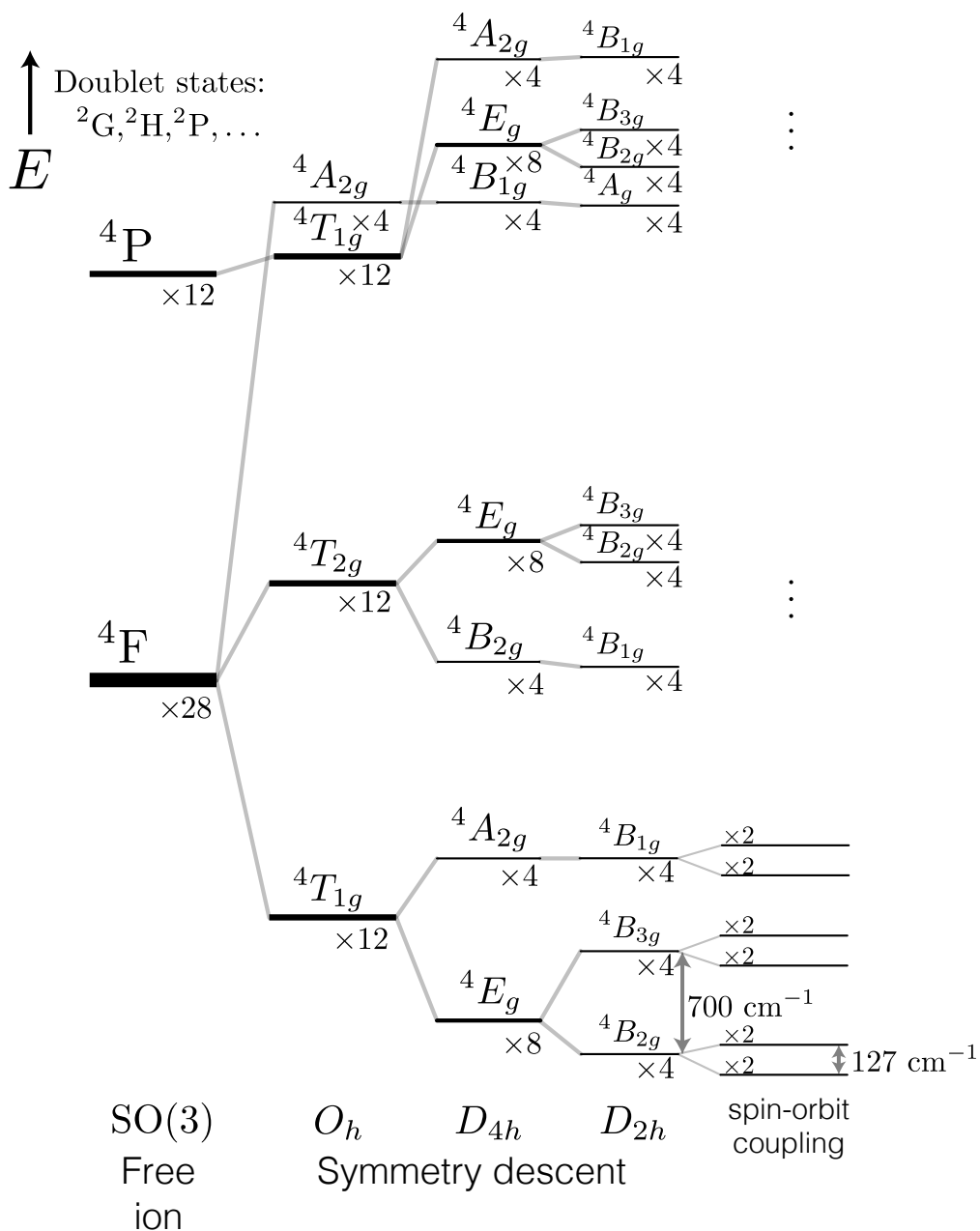


Figure S4: Lifting of  $\text{Co}^{2+}$  free ion degeneracy in the weak crystal field of  $[\text{CoCl}_4(\text{D}_2\text{O})_2]^{-2}$  through successive imposition of the cubic, axial, and rhombic components of the crystal field. The spin-orbit coupling lifts the fourfold spin degeneracy of the  $D_{2h}$  orbital singlets.

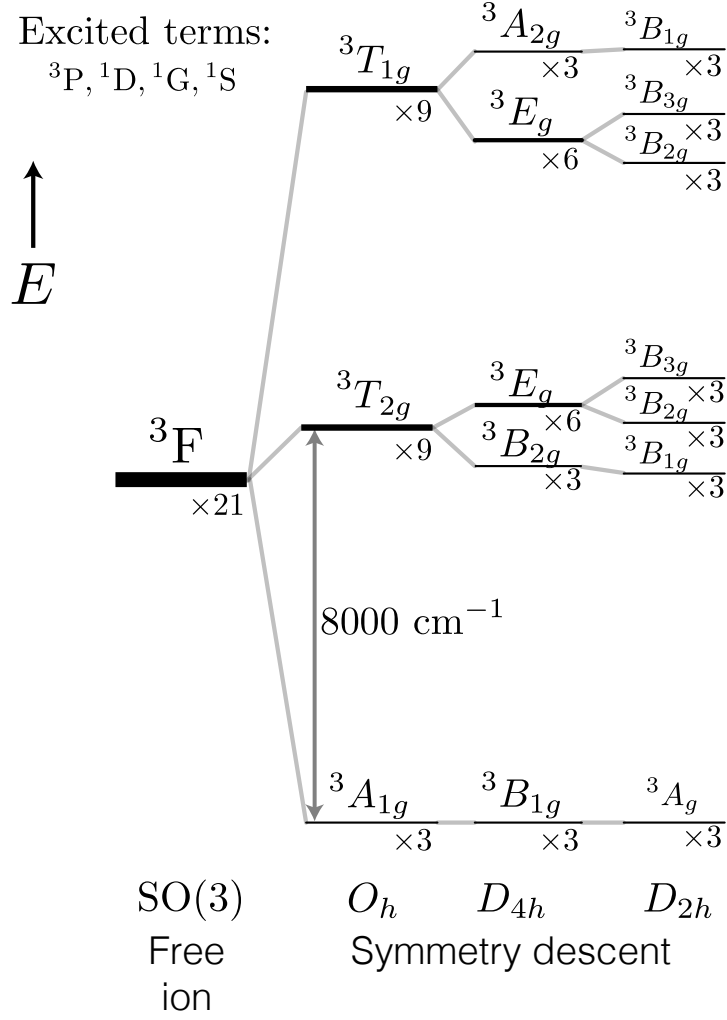


Figure S5: Lifting of  $\text{Ni}^{2+}$  free ion degeneracy in the weak crystal field of  $[\text{NiCl}_4(\text{D}_2\text{O})_2]^{-2}$  through successive imposition of the cubic, axial, and rhombic components of the crystal field. Spin-orbit coupling lifts the threefold spin degeneracy of the ground orbital singlet; this effect is not shown as we neglect this relatively small influence in the main text. States originating from the relatively low lying  ${}^3\text{P}$  and  ${}^1\text{D}$  terms are not shown.

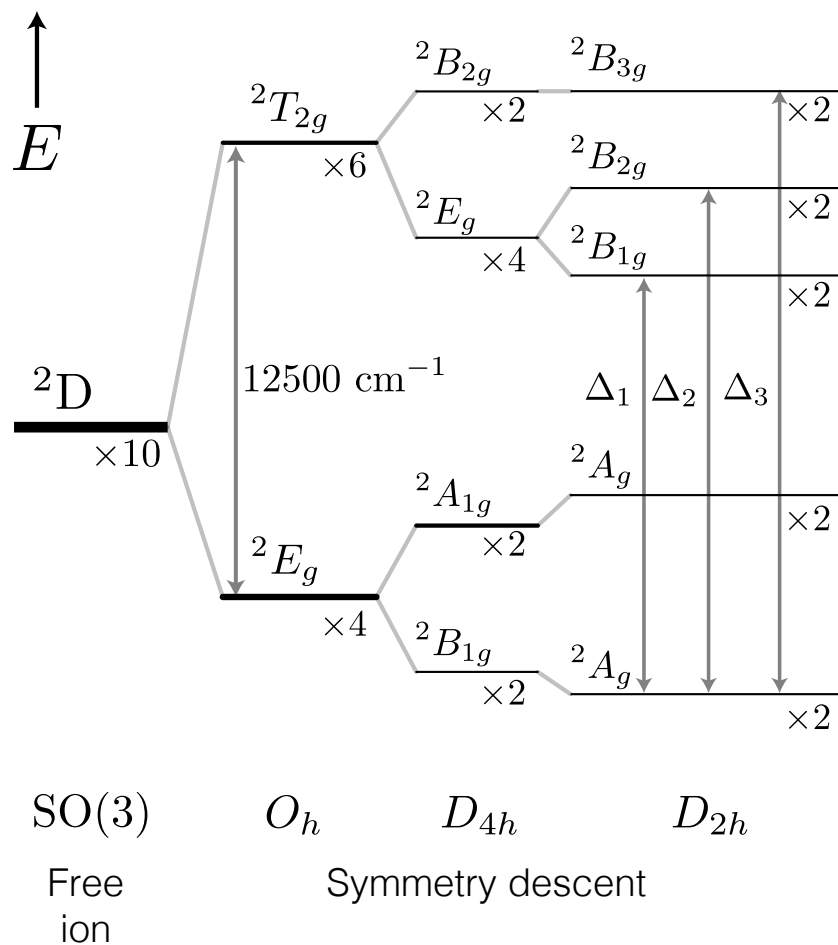


Figure S6: Lifting of  $\text{Cu}^{2+}$  free ion degeneracy in the weak crystal field of  $[\text{CuCl}_4(\text{D}_2\text{O})_2]^{-2}$  through successive imposition of the cubic, axial, and rhombic components of the crystal field. Spin-orbit coupling is unable to lift the Kramers degeneracy of the orbital singlets.



## V. CONTRIBUTIONS TO SPIN-ORBIT DEQUENCHED MOLECULAR SUSCEPTIBILITY

Term	CuCl <sub>2</sub> · 2D <sub>2</sub> O			NiCl <sub>2</sub> · 2D <sub>2</sub> O		
	$\chi_{xx} / \text{\AA}^3$	$\chi_{yy} / \text{\AA}^3$	$\chi_{zz} / \text{\AA}^3$	$\chi_{xx} / \text{\AA}^3$	$\chi_{yy} / \text{\AA}^3$	$\chi_{zz} / \text{\AA}^3$
Temperature independent	0.00029	0.00065	0.00215	0.00393	0.00393	0.00393
Curie	0.02733	0.02882	0.03545	0.08980	0.08980	0.08980
ZFS	0	0	0	0	0	0
Total	0.02762	0.02947	0.03760	0.09373	0.09373	0.09373

Term	FeCl <sub>2</sub> · 2D <sub>2</sub> O			MnCl <sub>2</sub> · 2D <sub>2</sub> O		
	$\chi_{xx} / \text{\AA}^3$	$\chi_{yy} / \text{\AA}^3$	$\chi_{zz} / \text{\AA}^3$	$\chi_{xx} / \text{\AA}^3$	$\chi_{yy} / \text{\AA}^3$	$\chi_{zz} / \text{\AA}^3$
Temperature independent	0.00632	0.00632	0.02157	0	0	0
Curie	0.23115	0.23115	0.28989	0.29039	0.29039	0.29039
ZFS	-0.00881	-0.00881	0.02209	0	0	0
Total	0.22866	0.22866	0.33355	0.29039	0.29039	0.29039

Table S-V: Individual contributions of the temperature independent, Curie, and ZFS terms to the spin-orbit dequenched molecular susceptibility eigenvalues.

Table S-V lists the contribution of each term in the formula for calculating the molecular susceptibility using the orbital angular momentum dequenching tensor,  $\mathbf{\Lambda}$ , which was used for CuCl<sub>2</sub> · 2D<sub>2</sub>O, NiCl<sub>2</sub> · 2D<sub>2</sub>O, FeCl<sub>2</sub> · 2D<sub>2</sub>O, and MnCl<sub>2</sub> · 2D<sub>2</sub>O. The molecular susceptibility for CoCl<sub>2</sub> · 2D<sub>2</sub>O was calculated numerically using the first-order approach described in the main text; further details are given in Fig. S7.

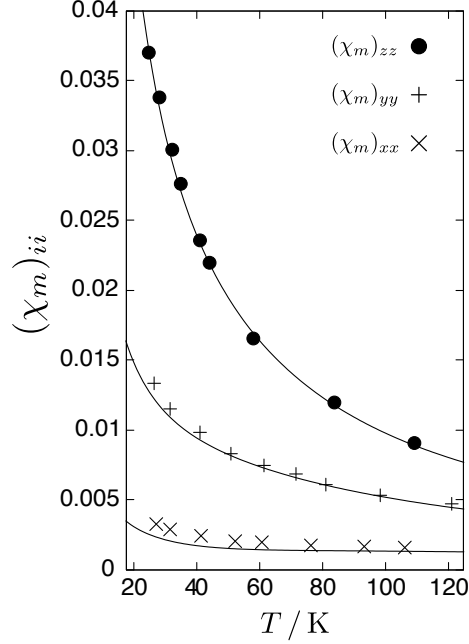


Figure S7: Temperature dependence of the  $\text{CoCl}_2 \cdot 2\text{D}_2\text{O}$  principal components of the bulk magnetic susceptibility tensor  $\chi_m$  (S. I., dimensionless) using data taken from Fig. 12, Ref. [2], according to the reanalysis procedure described in the main text. The curves represent the susceptibility calculated with the full Van Vleck equation using our numerical model given the crystal field parameters  $\Delta_{\text{ax}}$  and  $\Delta_{\text{rh}}$ . The values  $\Delta_{\text{ax}} = -125$  meV and  $\Delta_{\text{rh}} = -43$  meV are determined by fitting Narath's experimental bulk magnetic susceptibility data, shown as points clustering around their respective curves, for the three principal components simultaneously. Significant deviation from Curie-Weiss behavior, particularly for  $(\chi_m)_{xx}$ , which displays a strong temperature independent component, is noteworthy. Owing to this behavior, our analysis predicts interchange of the Haebleren labeled  $z$ - and  $x$ -axes near 163 K. Independent of any labeling convention, at all temperatures the component of least magnitude is very nearly aligned with the short Co-Cl bonds.

## VI. MOTIONAL MODEL SURVEY FOR PYRAMIDAL COORDINATION IN $\text{NiCl}_2 \cdot 2\text{D}_2\text{O}$

In Fig. S8, we show ternary plots illustrating the values of  $|\langle\zeta_q\rangle/\zeta_q|$  and  $\langle\eta_q\rangle$  for general cases of site occupancy where the  $p_i$  values are arbitrary, subject to the constraint that they sum to unity. The plots exhibit three-fold rotational and reflection symmetries, corresponding to eigenvalue invariance under cyclic permutation and swapping of the  $p_i$  indices, respectively. This is equivalent to applying active physical rotation and reflection operations to the deuteron coordinates, from which this invariance can be proven. Therefore, the order of the  $p_i$  is not relevant in the analysis of the quadrupolar tensor eigenvalues.

Diagrams are shown for specific values of  $\theta_w$  of  $50^\circ$ ,  $52.5^\circ$ , and  $\theta_M \approx 54.7^\circ$ , the latter corresponding to the case where the D–O–D bond angle is exactly the tetrahedral angle. We see clearly that  $\langle\eta_q\rangle$  is a highly discriminating parameter. For ideal tetrahedral geometry,  $\theta_w = \theta_M$ ,  $\langle\eta_q\rangle = 1$  if and only if at least one of the  $p_i = 0.5$ . At the other extreme,  $\langle\eta_q\rangle = 0$  for the case of equal occupancy,  $p_1 = p_2 = p_3 = 1/3$ . As  $\theta_w$  is lowered toward  $50^\circ$ ,  $\langle\eta_q\rangle$  remains zero for the case of equal occupancy, though having at least one of the  $p_i = 0.5$  is no longer a necessary nor sufficient condition for  $\langle\eta_q\rangle = 1$ . Nevertheless, we see that even with a D–O–D angle as low as  $100^\circ$ , one of the  $p_i$  must be greater than 0.4 to satisfy our experimental observation of  $\langle\eta_q\rangle$  near unity.

This leaves few regions of compatibility. Consider now without loss of generality a value of  $p_2$  between 0.4 and 0.45, being the largest of the  $p_i$ , to define one such region. We see that with the additional condition  $p_1 = p_3$ , we move towards the barycenter of the diagram, where, depending on the value of  $\theta_w$ , either  $\langle\eta_q\rangle$  or  $|\langle\zeta_q\rangle/\zeta_q|$  is much smaller than the experimentally observed values. With  $p_1 = p_2$ , we consider a region closer the vertex of the diagram, and here we can approach compatible eigenvalues provided  $\theta_w \approx 52.5^\circ$ . While decreasing  $\theta_w$  and increasing  $p_2$ , we can either increase  $p_1$  or  $p_3$  to follow a region of improving compatibility up to the diagram boundary where  $p_2 = 0.5$ . The only other distinct region of compatibility is bounded by the edge of the diagram and the curved  $\langle\eta_q\rangle = 1$  boundary. The furthest point away from the  $\langle\eta_q\rangle = 1$  boundary has  $p_2 = 0.5$  and  $p_1 = p_3 = 0.25$ . Here the best agreement is found when  $\theta_w \gtrsim 52.5^\circ$ .

This exhausts the significantly distinct possibilities. Corresponding to each of these regions, we investigate the solutions of significance given in the following Table S-VI:

Motional characteristic	$(p_1, p_2, p_3)$	$\theta_w$	$ \langle\zeta_q\rangle/\zeta_q $	$\langle\eta_q\rangle$
Encumbered rotation	(0.424, 0.424, 0.152)	$52.9^\circ$	0.343	0.806
Right-skewed vertex pivoting	(0.369, 0.5, 0.131)	$51.1^\circ$	0.336	0.914
Symmetric vertex pivoting	(0.25, 0.5, 0.25)	$53.6^\circ$	0.336	0.915
Left-skewed vertex pivoting	(0.131, 0.5, 0.369)	$51.1^\circ$	0.336	0.914

Table S-VI: Definition of the four distinct classes of motion in  $\text{NiCl}_2 \cdot 2\text{D}_2\text{O}$  compatible with the experimentally observed quadrupolar tensor parameters.

Although the order of the  $p_i$  values is not relevant in the analysis of the quadrupolar tensor eigenvalues, the ordering does affect the result of the paramagnetic shift since the lattice coordinates are not affected by the ligand symmetry operations that achieve the exchange of indices. Ultimately, simulations of full correlation spectra, which brings in five additional

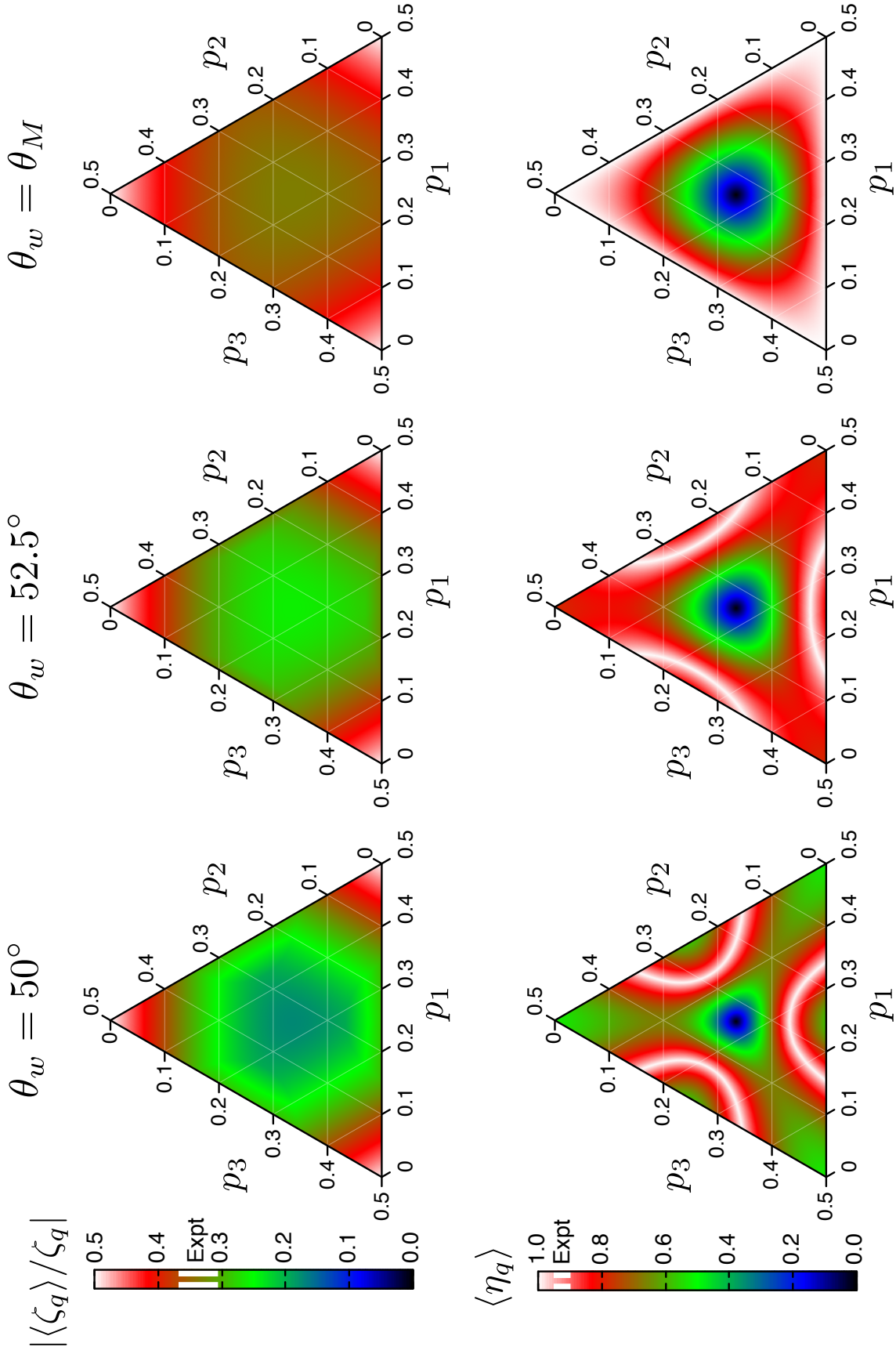


Figure S8: Ternary plots of the motionally averaged quadrupolar tensor parameters  $|\langle \zeta_q \rangle / \zeta_q|$  and  $\langle \eta_q \rangle$  versus the occupancy weighting factors  $(p_1, p_2, p_3)$  for pyramidal ligand coordination for three different values of  $\theta_w$ .



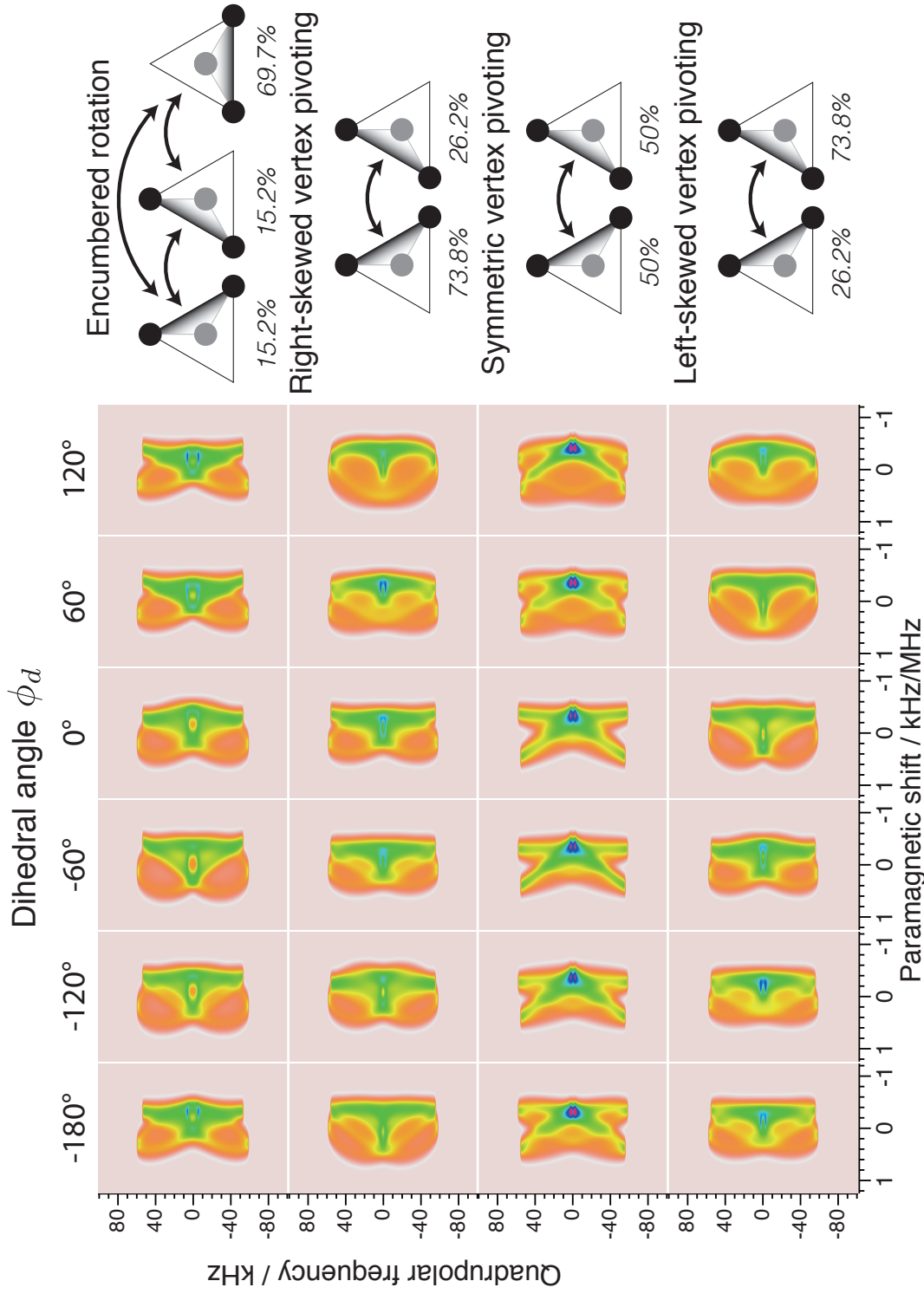


Figure S9: Simulated quadrupole and paramagnetic shift correlation NMR spectra for the four potentially suitable classes of motion in  $\text{NiCl}_2 \cdot 2\text{D}_2\text{O}$ , sampled for six values of  $\phi_d$ . The quadrupole tensor parameters for each class is taken from Table S-VI. The paramagnetic shift tensor is calculated in the lattice-fixed frame with the procedure described in the main text. For the purposes of these calculations, the dipole sources were localized entirely on nickel atoms. Schematics giving the proportion of whole-body ligand configurations that lead to the occupancy factors for each site given in Table S-VI for each class of motion appear to the right of the simulated spectra.

parameters (the paramagnetic shift tensor eigenvalues and its relative orientation to the quadrupole coupling tensor), must be carried out to further screen candidates. Because an appropriate value of  $\phi_d$  is not known, the entire range between  $-\pi$  and  $\pi$  is surveyed. This automatically accounts for the models that differ only by cyclic permutation of the indices, since this is equivalent to an active  $2\pi/3$  rotation. When two of the  $p_i$  are equal, the time-averaged configuration of the ligand is superposable on its mirror image and configurations that differ only by swapping two of the indices are automatically accounted for as well. Of the aforementioned classes, only the skewed vertex pivoting models have  $p_1 \neq p_2 \neq p_3$ , and for these we must consider the distinct left-handed and right-handed cases separately, giving four classes in total. For each of these, six values of  $\phi_d$  are chosen and the correlation spectra simulated as shown in Fig. S9. cursory visual inspection eliminates all but the symmetric vertex pivoting model as viable candidates. Furthermore, the similarity of the encumbered rotation model to the skewed vertex pivoting models suggests that any model in the transition zone, where  $\theta_w$  is decreased and  $p_2$  is increased from 0.424 to 0.5 with compensating changes in  $p_1$ , and  $p_3$ , will also fail to be a suitable candidate. Thus, the motional model with  $p_2 = 0.5$  and  $p_1 = p_3 = 0.25$  is uniquely the superior motional model, affirming the choice we made using the less rigorous but physically transparent subset analysis in the main text.

Mode	Torsion axis, $\alpha$	$\mathcal{I}_\alpha / (\text{u } \text{\AA}^2)$	$\omega_\alpha / \text{THz}$	$\langle \theta_\alpha^2 \rangle / \text{rad}^2$
Wag	$x_w$	1.197	7.49	0.105
Twist	$y_w$	2.369	9.95	0.032
Rock	$z_w$	3.566	12.1	0.016

Table S-VII: Torsional parameters for  $\text{MnCl}_2 \cdot 2\text{D}_2\text{O}$ . The torsion axes are given with respect to the ligand-fixed frame. Moments of inertia are calculated from the geometry of a free heavy water ligand. The torsional frequencies  $\omega_\alpha$  were reported in a Raman spectroscopy study and have been scaled to account for the deuterium labeling.[3]  $\langle \theta_\alpha^2 \rangle$  is given in the harmonic oscillator approximation according to Eq. (7).

## VII. TENSOR AVERAGING BY TORSIONAL MOTION

The paramagnetic shift tensor is affected by the librational motion of the ligand, fast on the NMR time scale. We consider here the averaging effects of the torsional modes for the case of trigonal ligand coordination. We parameterize the dependence of instantaneous tensor on the torsional angles and evaluate

$$\langle \mathbf{P} \rangle_{\mathcal{I}} = \frac{\text{Tr}\{\mathbf{P}(\theta_{x_w}, \theta_{y_w}, \theta_{z_w}) e^{-\mathcal{H}_{\text{lib}}(\theta_{x_w}, \theta_{y_w}, \theta_{z_w})/(k_B T)}\}}{\text{Tr}\{e^{-\mathcal{H}_{\text{lib}}(\theta_{x_w}, \theta_{y_w}, \theta_{z_w})/(k_B T)}\}}, \quad (1)$$

where  $\langle \mathbf{P} \rangle_{\mathcal{I}}$  denotes the instantaneous tensor  $\mathbf{P}$  for the deuteron site under consideration, corrected for torsional motion, and the  $\theta_\alpha$  represent rotations about the torsion axes away from the equilibrium position of the ligand. To render this tractable, we make the approximation that the torsional modes are uncoupled,

$$\mathcal{H}_{\text{lib}}(\theta_{x_w}, \theta_{y_w}, \theta_{z_w}) = \mathcal{H}_{\text{wag}}(\theta_{x_w}) + \mathcal{H}_{\text{twist}}(\theta_{y_w}) + \mathcal{H}_{\text{rock}}(\theta_{z_w}), \quad (2)$$

and assume that the temperature is low enough that the amplitude of the torsions is small, allowing us to approximate  $\mathcal{H}_{\text{mode}}$  using the harmonic oscillator potential in an angular coordinate basis,

$$\mathcal{H}_{\text{mode}}(\theta_\alpha) = -\frac{\hbar^2}{2\mathcal{I}_\alpha} \frac{d^2}{d\theta_\alpha^2} + \frac{1}{2}\mathcal{I}_\alpha \omega_\alpha^2 \theta_\alpha^2. \quad (3)$$

where  $\mathcal{I}_\alpha$  is the moment about the principal axis  $\alpha$  of the inertia tensor and  $\omega_\alpha$  is the torsional frequency, which is experimentally accessible by spectroscopy. The conventional ordering of the inertia tensor principal axis system is such that the principal moments are ordered according to  $\mathcal{I}_x \leq \mathcal{I}_y \leq \mathcal{I}_z$ . The inertia tensor is easily calculated for heavy water in the ligand fixed frame, in which it is found to be diagonal, with the principal moments ordered according to  $\mathcal{I}_{x_w} < \mathcal{I}_{y_w} < \mathcal{I}_{z_w}$  as shown in Table S-VII. Aside from a shift in origin from the oxygen atom to the center of mass of the ligand, the ligand fixed frame is the PAS of the inertia tensor by the standard labeling convention.

We adopt the parameterization

$$\mathbf{P}(\theta_{x_w}, \theta_{y_w}, \theta_{z_w}) = \mathbf{D}_0 + \mathbf{a}_1 \theta_{x_w} + \mathbf{a}_2 \theta_{x_w}^2 + \mathbf{b}_1 \theta_{y_w} + \mathbf{b}_2 \theta_{y_w}^2 + \mathbf{c}_1 \theta_{z_w} + \mathbf{c}_2 \theta_{z_w}^2, \quad (4)$$

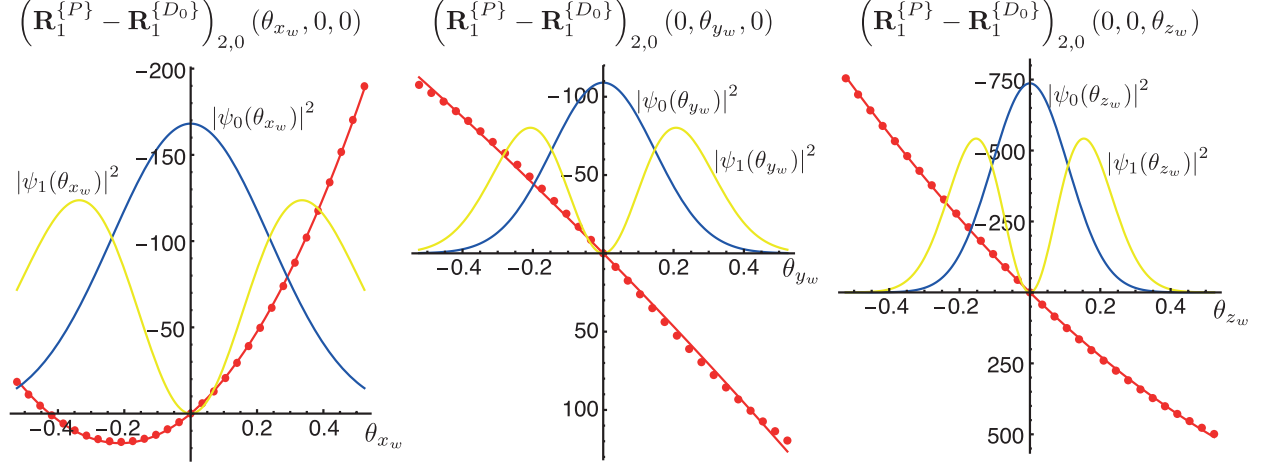


Figure S10: Departure of the lattice-fixed frame  $S_{2,0}$  component of the instantaneous paramagnetic shift tensor  $\mathbf{R}_1^{\{P\}}(\theta_{xw}, \theta_{yw}, \theta_{zw})$  in  $\text{MnCl}_2 \cdot 2\text{D}_2\text{O}$  from its value at the equilibrium deuteron position. The horizontal axis, in radians, corresponds to  $\theta_\alpha$  ranging from  $-30^\circ$  to  $30^\circ$ . Red dots are the numerically calculated values using the “Mn+Cl” source model and  $f_{\text{Cl}} = 6.7\%$ . The red line is the best fit parabola according to Eq. (4). Blue and yellow lines are respectively the (arbitrarily scaled) position space harmonic oscillator wave functions  $|\psi_0(\theta_\alpha)|^2$  and  $|\psi_1(\theta_\alpha)|^2$  calculated using the moments of inertia and torsional frequencies in Table S-VII. They are given to provide a sense of the angular domain over which the instantaneous paramagnetic shift tensor is “sampled”.

where  $\mathbf{D}_0$  is the instantaneous paramagnetic shift tensor calculated at the equilibrium position of the ligand. The remaining coefficient tensors are to be determined by calculating  $\mathbf{P}(\theta_{xw}, \theta_{yw}, \theta_{zw})$  in the lattice-fixed frame as a function of one of the  $\theta_\alpha$  coordinates while holding the other two coordinates at zero and fitting the simplified function to a parabola.

With Eqs. (2) and (4) we find that Eq. (1) reduces to

$$\langle \mathbf{P} \rangle_{\mathcal{I}} = \mathbf{D}_0 + \mathbf{a}_2 \langle \theta_{xw}^2 \rangle_{\mathcal{I}} + \mathbf{b}_2 \langle \theta_{yw}^2 \rangle_{\mathcal{I}} + \mathbf{c}_2 \langle \theta_{zw}^2 \rangle_{\mathcal{I}}. \quad (5)$$

Odd powered averages of  $\theta_\alpha$  vanish because of the symmetry of the  $\mathcal{H}_{\text{mode}}(\theta_\alpha)$ . Each angular variance  $\langle \theta_\alpha^2 \rangle_{\mathcal{I}}$  represents a statistical average over the canonical ensemble,

$$\langle \theta_\alpha^2 \rangle_{\mathcal{I}} = \frac{\text{Tr}\{\theta_\alpha^2 e^{-\mathcal{H}_{\text{mode}}(\theta_\alpha)/(k_B T)}\}}{\text{Tr}\{e^{-\mathcal{H}_{\text{mode}}(\theta_\alpha)/(k_B T)}\}}, \quad (6)$$

which for the harmonic oscillator problem can be solved to give the following analytic solution:

$$\langle \theta_\alpha^2 \rangle_{\mathcal{I}} = \frac{\hbar}{\mathcal{I}_\alpha \omega_\alpha} \left( \frac{1}{2} + \frac{1}{e^{\hbar \omega_\alpha / (k_B T)} - 1} \right). \quad (7)$$

Using  $\mathcal{I}_\alpha$  and  $\omega_\alpha$  we calculate the variances using Eq. (7) and give the results in Table S-VII. It is worth noting that experimental data from NMR and NQR can be used to determine the  $\langle \theta_\alpha^2 \rangle_{\mathcal{I}}$  in favorable cases.[4, 5]

In our regression analysis of the tensor coefficients in Eq. (5), we used the irreducible spherical basis. Fig. S10 illustrates the quadratic parameterization according to Eq. (4) for

Compound	Tensor	$\langle \zeta_P \rangle$ / ppm	$\langle \eta_P \rangle$	$\langle \alpha_{\text{rel}} \rangle$
$\text{CoCl}_2 \cdot 2\text{D}_2\text{O}$	$\langle \mathbf{A}^{\{D_0\}} \rangle$	1320	0.392	164.4°
	$\langle \mathbf{A}^{\{P_{\mathcal{I}}\}} \rangle$	1369	0.373	165.7°
$\text{FeCl}_2 \cdot 2\text{D}_2\text{O}$	$\langle \mathbf{A}^{\{D_0\}} \rangle$	1150	0.705	136.9°
	$\langle \mathbf{A}^{\{P_{\mathcal{I}}\}} \rangle$	1193	0.655	136.3°
$\text{MnCl}_2 \cdot 2\text{D}_2\text{O}$	$\langle \mathbf{A}^{\{D_0\}} \rangle$	1233	0.601	147.1°
	$\langle \mathbf{A}^{\{P_{\mathcal{I}}\}} \rangle$	1278	0.556	147.1°

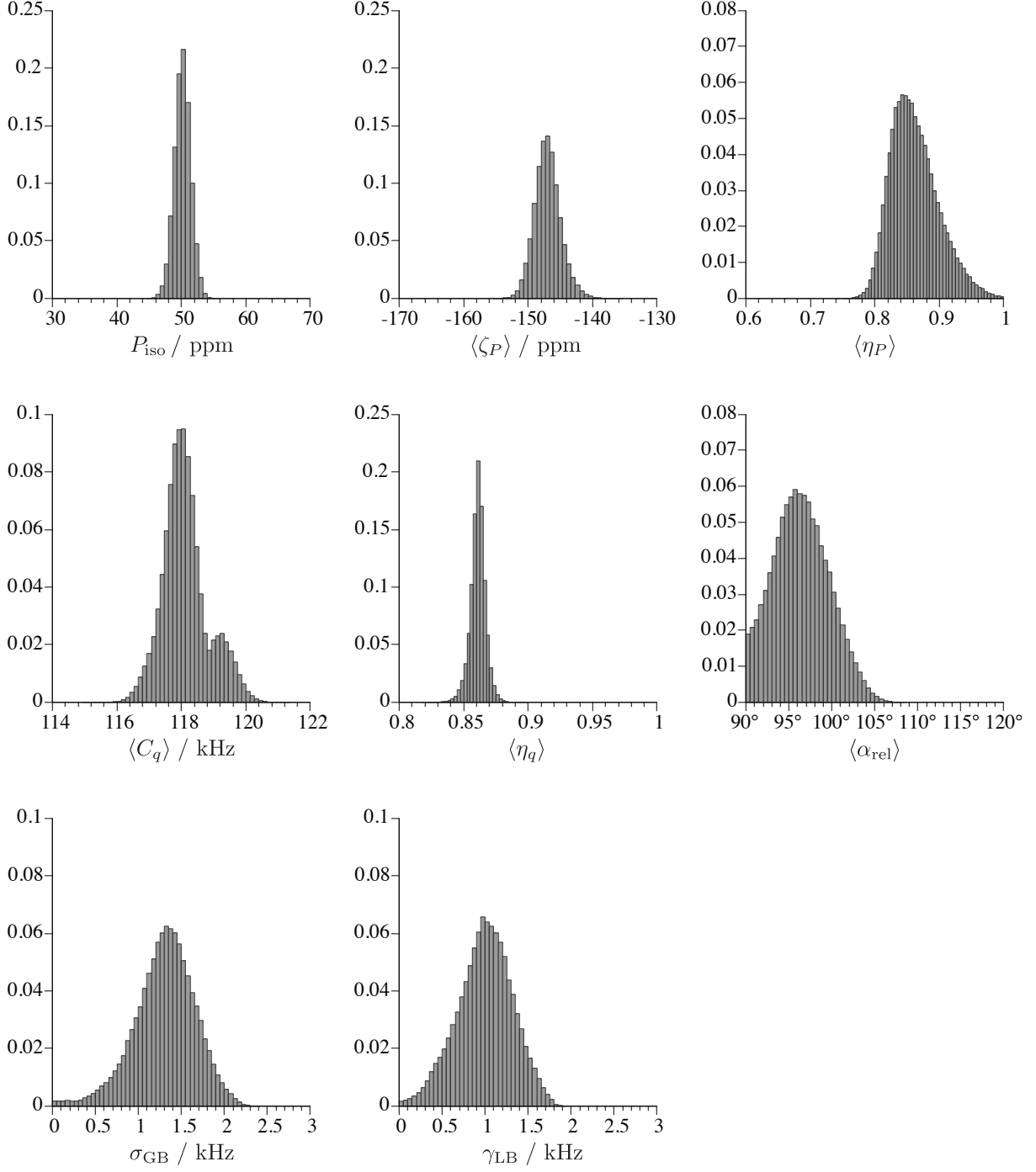
Table S-VIII: Torsion-corrected motionally averaged paramagnetic shift tensors for the isostructural series in the ligand-fixed frame (equivalent to the efg PAS),  $\langle \mathbf{A}^{\{P_{\mathcal{I}}\}} \rangle$ , compared to the uncorrected tensors,  $\langle \mathbf{A}^{\{D_0\}} \rangle$ . The torsion parameters in Table S-VII were used for each system. The paramagnetic shift tensor calculation implemented the “M+Cl” source models with  $f_{\text{Cl}} = 6.7\%$  (Mn),  $f_{\text{Cl}} = 4.1\%$  (Fe), and  $f_{\text{Cl}} = 3.9\%$  (Co).

the  $S_{2,0}$  component of  $\mathbf{R}_1^{\{P\}}(\theta_{x_w}, \theta_{y_w}, \theta_{z_w})$ . The parameterization is rather good within 30° of equilibrium for each torsional mode. With the coefficient tensors and angular variances known, we calculate the torsion-corrected motionally averaged paramagnetic shift tensor in the lattice fixed frame,  $\langle \mathbf{R}^{\{P_{\mathcal{I}}\}} \rangle$ , in the same way as described in the trigonal motional model section of the main text but with the substitution  $\mathbf{R}_1^{\{P\}} \rightarrow \mathbf{R}_1^{\{P_{\mathcal{I}}\}}$ . The paramagnetic shift tensor of the ligand frozen in its equilibrium position expressed in the PAS of the efg tensor (which is unaffected in this model of torsional averaging),  $\langle \mathbf{A}^{\{D_0\}} \rangle$ , is of course identical to results for  $\langle \mathbf{A}^{\{P\}} \rangle$  presented in the main text. With the inclusion of the torsional correction, the  $\langle \mathbf{A}^{\{P_{\mathcal{I}}\}} \rangle$  tensor tends to larger  $\langle \zeta_P \rangle$  and smaller  $\langle \eta_P \rangle$ , while  $\langle \alpha_{\text{rel}} \rangle$  is roughly unchanged. These effects are consistent across the isostructural series, as seen in Table S-VIII. Neglect of torsion influences the results to a level of no more than 5% at 300 K.

## VIII. MARGINAL PARAMETER DISTRIBUTIONS

The following histograms are giving for the purposes of visualizing secondary likelihood maxima and correlations between fit parameters.





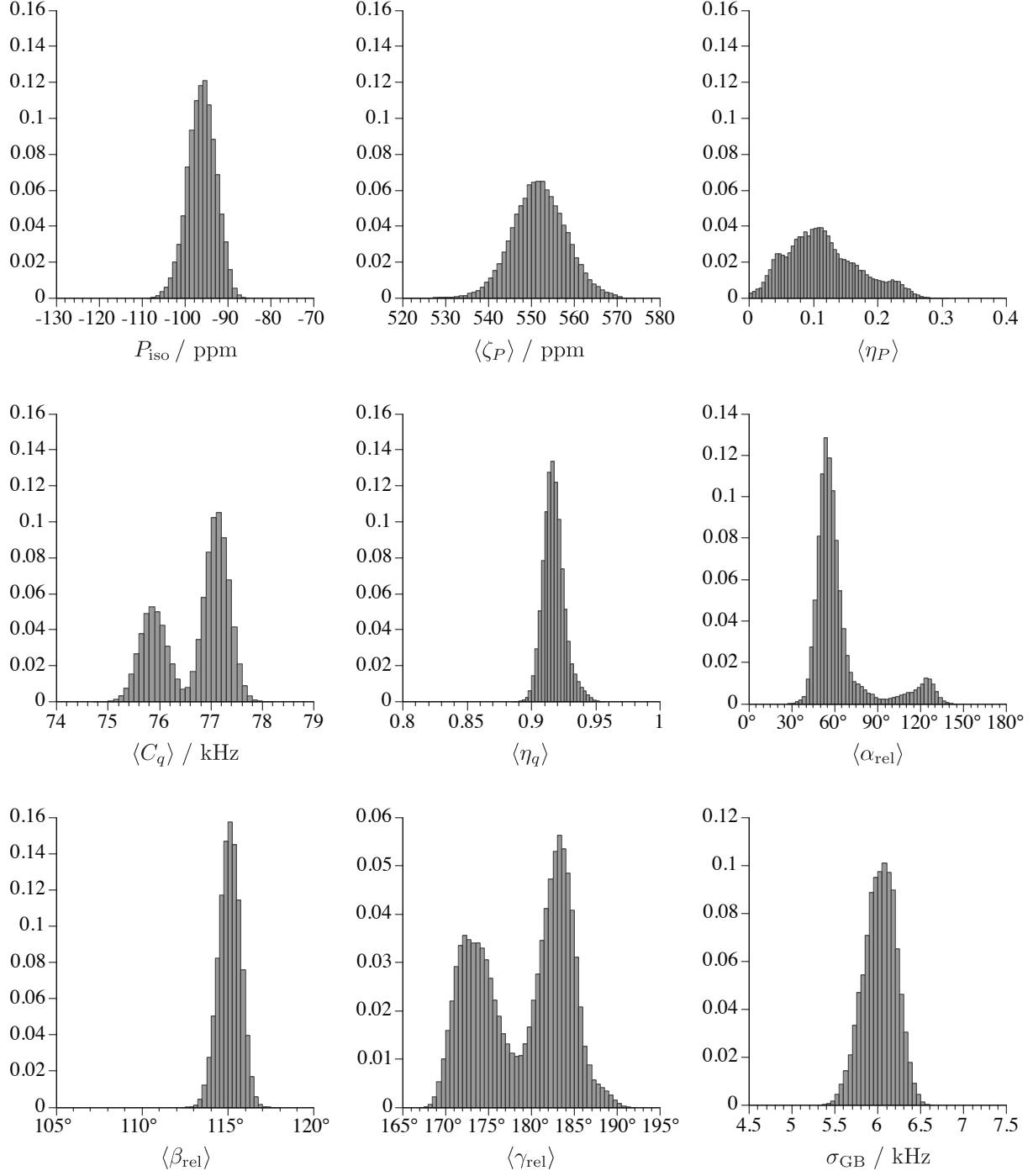
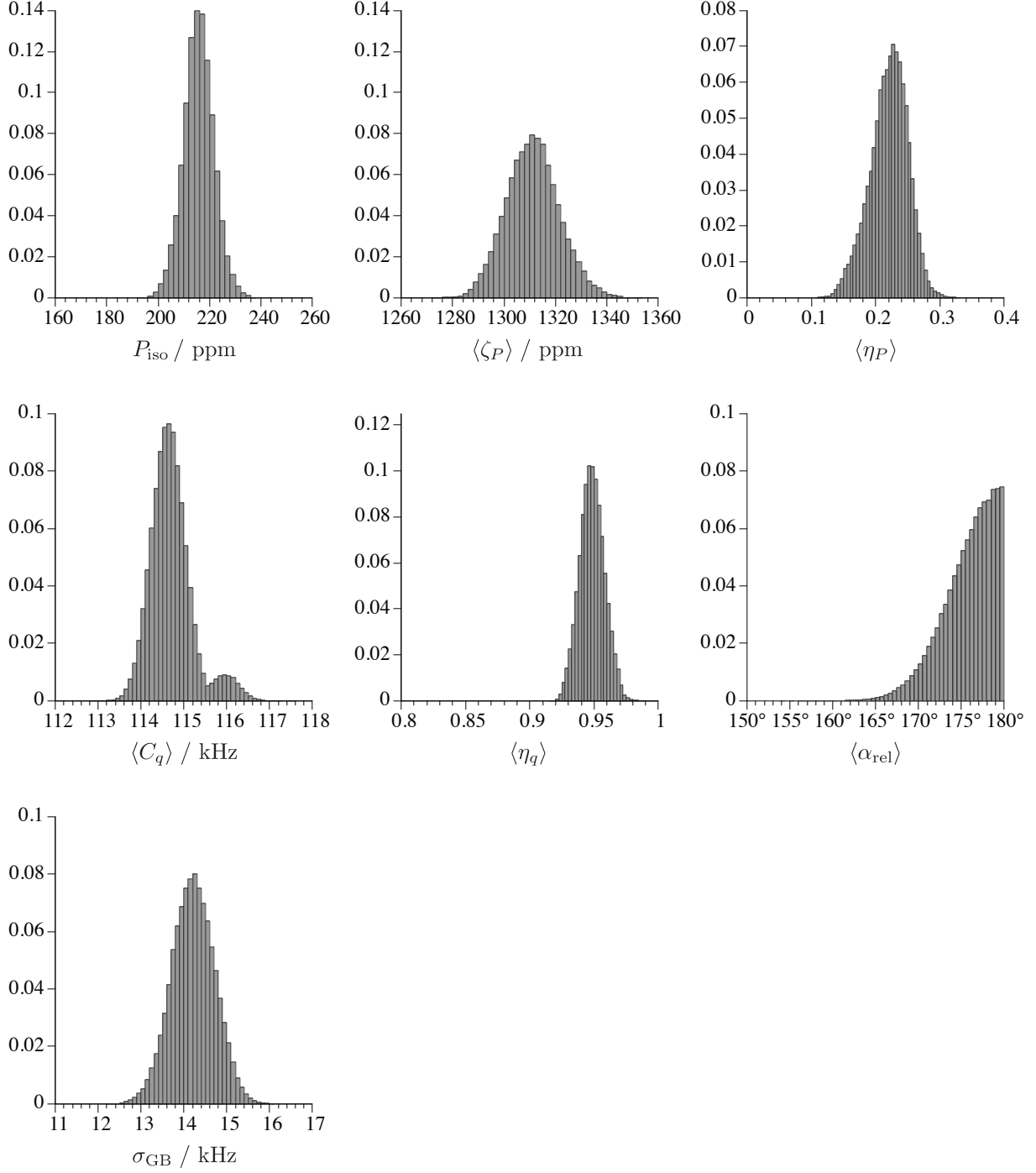


Figure S12: Histograms showing maximum likelihood parameter distributions for  $\text{NiCl}_2 \cdot 2\text{D}_2\text{O}$  marginalized over all variables but  $X$  (horizontal axis). The response axis corresponds to  $P(X)$ , the probability that  $X$  falls within its binned range.



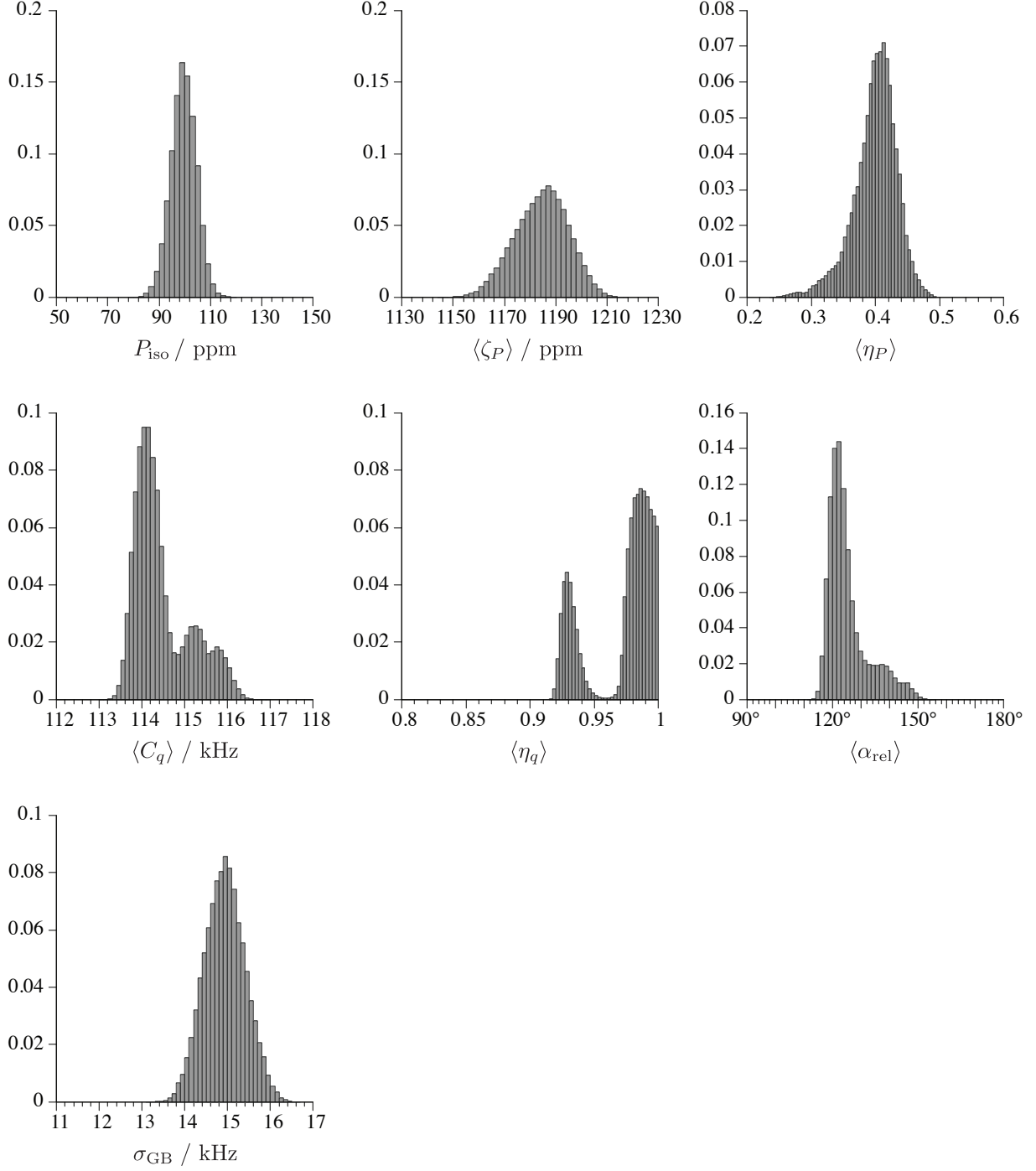


Figure S14: Histograms showing maximum likelihood parameter distributions for  $\text{FeCl}_2 \cdot 2\text{D}_2\text{O}$  marginalized over all variables but  $X$  (horizontal axis). The response axis corresponds to  $P(X)$ , the probability that  $X$  falls within its binned range.

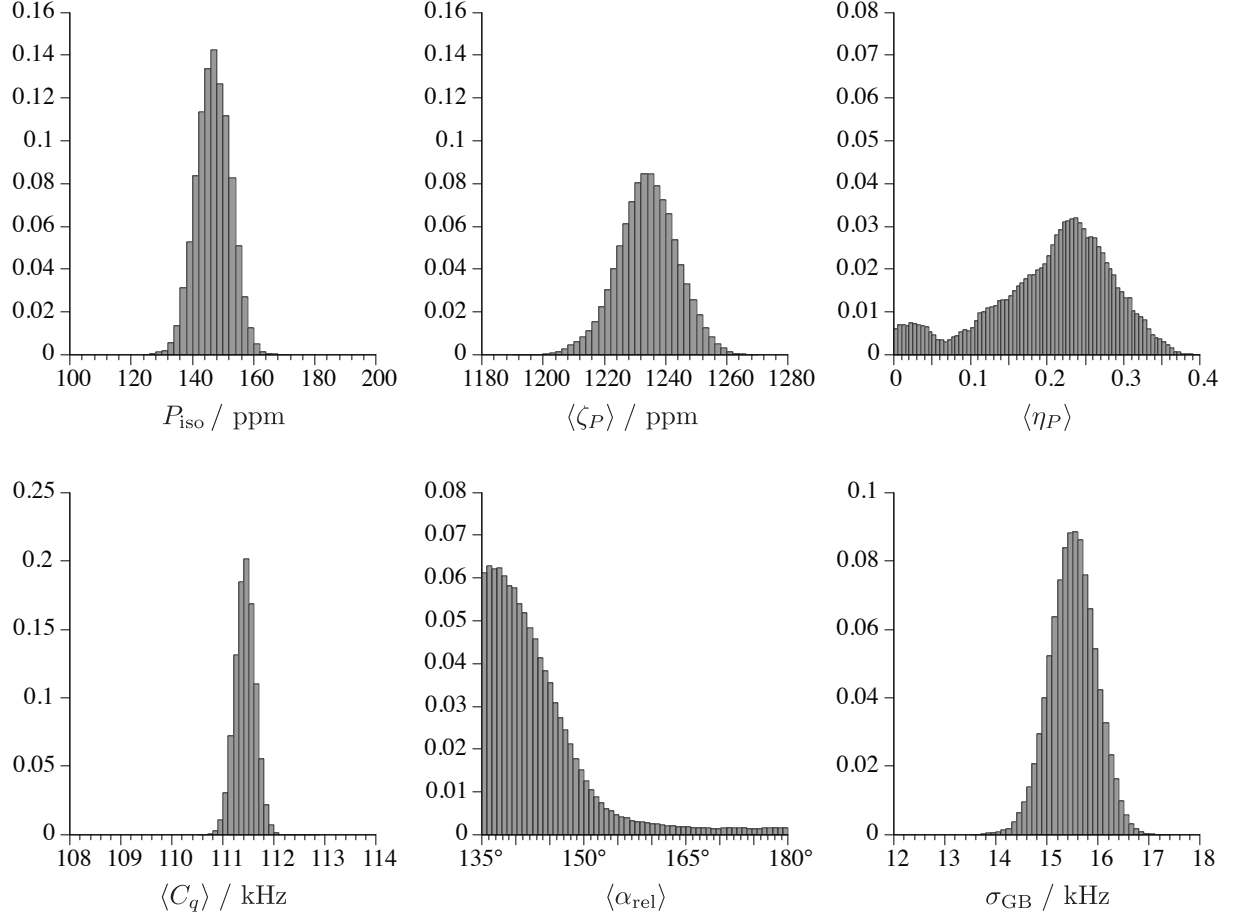
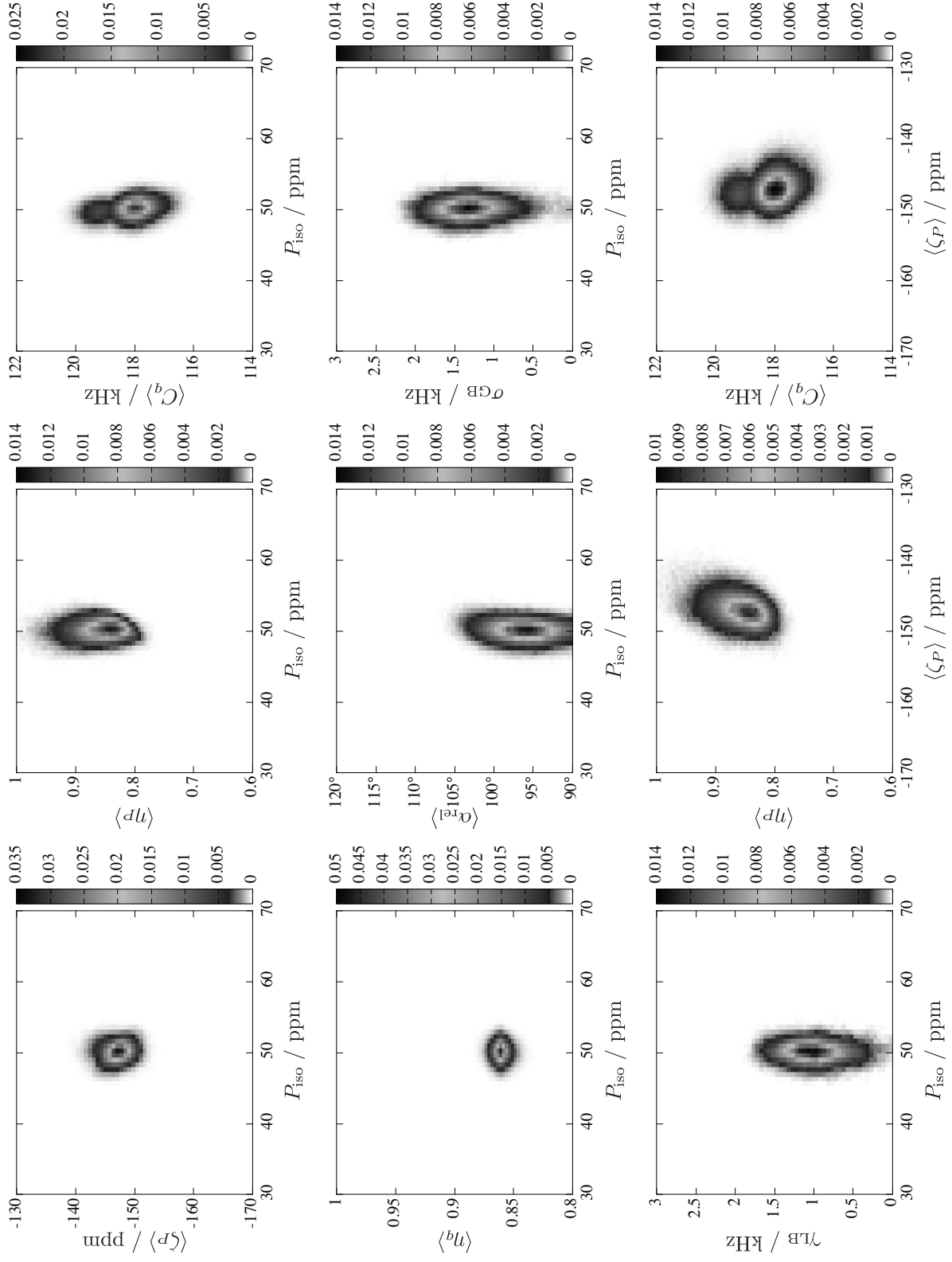
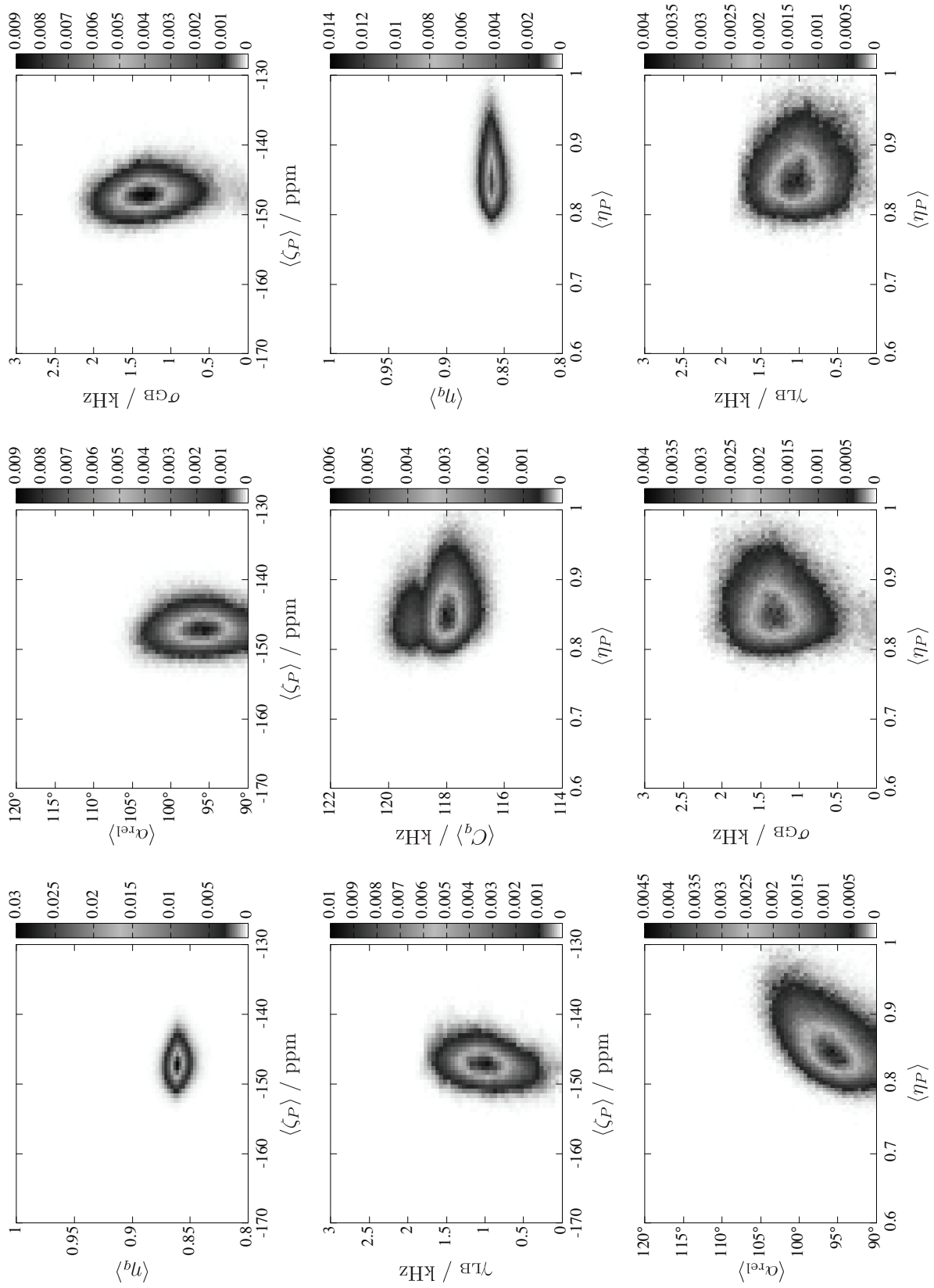
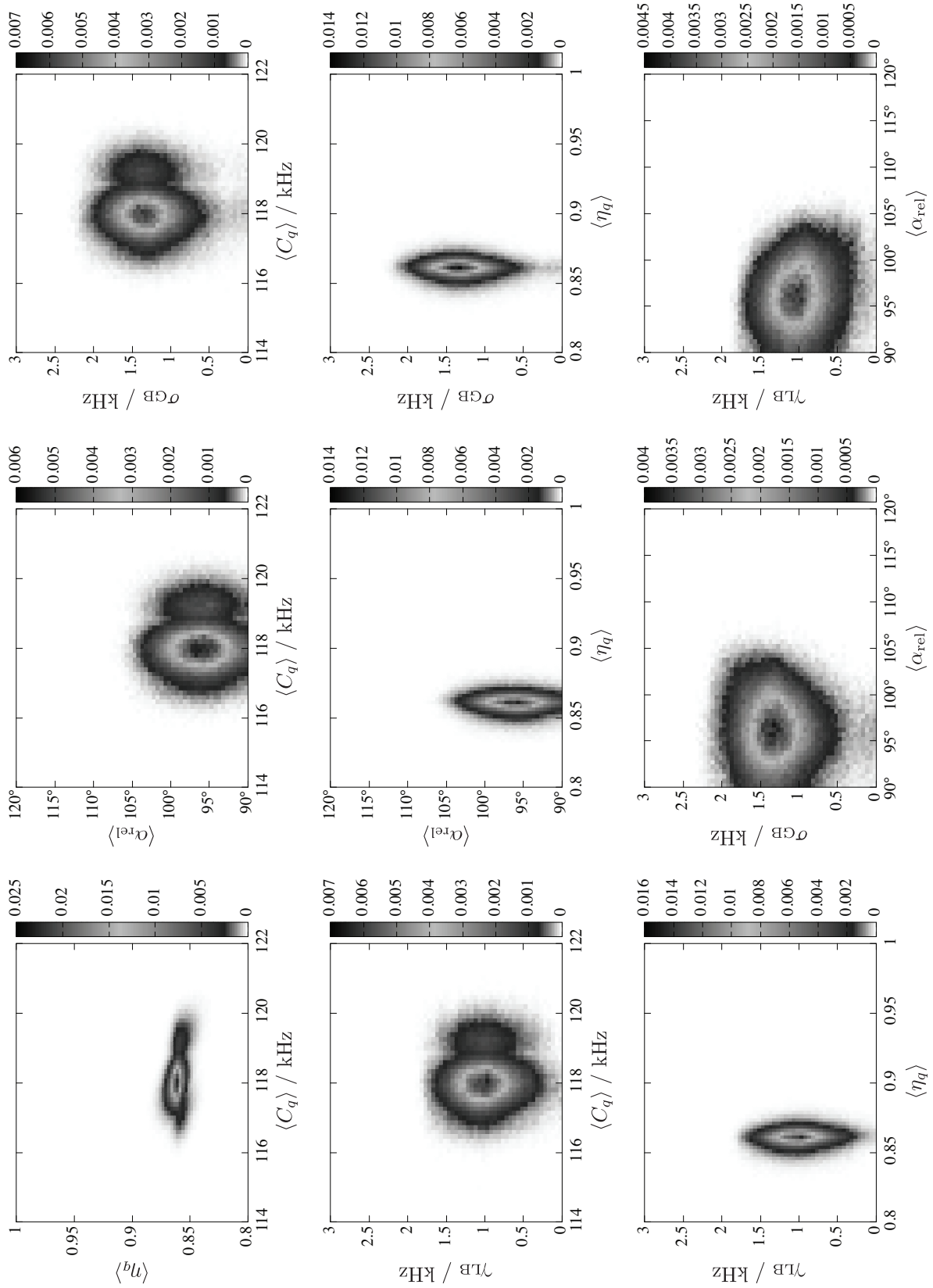


Figure S15: Histograms showing maximum likelihood parameter distributions for  $\text{MnCl}_2 \cdot 2\text{D}_2\text{O}$  marginalized over all variables but  $X$  (horizontal axis). The response axis corresponds to  $P(X)$ , the probability that  $X$  falls within its binned range.









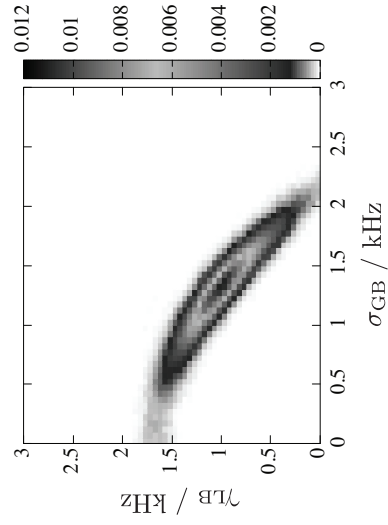
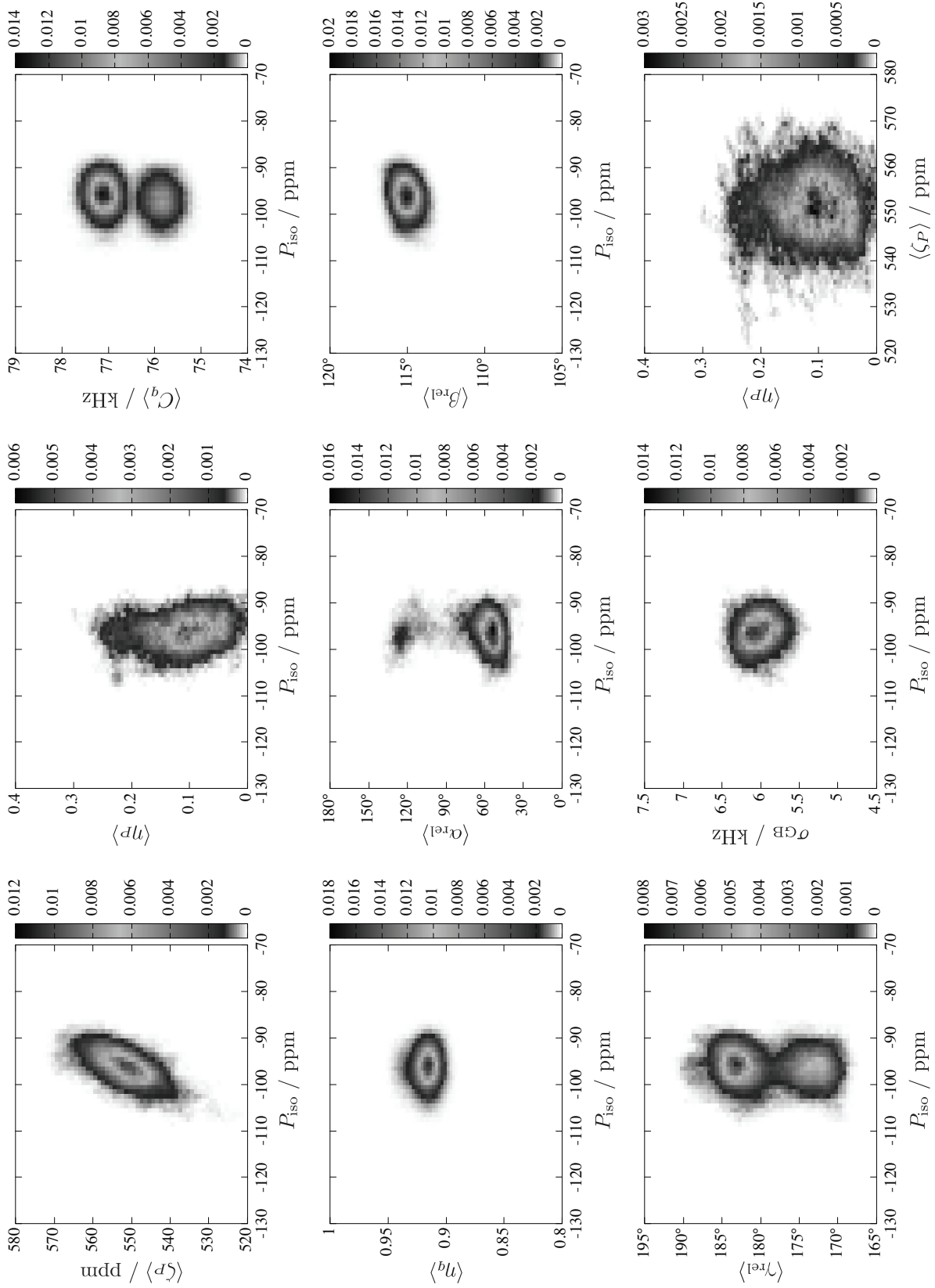
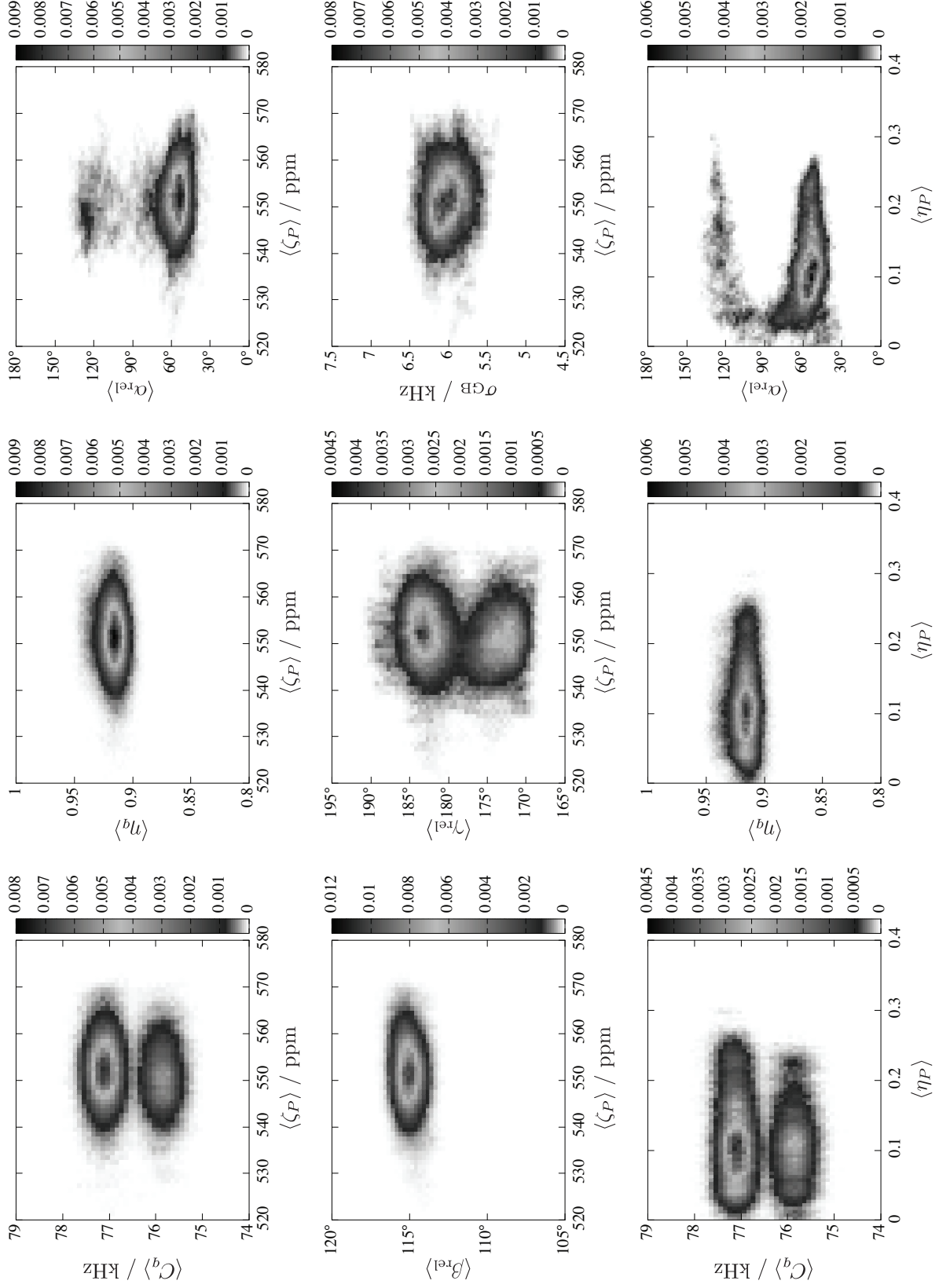
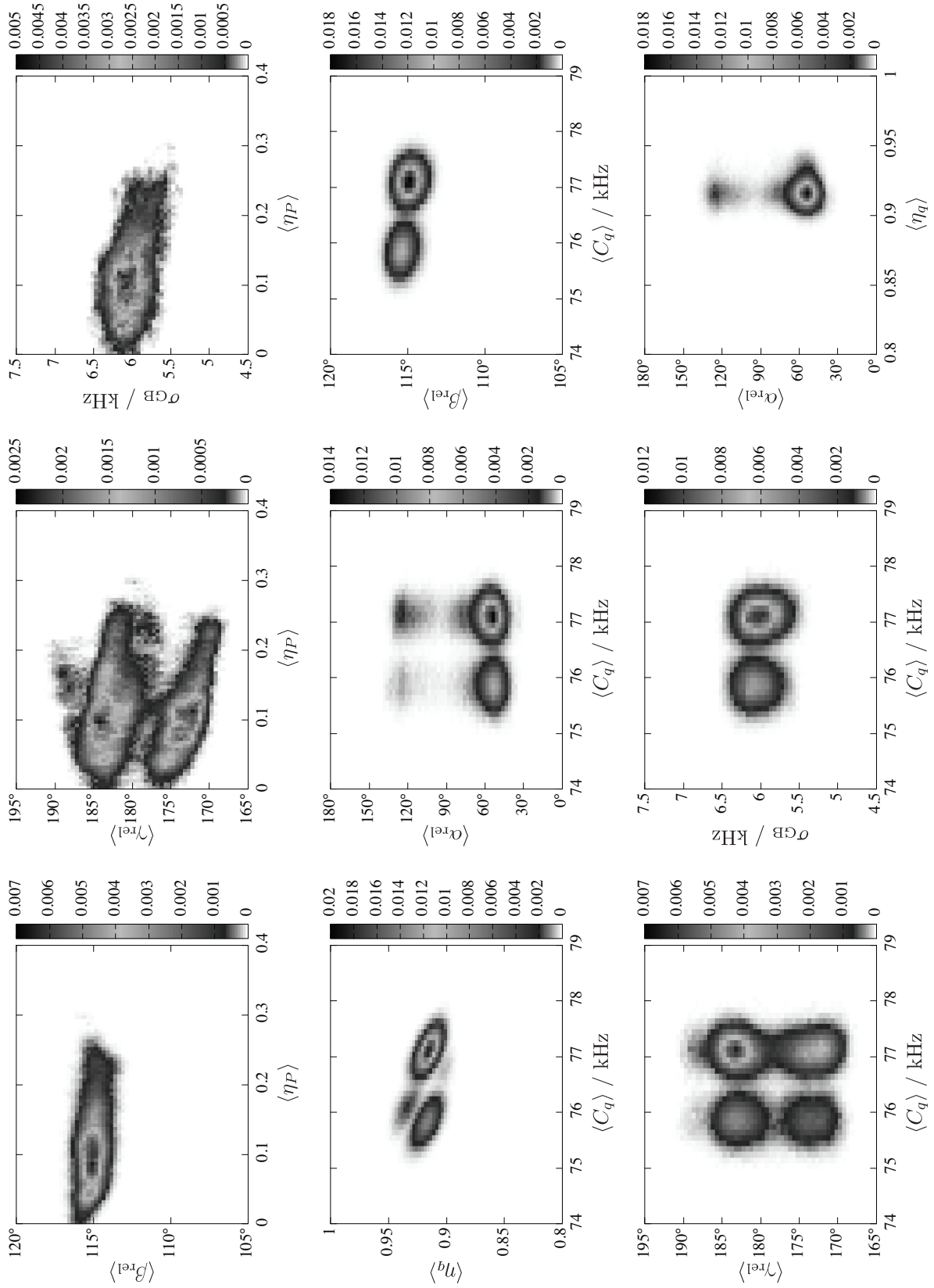


Figure S16: Histograms showing maximum likelihood parameter distributions for  $\text{CuCl}_2 \cdot 2\text{D}_2\text{O}$  marginalized over all variables but  $X$  (horizontal axis) and  $Y$  (vertical axis), providing a visualization of their correlation. The response axis corresponds to  $P(X, Y)$ , the probability that  $X$  and  $Y$  fall within their respective binned ranges.









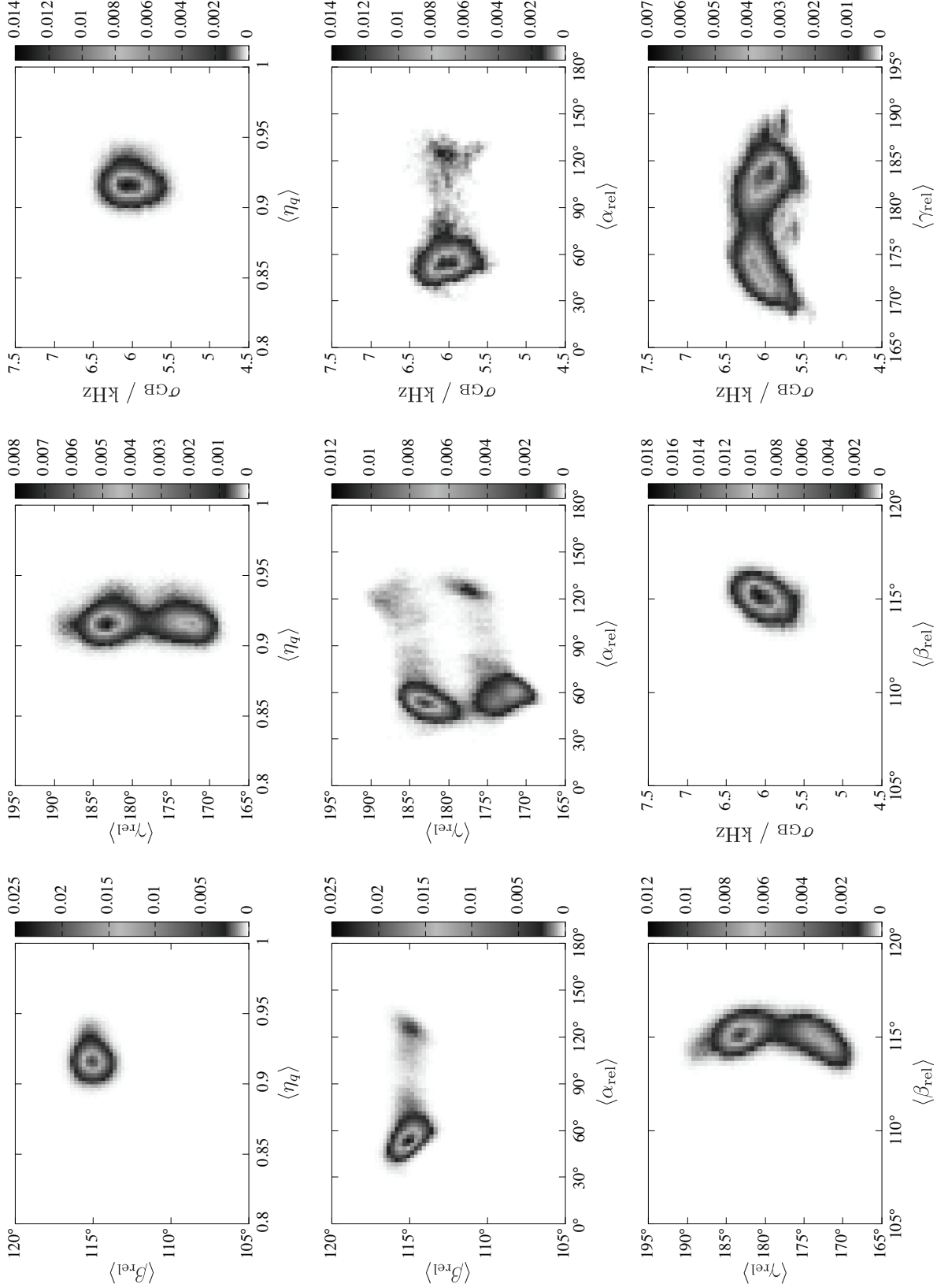
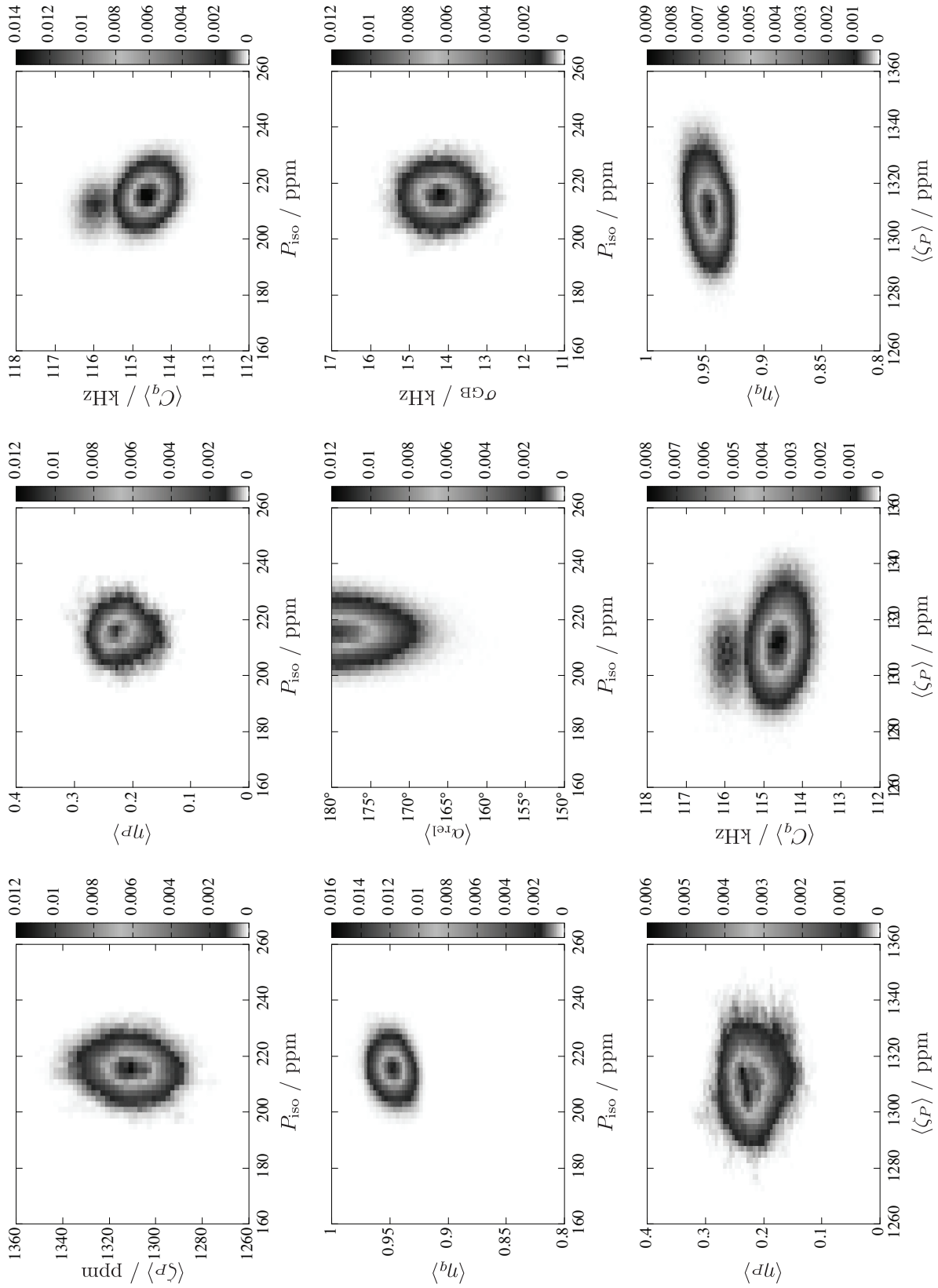
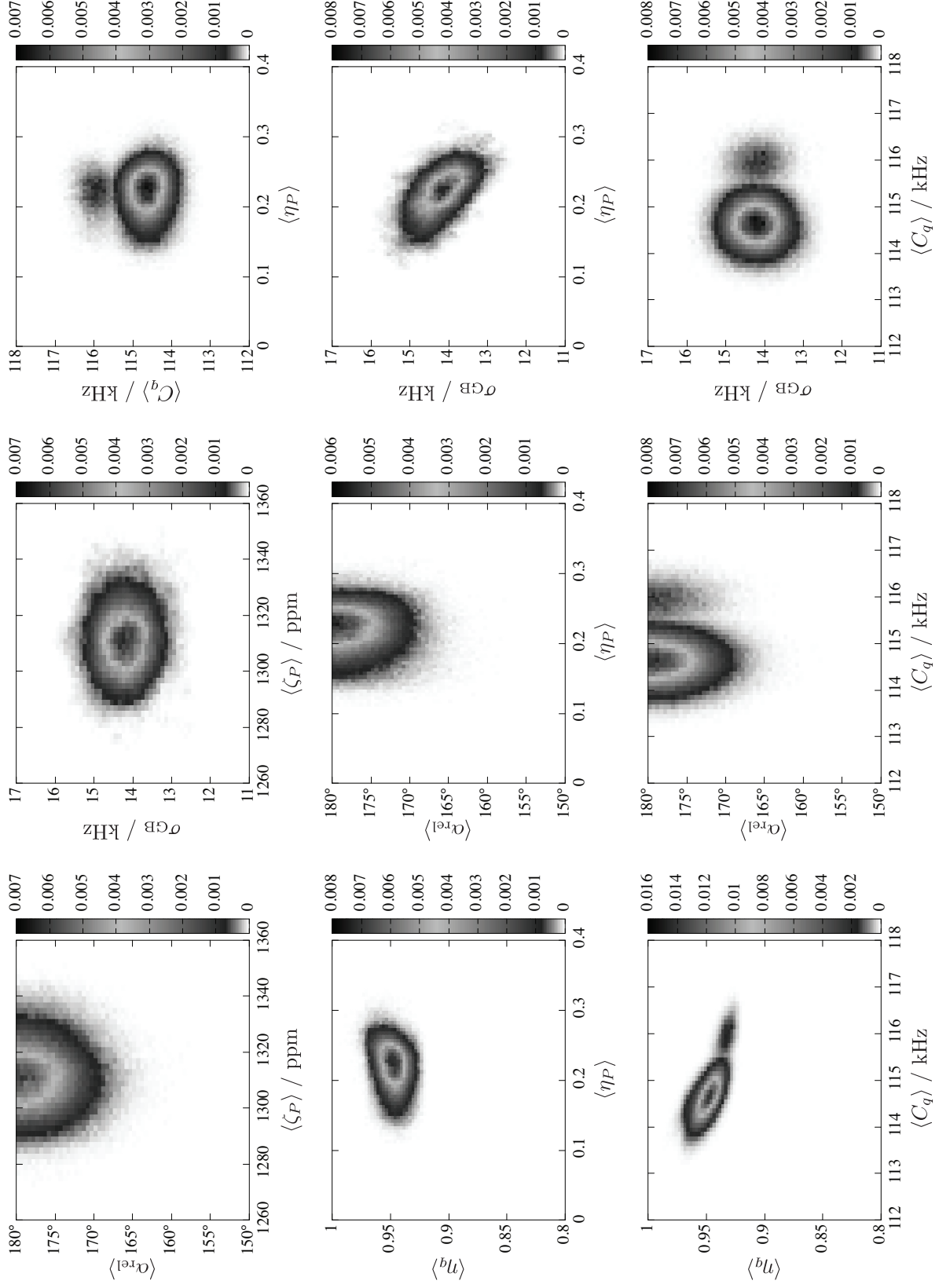


Figure S17: Histograms showing maximum likelihood parameter distributions for  $\text{NiCl}_2 \cdot 2\text{D}_2\text{O}$  marginalized over all variables but  $X$  (horizontal axis) and  $Y$  (vertical axis), providing a visualization of their correlation. The response axis corresponds to  $P(X, Y)$ , the probability that  $X$  and  $Y$  fall within their respective binned ranges.







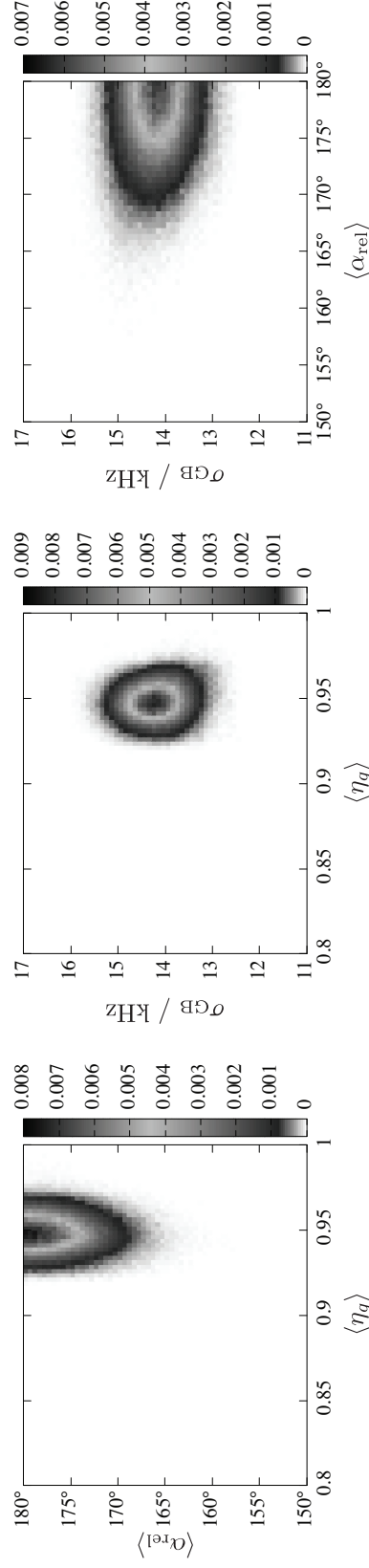
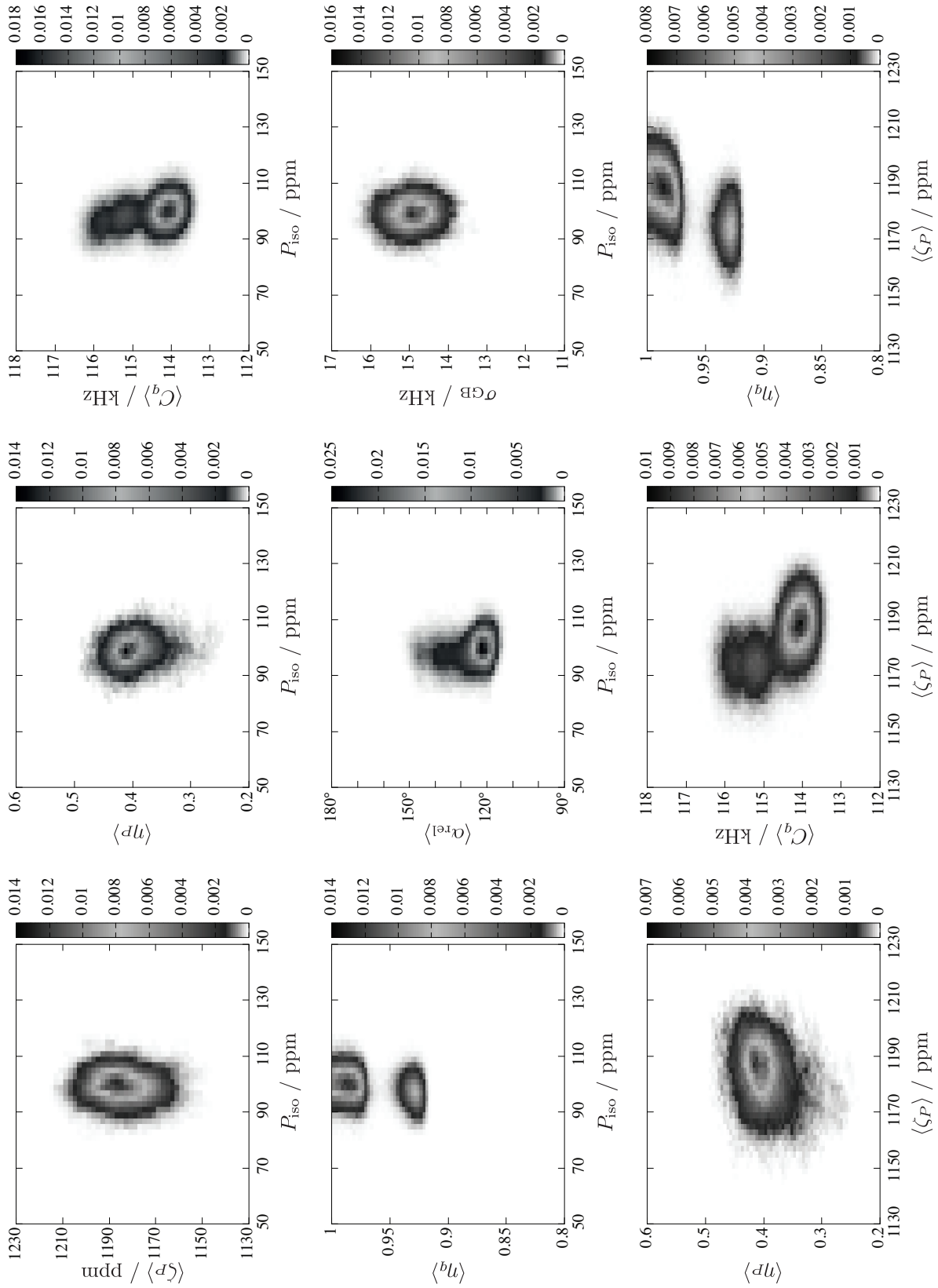
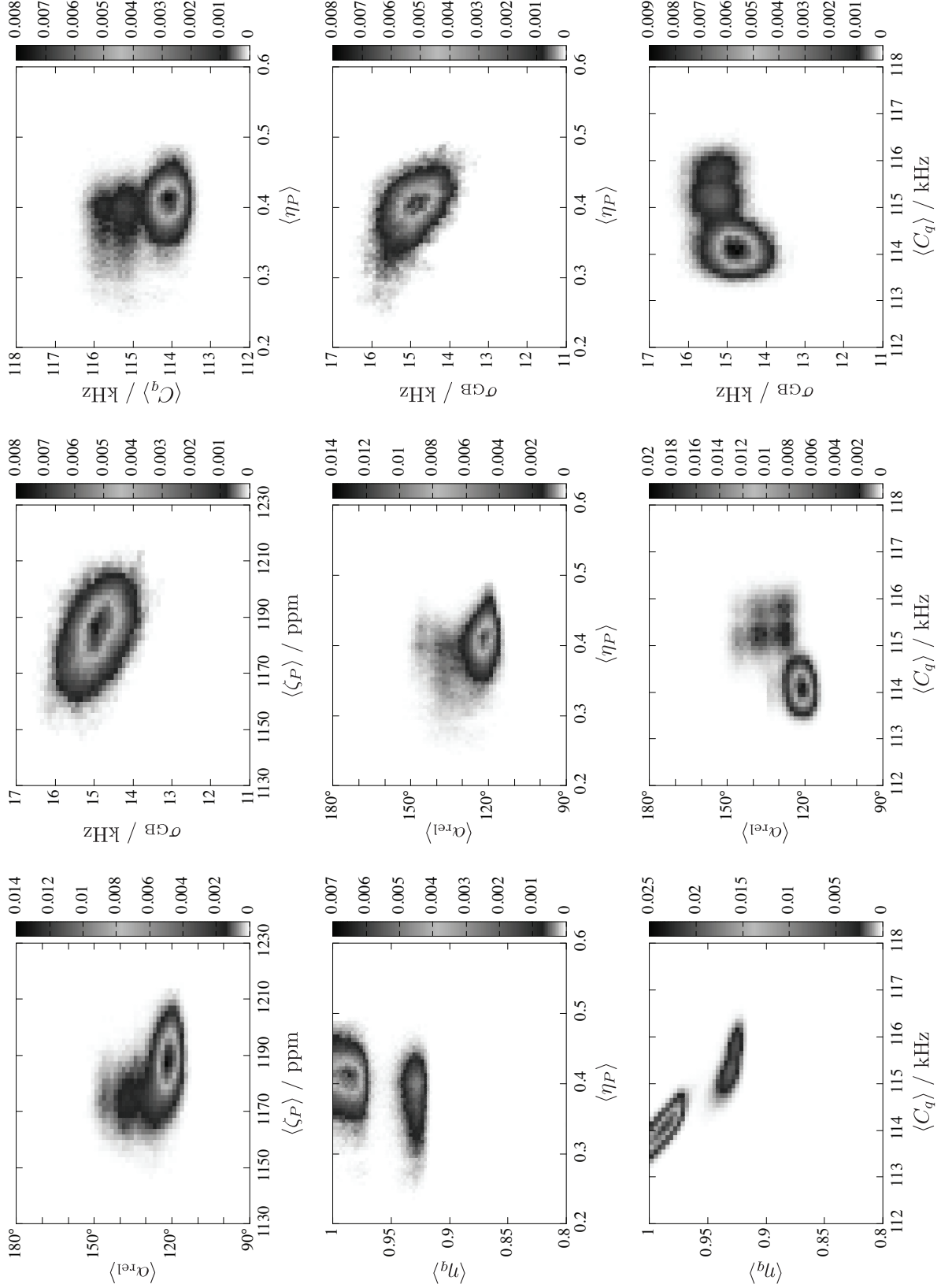


Figure S18: Histograms showing maximum likelihood parameter distributions for  $\text{CoCl}_2 \cdot 2\text{D}_2\text{O}$  marginalized over all variables but  $X$  (horizontal axis) and  $Y$  (vertical axis), providing a visualization of their correlation. The response axis corresponds to  $P(X, Y)$ , the probability that  $X$  and  $Y$  fall within their respective binned ranges.





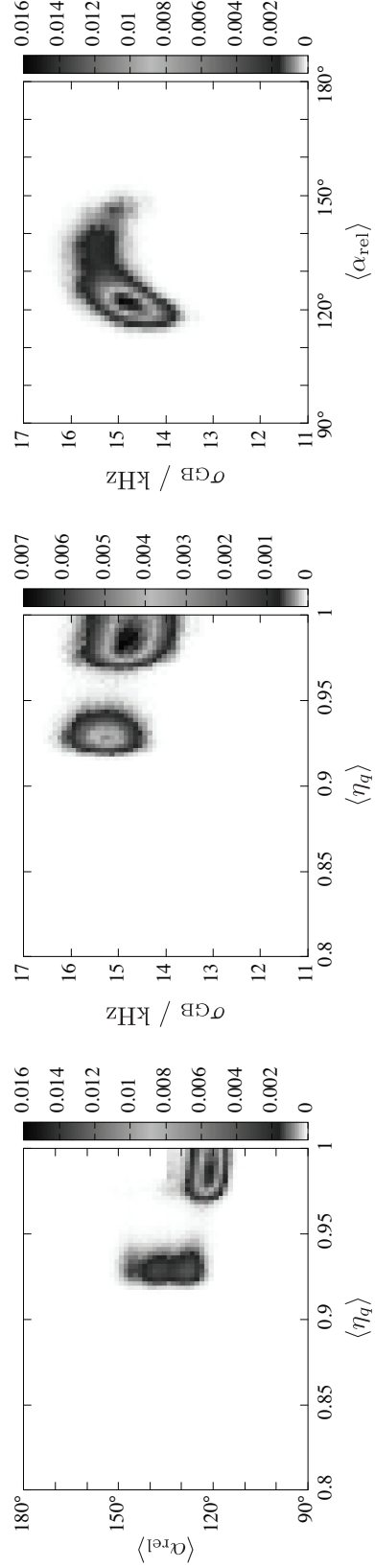
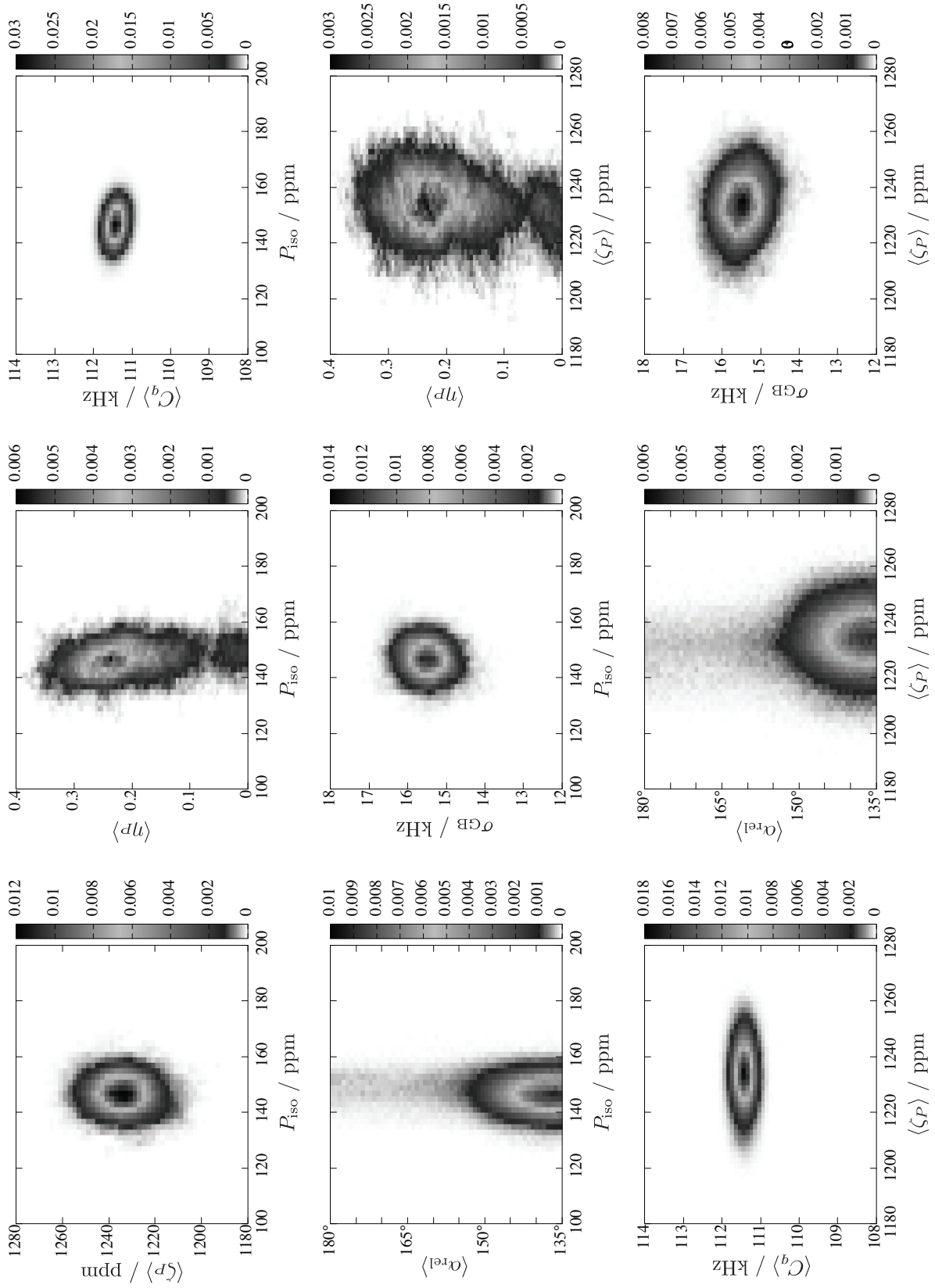


Figure S19: Histograms showing maximum likelihood parameter distributions for  $\text{FeCl}_2 \cdot 2\text{D}_2\text{O}$  marginalized over all variables but  $X$  (horizontal axis) and  $Y$  (vertical axis), providing a visualization of their correlation. The response axis corresponds to  $P(X, Y)$ , the probability that  $X$  and  $Y$  fall within their respective binned ranges.



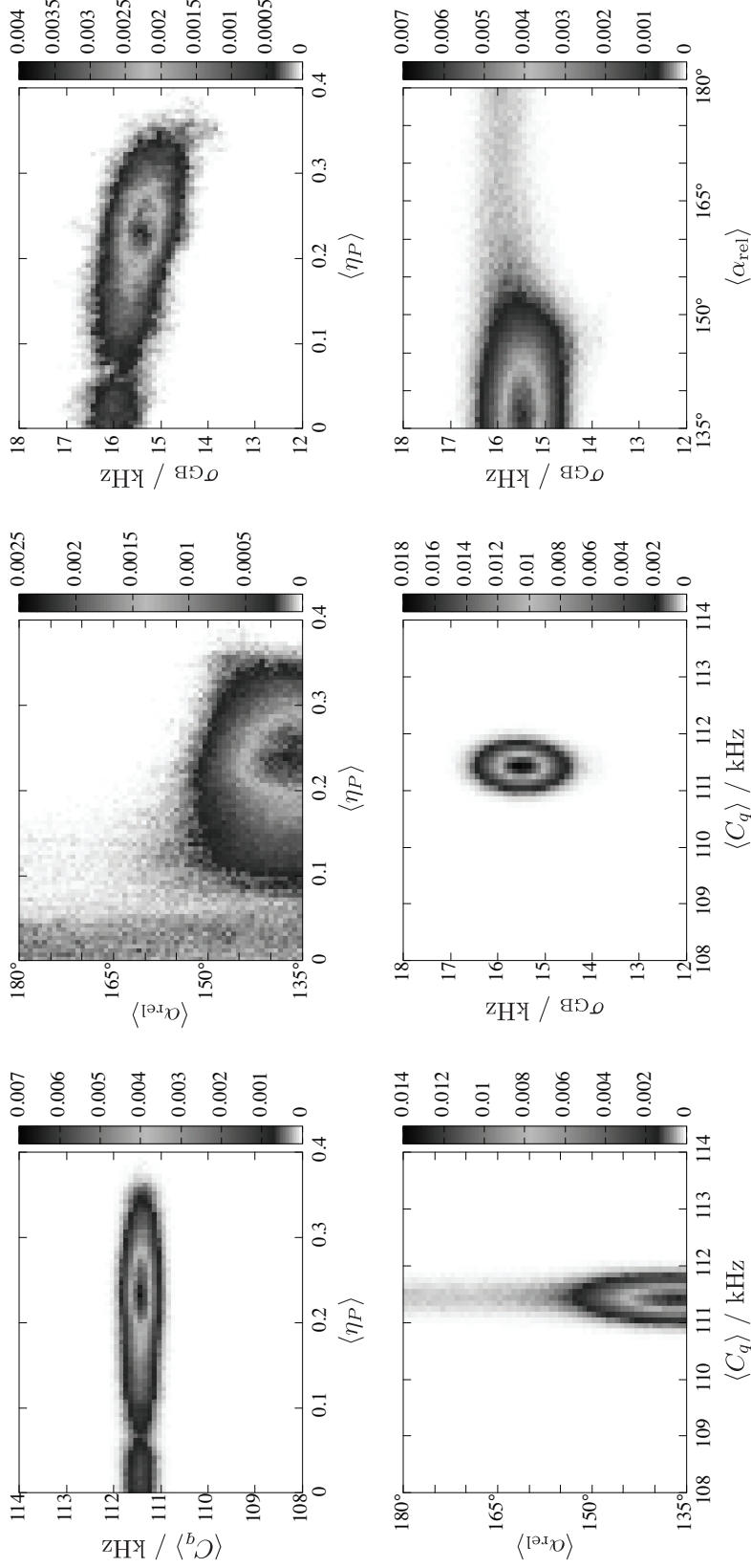


Figure S20: Histograms showing maximum likelihood parameter distributions for  $\text{MnCl}_2 \cdot 2\text{D}_2\text{O}$  marginalized over all variables but  $X$  (horizontal axis) and  $Y$  (vertical axis), providing a visualization of their correlation. The response axis corresponds to  $P(X, Y)$ , the probability that  $X$  and  $Y$  fall within their respective binned ranges.



## IX. STRUCTURAL PARAMETERS AND WATER LIGAND GEOMETRY

Compound	Space group	$(a, b, c) / \text{\AA}$	$\beta$	Ref.	$r_{\text{OD}} / \text{\AA}$	$2\theta_w$	$\phi_d$	$T / \text{K}$	Ref.
MnCl <sub>2</sub> ·2H <sub>2</sub> O	<i>C2/m</i>	(7.409, 8.800, 3.691)	98.67°	[6]					
FeCl <sub>2</sub> ·2H <sub>2</sub> O	<i>C2/m</i>	(7.355, 8.548, 3.637)	98.18°	[6]	0.918	103.9°	52.26°	4.2	[7]
CoCl <sub>2</sub> ·2D <sub>2</sub> O	<i>C2/m</i>	(7.2789, 8.5533, 3.5686)	97.58°	[8]	0.980	103.2°	57.76°	77	[9]
NiCl <sub>2</sub> ·2H <sub>2</sub> O	<i>C2/m</i>	(10.9965, 6.8858, 6.9093)	53.3552°	[10]					
CuCl <sub>2</sub> ·2H <sub>2</sub> O	<i>Pmna</i>	(8.104, 3.757, 7.433)	90°	[11]	0.948	111.4°	51.47°	300	[11, 12]

Table S-IX: Structural and ligand geometry parameters. The unit cell parameters  $a$ ,  $b$ ,  $c$ ,  $\beta$  were taken from the cited room temperature X-ray diffraction studies. The parameters  $r_{\text{OD}}$  and  $2\theta_w$  were determined with coordinates from neutron diffraction or, for CuCl<sub>2</sub>·2H<sub>2</sub>O, X-ray refinement of the neutron diffraction data, at the specified temperature.

Compound	Motional Model	$2\theta_w$
MnCl <sub>2</sub> · 2D <sub>2</sub> O	trigonal	109.47°
FeCl <sub>2</sub> · 2D <sub>2</sub> O	trigonal	109.07°
CoCl <sub>2</sub> · 2D <sub>2</sub> O	trigonal	108.46°
NiCl <sub>2</sub> · 2D <sub>2</sub> O	pyramidal	107.17°
CuCl <sub>2</sub> · 2D <sub>2</sub> O	trigonal	112.55°

Table S-X: Predictions of  $2\theta_w$  from experimental  $|\langle\zeta_q\rangle/\zeta_q|$  and  $\langle\eta_q\rangle$  values.

- 
- [1] K. Juraitis, J. Domiciano, and W. Sano, Journal of Physics and Chemistry of Solids **44**, 531 (1983).
  - [2] A. Narath, Phys. Rev. **140**, A552 (1965).
  - [3] B. K. Srivastava, D. P. Khandelwal, and H. D. Bist, Journal of Raman Spectroscopy **7**, 202 (1978).
  - [4] T. Chiba, J. Chem. Phys. **39**, 947–953 (1963).
  - [5] J. M. Millar, A. M. Thayer, D. B. Zax, and A. Pines, J. Am. Chem. Soc. **108**, 5113–5116 (1986).
  - [6] B. Morosin and E. J. Graeber, The Journal of Chemical Physics **42**, 898 (1965).
  - [7] W. Schneider and H. Weitzel, Acta Crystallographica Section A **32**, 32 (1976).
  - [8] B. Morosin, The Journal of Chemical Physics **44**, 252–257 (1966).
  - [9] D. Cox, B. Frazer, and G. Shirane, Physics Letters **17**, 103 (1965).

- [10] B. Morosin, *Acta Crystallographica* **23**, 630 (1967).
- [11] Å. Engberg, *Acta Chem. Scand.* **24**, 3510 (1970).
- [12] S. W. Peterson and H. A. Levy, *J. Chem. Phys.* **26**, 220 (1957).